UC Berkeley
UC Berkeley Electronic Theses and Dissertations

Title
Characterization of the Structure and Function of the Normal Human Fovea Using Adaptive Optics Scanning Laser Ophthalmoscopy

Permalink
https://escholarship.org/uc/item/2p52s3ck

Author
Putnam, Nicole Marie

Publication Date
2012

Peer reviewed|Thesis/dissertation

eScholarship.org Powered by the California Digital Library
University of California

Characterization of the Structure and Function of the Normal Human Fovea Using Adaptive Optics Scanning Laser Ophthalmoscopy

By

Nicole Marie Putnam

A dissertation submitted in partial satisfaction of the

requirements for the degree of

Doctor of Philosophy

in

Vision Science

in the

Graduate Division

of the

University of California, Berkeley

Committee in charge:

Professor Austin Roorda, Chair
Professor Martin Banks
Professor Daniel Fletcher

Fall 2012

Characterization of the Structure and Function of the Normal Human Fovea
Using Adaptive Optics Scanning Laser Ophthalmoscopy

© 2012

by Nicole Marie Putnam

Abstract

Characterization of the Structure and Function of the Normal Human Fovea
Using Adaptive Optics Scanning Laser Ophthalmoscopy

by

Nicole Marie Putnam

Doctor of Philosophy in Vision Science

University of California, Berkeley

Professor Austin Roorda, Chair

In order to study the limits of spatial vision in normal human subjects, it is important to look at and near the fovea. The fovea is the specialized part of the retina, the light-sensitive multi-layered neural tissue that lines the inner surface of the human eye, where the cone photoreceptors are smallest (approximately 2.5 microns or 0.5 arcmin) and cone density reaches a peak. In addition, there is a 1:1 mapping from the photoreceptors to the brain in this central region of the retina. As a result, the best spatial sampling is achieved in the fovea and it is the retinal location used for acuity and spatial vision tasks. However, vision is typically limited by the blur induced by the normal optics of the eye and clinical tests of foveal vision and foveal imaging are both limited due to the blur. As a result, it is unclear what the perceptual benefit of extremely high cone density is. Cutting-edge imaging technology, specifically Adaptive Optics Scanning Laser Ophthalmoscopy (AOSLO), can be utilized to remove this blur, zoom in, and as a result visualize individual cone photoreceptors throughout the central fovea. This imaging combined with simultaneous image stabilization and targeted stimulus delivery expands our understanding of both the anatomical structure of the fovea on a microscopic scale and the placement of stimuli within this retinal area during visual tasks. The final step is to investigate the role of temporal variables in spatial vision tasks since the eye is in constant motion even during steady fixation. In order to learn more about the fovea, it becomes important to study the effect of this motion on spatial vision tasks. This dissertation steps through many of these considerations, starting with a model of the foveal cone mosaic imaged with AOSLO. We then use this high resolution imaging to compare anatomical and functional markers of the center of the normal human fovea. Finally, we investigate the role of natural and manipulated fixational eye movements in foveal vision, specifically looking at a motion detection task, contrast sensitivity, and image fading.

TABLE OF CONTENTS

LIST OF FIGURES

LIST OF ABBREVIATIONS

AFC:	alternative forced choice
AO:	adaptive optics
AOM:	acousto-optic modulator
AOSLO:	adaptive optics scanning laser ophthalmoscopy (or ophthalmoscope)
CCD:	charge-coupled device
cpd:	cycles per degree
CSF:	contrast sensitivity function
D:	diopters (m^{-1})
DM:	deformable mirror
ELM:	external limiting membrane
FFT:	fast Fourier transform
FWHM:	full width at half maximum
GUI:	graphical user interface
ICD:	center-to-center inter-cone distance
IR:	infrared
IS:	inner segment
LSO:	line scanning ophthalmoscopy (or ophthalmoscope)
MEMS:	microelectromechanical systems
MTF:	modulation transfer function
OCT:	optical coherence tomography
OS:	outer segment
OTF:	optical transfer function
PFD:	preferred fixation direction
PRL:	preferred retinal locus of fixation
PSF:	point spread function
RMS:	root mean square
SHWS:	Shack-Hartmann wavefront sensor
SLD:	superluminescent diode
SNR:	signal to noise ratio
WFS:	wavefront sensor

ACKNOWLEDGEMENTS

I would like to take this opportunity to thank my parents. They are two of the most selfless people I know and their unwavering support and belief that I could accomplish anything I set my sights on has been integral to my happiness and success academically and in life. They were always willing to listen patiently as I talked about things they did not understand and I am incredibly lucky to have their love and support. I would also like to thank my brother Daniel. Even though he is still figuring out his interests and aspirations, he is an inspiration to me and reminds me that it is important to always strive to learn, understand, and question the world.

In addition to my wonderful family, I am lucky to have many friends who I would like to thank. These friendships and support exceed all my hopes and expectations. Thank you to Heather Durko, Jennifer Hayes, Alissa Peck, Crystal Thomas, Amanda Alvarez, Paul Ivanov, Rachael Byrne, and Barak Michener who each spent many hours listening to my crazy ideas, my successes, failures, excitement, and frustration over the years. I would also like to thank my classmates and friends in Berkeley and San Francisco who have become a second family to me in the bay area and without which I am certain I would not have remembered how important it is to live life to the fullest.

I would like to thank the incredible group of colleagues in the Roorda Lab who have supported my work directly and indirectly. In particular, I would like to thank Pavan Tiruveedhula for all his amazing work keeping the AOSLO operational and ensuring that all the technical aspects of the new experiments I wanted to implement became a reality. I would also like to thank Wolf Harmening, Christy Sheehy, William Tuten, Brandon Lujan, Lawrence Sincich, Johnny Tam, and Ethan Rossi for their support over the years.

Finally, I would like to thank my scientific mentors David Williams and Austin Roorda. I am extremely grateful to have had the opportunity to work for David Williams, who remains an inspiration as a brilliant researcher and kind person. As an undergraduate interested in optics and vision research, I will forever appreciate the fact that I was welcomed into his group at that crucial point in my education. The fact that he has remained willing to lend an ear and offer advice and insight as well as continued support and belief in me has been crucial to my development as a scientist and researcher. I would lastly like to thank my advisor Austin Roorda who has helped me grow and challenged the way I think about scientific problems. He is also an inspiration and has brought together an amazing group of diverse and talented people through collaborations in and outside of the lab in Berkeley. I am grateful to have had the opportunity to learn from him.

CHAPTER 1: IMAGING THE HUMAN FOVEA

The Anatomical Structure of the Fovea

The retina is the light-sensitive tissue that lines the inner surface of the human eye. It is a multi-layered neural structure. There are millions of photoreceptors towards the back that collect the light that enters the eye, serving as the first step of our visual percepts of the world. Most of the photoreceptors in the retina, approximately 120 million, are rod photoreceptors which are primarily responsible for light detection under dim conditions. The remaining 6-7 million are cone photoreceptors, which are responsible for color vision and daylight tasks. They are used for tasks that require good resolution such as reading because they are tightly packed along the line-of-sight at what is called the fovea. In this area of the retina, there are only cone photoreceptors present and they achieve their peak density. There is also a noted absence of blood vessels in the fovea and a cross-sectional view of the retina shows a dip or pit, which is where the name fovea comes from (Dowling, 1987; Polyak, 1941).

Figure 1 shows images of the retina obtained using the commercial Cirrus HD-OCT system (Carl Zeiss Meditec, Inc, Dublin CA). The background shows the image from a line scanning ophthalmoscope (LSO) used to obtain an *en-face* view of the retina, Figure 1 (A), and the corresponding cross-sectional view of the retina obtained with Optical Coherence Tomography (OCT), Figure 1 (B). The LSO image show salient features such as the blood vessels and the optic nerve head (the area where the axons of the retinal nerve fibers exit the eye). The OCT image corresponds to the 6mm vertical section labeled in green through the center of the fovea. This image clearly shows the distinct retinal layers and a pit corresponding to the location of the fovea.

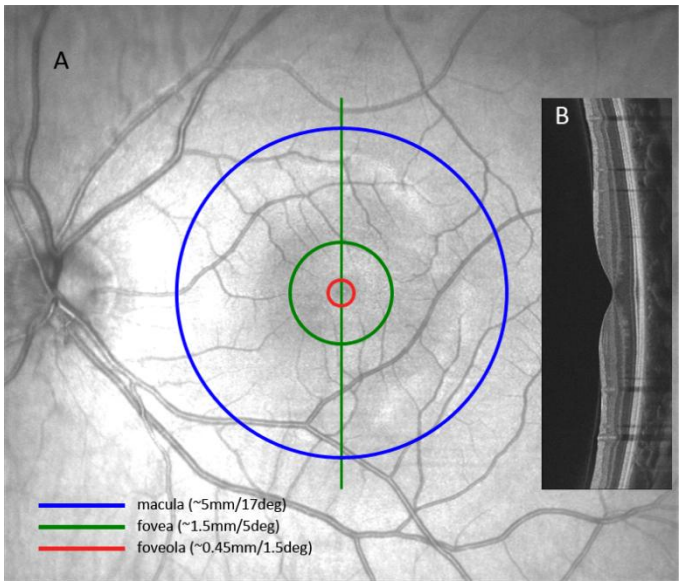

Figure 1: SLO (A) and OCT (B) images of the macula for a normal subject. For the left eye of a normal subject, the green vertical line labels a 6mm section corresponding to the location of the OCT image on the right side.

These images illustrate that imaging can play a large role in understanding the structure of this specialized area of the retina. Figure 1 also illustrates the names and sizes of the increasingly specific regions of this central area of the retina. The entire central region is typically referred to as the macula (~5 mm/17 degrees), zooming in we see the area that is referred to as the fovea (~1.5 mm/5 degrees), and zooming in even further reveals the foveola (~0.45 mm/1.5 degrees). Historically, the center of the fovea has been identified in similar images using the foveal pit, the location of the foveal avascular zone (FAZ), or the distance from the optic disk. When we zoom in to image the very center of the foveola at high resolution, optical imperfections, or aberrations, in the human eye limit our ability to see the individual photoreceptor cells under normal conditions. This leads to the need for a technology to compensate for an individual's aberrations, such as Adaptive Optics (AO), which will be discussed more in the next section. Obtaining high-resolution images of this region also allows for the identification of the foveal center using other anatomical features such as the noted absence of rod photoreceptors and the peak of cone photoreceptor density.

Imaging and Resolution Limits

Even in a perfect imaging system, there are optical limits to resolution due to the diffraction of light at limiting apertures. The intensity distribution of a point through a circular aperture forms what is called an Airy disk, in which most of the light is concentrated in the center with rings of light with decreasing intensity. A simple equation for the diameter (D) of the Airy disk follows:

$$\mathbf{D = 2.44\,\lambda\,f/\#_W} \qquad \text{Equation 1}$$

The implications of Equation 1 are that there are a few major factors that determine the size of the Airy disk, the imaging wavelength (λ) and the working f number ($f/\#_W$) of the system, which corresponds to the system focal length (f) divided by the diameter of the imaging aperture (d). In a system with multiple points of light, we can use the Rayleigh criterion for angular resolution in radians as follows in Equation 2:

$$\textbf{Rayleigh Criterion for Angular Resolution} = \frac{1.22\lambda}{d} \qquad \text{Equation 2}$$

As a result, there are two major factors that limit angular resolution in a perfect optical system. The first is the imaging wavelength (λ) and the second is the diameter of the imaging aperture (d) (Born & Wolf, 2000; Greivenkamp, 2003).

In a typical human eye, the optical system is not perfect. The imperfections are called aberrations and their effect on the distribution of intensity in the image can be described by a Point Spread Function (PSF). Figure 2 illustrates the diffraction-limited Airy disks corresponding with imaging in a perfect eye compared with an example from a normal aberrated eye for a range of biological pupil sizes. In a typical eye, imaging is close to diffraction-limited up to

approximately a 3mm pupil after which imaging is much worse despite the fact that the Rayleigh Criterion for resolution gets better with increasing pupil size.

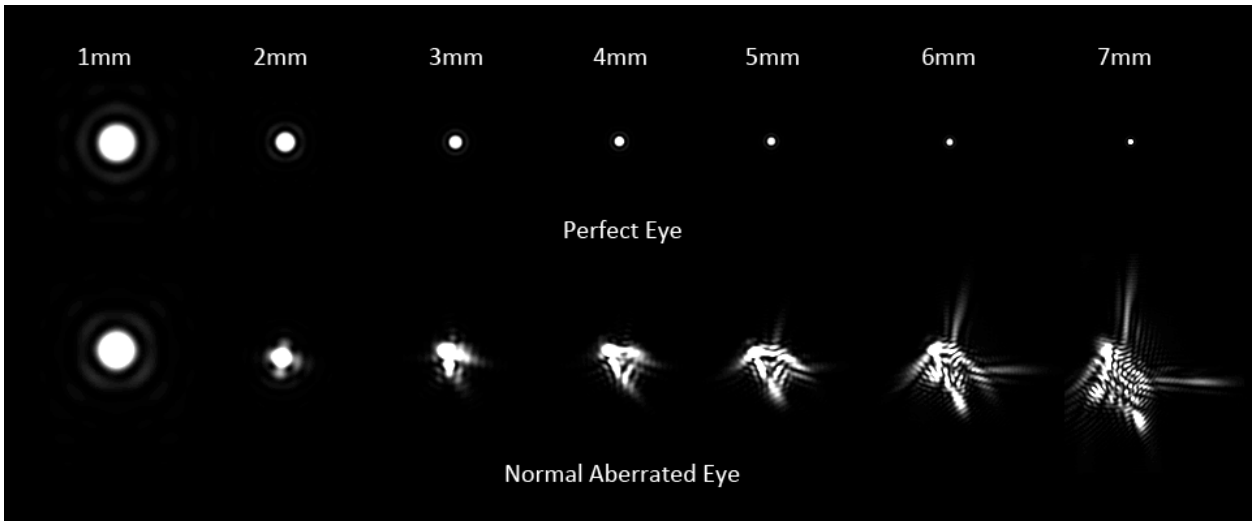

Figure 2: Point Spread Functions (PSFs) for a range of biological pupil sizes. Top: Simulated PSFs for a perfect eye Bottom: Simulated PSFs for a normal (aberrated) eye. (Figure adapted from Austin Roorda's class notes.)

There are also anatomical differences between foveal and para-foveal cones. Cone photoreceptors are smallest at the center of the fovea, approximately 2.5 microns or 0.5 arcmin, and cone density reaches a peak. Histological studies reported an average of 191,000 cones/mm^2 (range 98,000-324,000 cones/mm^2) and stated that density was an order of magnitude lower just outside the foveola at 1 mm or approximately 3.33 degrees eccentricity (Østerburg, 1935; Curcio et al., 1990). The challenge of reliably resolving all the cones in the central fovea with AOSLO stems from their small size and dense packing coupled with blur and interference artifacts from the imaging system. The imaging of foveal cones is challenging even with flood-illuminated systems due to the unique anatomical structure of the smallest foveal cones which are said to be more rod-like and exhibit minimal taper at the inner segment (IS)/outer segment (OS) junction compared with more peripheral cones which may impact imaging (Borwein, 1983; Dowling, 1987; Polyak, 1941; Walls, 1942; Schultze, 1873). There is an illustration in Dowling's book, modified from Walls, that illustrates the belief that the foveal cones exhibit minimal taper and look more like a rod than a typical cone. Together, these factors have led many psychophysical studies that examine the relationship between cone structure and functional vision to be focused further out around 1 degree eccentricity where cone density is less variable and cone size is large enough to be easily resolved with current instruments.

Adaptive Optics

Adaptive Optics (AO) was first proposed in the 1950s for astronomical applications in order to compensate for dynamic atmospheric turbulence distorting images of distant stellar objects taken from ground-based telescopes (Babcock, 1953). The principle of AO is fairly simple: one

must first determine the profile of the distortion and then implement a correction. There are many problems and solutions associated with both aspects, but the typical implementation includes the use of a wavefront sensor (WFS) to measure the system aberrations and the use of a deformable element, typically a deformable mirror (DM), to compensate for those measured optical imperfections in order to reach close to diffraction-limited imaging performance.

Decades after AO was proposed and implemented by the astronomical community, a DM was first used in the human eye to compensate for one subject's previously measured astigmatic refractive error (Dreher, Bille, & Weinreb, 1989). By the late 1990s, the technology was employed in conjunction with a Shack-Hartmann wavefront sensor (SHWS), which was used to compute the high-order aberrations in a living eye, and compensate for both the low-order and high-order aberrations of the human eye by researchers at the University of Rochester. That first ophthalmic AO system was a flood-illuminated ophthalmoscope that took images using 550nm light and was able to resolve images of individual cone photoreceptors in the normal human eye (Liang, Williams, & Miller, 1997). An updated version of Rochester's flood-illuminated ophthalmoscope was later used to resolve complete foveal cone mosaics in some subjects (Putnam et al., 2005).

AO Scanning Laser Ophthalmoscopy

AO was first incorporated into a Scanning Laser Ophthalmoscope (SLO) system in the early 2000s (Roorda et al., 2002). The AOSLO is a confocal system, which provides a number of benefits including improved theoretical resolution, higher contrast imaging, and axial sectioning (Wilson & Sheppard, 1984). AOSLO also has numerous advantages over a flood-illuminated system including the acquisition of images at video rates and the ability to encode dynamic stimuli directly in the imaging beam (Poonja, Patel, Henry, & Roorda, 2005). This stimulus presentation feature makes AOSLO an extremely useful tool in psychophysical studies, unambiguously recording stimulus locations in the resulting images, leaving a direct record of the stimulated photoreceptors. Since the AOSLO is a scanning system, the image is built point by point resulting in a 512x512 pixel video of a square patch of retina up to approximately 2 degrees on a side. The addition of an acousto-optic modulator (AOM) to the input beam allows the imaging source to be modulated, switched on and off, allowing stimuli to be encoded directly in the imaging beam by modulating the laser at certain locations in the beam. A dark stimulus is encoded by turning the imaging beam off or an additional source of a different wavelength may be used simultaneously to present a bright stimulus at the desired locations. In the case of a dark stimulus, the operator then sees a cone mosaic with a dark region corresponding to the stimulus location and the subject views the imaging raster with a dark stimulus, which is illustrated in Figure 3.

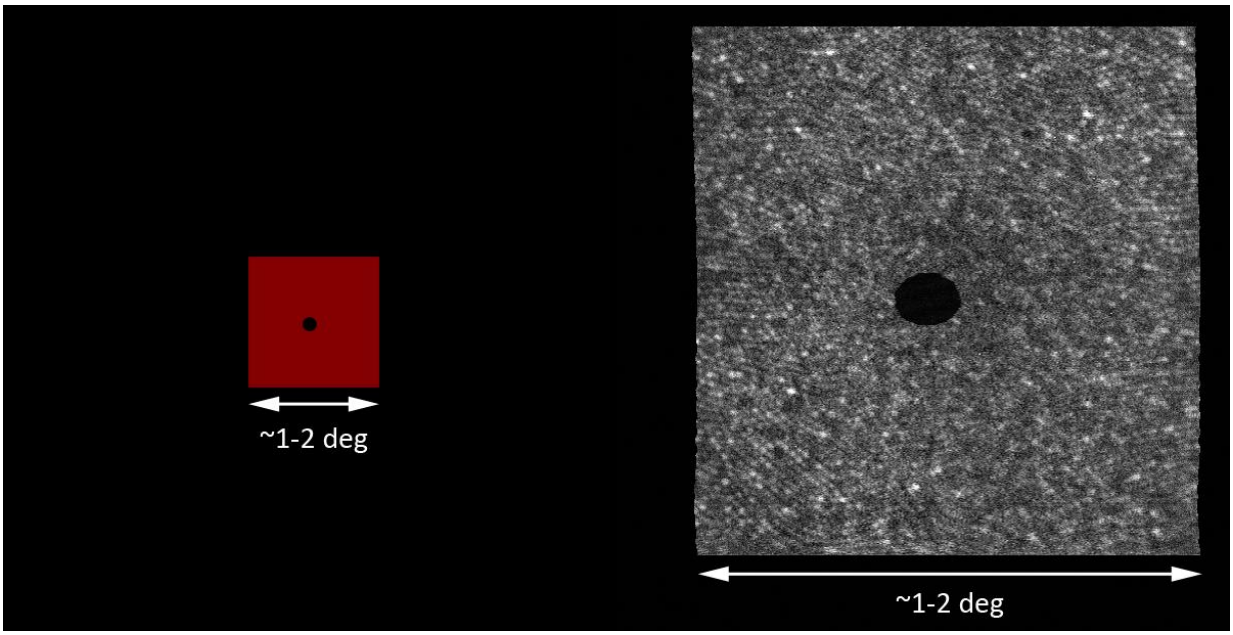

Figure 3: Example subject and operator views when imaging with AOSLO. The left side of the figure illustrates the subject's view of a red square with a dark circular visible stimulus. The small red square is meant to illustrate the point that the field is small (typically 1-2 degrees). The right side of the figure illustrates the operator's view of a high-resolution retinal image with a dark circle corresponding to the location of the visible stimulus.

Fixational eye movements and AOSLO image stabilization

The eye is always moving, even during steady fixation. The small, involuntary fixational eye movements persist during sustained fixation and are typically broken down into three major types based on their characteristics. Microsaccades are the largest and fastest. It has been proposed that they serve the purpose of correcting the displacement of images due to the second type of fixational eye movement, drifts, such that objects of interest return towards the center of the fovea. Drifts are a steady, slower motion that occurs between microsaccades. It has been proposed that drifts are produced by instability in the fixation system, but it has also been proposed that they have a role in preventing image fading and retinal fatigue. It is also possible that the drifts also play a role in correcting fixational errors and returning objects of interest to the fovea. Finally, tremor is a high-frequency (~90 Hz) motion that is superimposed on the slow drifts (Martinez-Conde, Macknik, & Hubel, 2004). Recent work has also suggested that drift and microtremor are distinctly different components of eye motion, but are the low and high frequency components of the same, roughly 1/f, spectrum (Stevenson, Roorda, & Kumar, 2010).

When all motion of a stimulus is removed leaving it fixed on the retina, it has been shown to fade from view. Images in a fixed retinal location lead to visual adaptation of the sensory neurons whose response declines with prolonged exposure to a static stimulus (Barlow, 1997; Barlow, 1952; Hubel & Wiesel, 1959; Macedo, Crossland, & Rubin, 2008; Martinez-Conde et al.,

2004). This is true for both entoptic stimuli such as the blood vessels that lie in front of the photoreceptors as well as stimuli that are stabilized on the retina using external equipment. This highlights an important role of fixational eye movements in vision.

In order to visualize the smallest foveal cones, it is necessary to implement good stabilization software. In addition to off-line stabilization of images, the Berkeley AOSLO has the ability to stabilize retinal images in real time (Arathorn et al., 2007; Vogel, Arathorn, Roorda, & Parker, 2006). In order to track the retina in real time, 16 pixel strips of the image are registered with a reference frame acquired earlier in the imaging session. The x and y displacements of the strip are used to register the current strip with the reference frame and provide a direct measure of the retinal motion. In addition to correcting eye movements to provide a stabilized image, the stimulus may be placed at a targeted retinal location within the imaging frame by using the eye position signal to guide the timing for the modulation of the scanning laser. An image stabilization and targeted stimulus delivery interface was developed in order to deliver stimuli to specific retinal locations and/or manipulate their motion in a variety of psychophysical tasks. This capability has been used to target and stabilize a stimulus on a particular cone or area regardless of eye motion (Sincich, Zhang, Tiruveedhula, Horton, & Roorda, 2009), but may also be used to manipulate the stimulus motion to any desired trajectory related to or independent of the natural eye motion. The lag between eye motion predication and stimulus delivery is as small as 2-4 msec with an accuracy of 0.15 arcmin (Yang, Arathorn, Tiruveedhula, Vogel, & Roorda, 2010). A lag time around 6-8 msec was typically used in order to improve the consistency and robustness of the stimulus presentation, but it should be noted that this is still smaller than the highest frequency component of jitter and drift movements (~10msec).

There are limitations to this stabilization, however, due in part to the small field size used for AO imaging (~2 degrees). As a result, most of the smaller, continuous drift movements are easily stabilized along with some microsaccades and it becomes interesting to focus on the periods of steady drift. In addition to image stabilization, this real-time strip-based stabilization method allows for targeted stimulus delivery within the imaging frame.

OVERVIEW OF THE STUDIES IN THIS DISSERTATION:

Chapter 2: Modeling the Foveal Cone Mosaic Imaged with Adaptive Optics Scanning Laser Ophthalmoscopy

Cone photoreceptors reach their peak density near the center of the fovea, which corresponds to a cone spacing that is at or near the theoretical optical imaging resolution limits. There are fundamental limits imposed by pupil size, the power of the eye, and the system imaging wavelength. Other limits are imposed by foveal cone structure, which leads to less scattered light to detect, and eye motion, which imposes a need to stabilize the images since small residual motion will have a large effect on small structures. A combination of improved AO control, image stabilization, and the use of optimized field sizes improves the chances of resolving a continuous mosaic of foveal cones. This chapter presents a model developed to

understand the impact of different theoretical imaging limitations with our specific imaging modality (AOSLO), the performance of current imaging systems, and imaging developments.

Chapter 3: Comparison of Anatomical and Functional Measures of the Normal Human Fovea using Adaptive Optics Scanning Laser Ophthalmoscopy

Structure-function relationships are important in order to understand more about the microscopic anatomical images obtained with AOSLO. At this scale, there is a need to define things differently and a combination of structural and functional markers will provide more insight than either alone. We first obtain high-resolution images of the center of the fovea and estimate the point of peak density from cone density measurements. We then test two functional measures of the fovea. The first functional measure of the fovea is the preferred retinal locus of fixation (PRL), where many samples of the location used for fixation are taken from a continuously moving video of the retina. The standard deviation of these points is comparable with a measure of fixation stability from Steinman and Ditchburn's seminal studies (Ditchburn & Ginsborg, 1952; Steinman, Haddad, Skavenski, & Wyman, 1973). More recent measurements made in AO Ophthalmoscopy studies sampled this continuous fixation with isolated points sampled from the motion trajectory and were able to record those retinal locations targeted by fixation (Putnam et al., 2005). In this chapter, we compare the mean locations from a sample of 100 videos in order to compare both the variance in individual videos and the mean locations in order to compare with previous studies. The second functional measure of the fovea is the preferred fixation direction (PFD), the retinal locations corresponding to the perception that a target is in the direction of fixation. We measure both the PRL and the PFD on two separate days and compare the retinal loci with an estimate of the anatomical center of the fovea from our high-resolution images in both eyes of three subjects.

Chapter 4: The Role of Natural and Manipulated Fixational Eye Movements in Foveal Vision

Spatial vision tasks are typically differentiated from temporal vision tasks, with spatial vision describing the "distribution of light across space and the perception of the location of visual objects within three-dimensional space" (De Valois & De Valois, 1980). This description and the typical treatment of spatial vision tasks neglects the often integral temporal component induced by the constant motion of the eye, even during steady fixation. Acuity thresholds have been shown to decrease with increasing exposure time up to and potentially beyond 400 ms (Baron & Westheimer, 1973). As a result, in order to fully characterize and understand the spatial aspects of foveal vision, it is also important to consider temporal aspects of stimulus presentation even during what are typically considered spatial tasks. We are interested in understanding the role of different components of retinal image motion in these spatial vision tasks and the circumstances under which they impair or enhance our visual performance.

Objects in the natural world appear stable despite constant retinal image motion during fixation. Previous studies have shown that increasing the magnitude of retinal image motion in a direction consistent with natural eye motion does not have an effect on the perceived image stability (Stevenson et al., 2010). In contrast, cancelling out the retinal image motion leads to a percept of image motion before the object fades away from view due to the lack of motion.

Finally, presenting a magnitude of retinal image motion that is equal to that of the natural motion but in the opposite direction leads to the percept of a highly unstable object. It is clear that the direction of retinal image motion plays an important role in producing a stable percept of the world, but we are also interested in the role that it plays in different spatial and temporal acuity tasks.

In addition to the fact that objects that are constantly moving across the retina appear stable, when objects are fixed on a single retinal location, they actually fade from view. This fading of retinal images is a visual phenomenon that occurs when neurons in the visual system become adapted to a stimulus. Troxler's fading refers to the phenomenon where stimuli that are in the periphery disappear when someone fixates on a point for a few seconds (Martinez-Conde, Macknik, Troncoso, & Dyar, 2006). In this case, small fixational eye movements drive stimulus motion and are small enough that the retinal image changes in the periphery are not large enough to produce visual signals. Fading has also been shown for images that are stabilized on the retina with specialized laboratory equipment (Ditchburn, Fender, & Mayne, 1959; Riggs, Ratliff, Cornsweet, & Cornsweet, 1953; Steinman & Levinson, 1990). Riggs et al. tested stimuli as thin as 5.8 seconds of arc up to 93.3 seconds of arc and demonstrated fading of thin lines within seconds and reported that they would stay faded for the remainder of the 60 second trial with larger stimuli taking both longer to disappear and often reappearing. Ditchburn et al. discussed the fading of a larger stimulus a few arcmin in width stabilized in the center of the fovea, noting that the bar would disappear and reappear with a median time around 5 seconds. They noted that stimuli were seen for only approximately 2 seconds of that 5 second interval. Overall in these reports, there is much discussion of the disappearance and reappearance of stabilized images, with a time course that depends on retinal location, stimulus size, and contrast. For larger stimuli presented foveally fading was slower and not sustained compared with smaller stimuli presented eccentrically.

A. Measurement of Motion Detection Thresholds

The goal of this first set of experiments is to understand how our ability to detect very small amounts of motion relates to the spatial manipulation of the motion trajectory on the retina. We make quantitative measurements of motion detection thresholds in order to help understand the role that stimulus motion plays during this visual task. Subjects made a 2AFC judgment of clockwise or counterclockwise motion for a small circular stimulus with a 0.5 or 1.5 cycle circular motion path added to either the natural and existing eye motion or a manipulation of that eye motion. For example, in the natural case with eye motion due to fixational eye movements, the stimulus trajectory was nearly perfectly circular in space, but was the sum of the natural eye motion and the circular imposed motion on the retina. In the case where the natural eye motion was ignored or stabilized, the stimulus trajectory was nearly perfectly circular about a fixed retinal location. We test conditions including normal eye motion and manipulated motion trajectories in the same direction and opposite direction as natural eye motion using stimulus motion control with AOSLO.

B. Measurement of Contrast Thresholds and the Role of Fading

The goal of this second set of experiments is to understand the role of natural and manipulated fixational eye movements on contrast sensitivity and the role that motion plays in image fading. In order to measure the impact of these small fixational eye movements on image contrast thresholds, we utilized the AOSLO's image stabilization and targeted stimulus delivery interface to create a test in which the contrast of a small grating increased over time. Subjects were instructed to look at the center of blank imaging field and were presented with a cued location for 0.33 seconds upon starting the trial with a button press. They were then instructed to attend to that retinal location very close to fixation and judge grating orientation as soon as they were able to make a judgment (2AFC right or left) and the contrast at the time of button press was measured. This task was performed under natural, stabilized and manipulated eye motion conditions. We also looked at the time-course of image fading for naturally moving, stabilized, and conditions in-between with small stimuli near the fovea. In this experiment, subjects were instructed to fixate on the corner of the red imaging raster and initiated a trial with the press of a button. A small 100% contrast grating was presented at a random location within the imaging field and subjects were instructed to press one button when the stimulus was no longer visible or to press another if the 9 second trial concluded with no image fading. We measured the time the stimulus was visible and the percentage of trials where the stimulus was visible for the entire 9 second trial under natural, stabilized, and manipulated motion conditions between natural and stabilized.

CHAPTER 2: MODELING THE FOVEAL CONE MOSAIC IMAGED WITH ADAPTIVE OPTICS SCANNING LASER OPHTHALMOSCOPY

ABSTRACT

To better understand the limitations of high-resolution adaptive optics scanning laser ophthalmoscopy (AOSLO), we describe an imaging model that examines the smallest cone photoreceptors in the fovea of normal human subjects and analyze how different factors contribute to their resolution. The model includes basic optical factors such as wavelength and pupil size, and defines limits caused by source coherence which are specific to the AOSLO imaging modality as well as foveal cone structure. The details of the model, its implications for imaging, and potential techniques to circumvent the limitations are discussed in this paper.

INTRODUCTION

Adaptive optics scanning laser ophthalmoscopy (AOSLO) has been used for a decade to produce high-resolution images of microscopic retinal structures in the living eye (Roorda et al., 2002). AOSLO imaging has a number of features which make it an appealing choice for both clinical and basic science applications, including the ability to axially section retinal layers, the capability to encode dynamic stimuli directly in the imaging beam, and the ability to study fixation, acuity, sensitivity, or other metrics of visual performance at video-rate while simultaneously visualizing retinal cells (Poonja et al., 2005; Roorda, 2010; Rossi & Roorda, 2006; Rossi & Roorda, 2010a; Rossi, Weiser, Tarrant, & Roorda, 2007; Stevenson & Roorda, 2005; Stevenson, Kumar, & Roorda, 2007; Zhang & Roorda, 2007).

AOSLO is the method of choice for the study and characterization of the normal functioning retina, specifically the central foveola with its critical role in normal dynamic visual tasks such as reading. Questions regarding the structure and function of the foveal center could be better answered with the use of real-time microscopic imaging with AOSLO. Previous AOSLO studies, for example, characterized the retinal locations targeted by different eye movement systems by identifying and comparing the preferred retinal locus for pursuit eye movement tasks, saccadic eye movement tasks, and for steady fixation (Stevenson et al., 2007). Interestingly, they found that preferred retinal loci for these tasks were not necessarily in the same location. A limitation to these studies, however, was the lack of resolution of the smallest cones in the central fovea, resulting in the inability to relate these loci to the peak cone density position. The ability to characterize the anatomy, resolve the smallest foveal cones, and compare these to functional measures such as detection and acuity will aid our understanding of the capabilities and limitations of the functioning fovea.

Despite steady improvement in AOSLO systems over the years (Arathorn et al., 2007; Burns, Tumbar, Elsner, Ferguson, & Hammer, 2007; Grieve, Tiruveedhula, Zhang, & Roorda, 2006; Morgan, Dubra, Wolfe, Merigan, & Williams, 2009; Zhang, Poonja, & Roorda, 2006a; Zou, Qi, & Burns, 2008), the difficulty of resolving all the cones in the central fovea remains. This is mainly due to their small size and dense packing but also, as we will describe in this paper, as a result of their unique anatomical structure, which is said to be more rod-like compared with more

peripheral cones (Dowling, 1987; Schultze, 1873; Walls, 1942). In the past year, we reported a few cases where the entire cone mosaic in a healthy normal retina has been resolved with AOSLO (Li, Tiruveedhula, & Roorda, 2010), but typically the smallest cones within the central ~0.1 degree remain difficult to resolve even under the best conditions.

In non-scanning, flood illumination CCD-based systems that use incoherent light, it seems that the entire foveal cone mosaic can be imaged more routinely, as evidenced by reports from the AO Ophthalmoscope at the University of Rochester (Putnam et al., 2005). Both systems are designed to have similar theoretical resolution limits, which led us to implicate additional limits to AOSLO resolution resulting from the partial coherence of the light source. In fact, we've already reported that the fidelity of AOSLO images improved greatly when we used a low coherent light source (Zhang, Poonja, & Roorda, 2006b).

In order to better understand and devise ways to overcome the factors limiting performance in AOSLO imaging, we developed an accurate model of foveal cone imaging that considers basic optical factors such as wavelength, pupil size, and the formation of an image with a scanning laser system. The model focuses primarily, however, on the impact of source coherence, a factor that is specific to the AOSLO imaging modality.

METHODS

The following sections outline the development of a model of foveal cone imaging that will ultimately lead to simulated AOSLO images of the photoreceptor mosaic. We first consider where the light originates in an AOSLO image of a cone and measure the relative magnitude of the contributions. Second, we develop a model of how neighboring cones interact when illuminated with coherent light. Third, we define a cone mosaic, drawing from existing anatomical measures. Finally, we describe how to construct images point-by-point through raster scanning or conventional imaging using light sources with different degrees of spatial and temporal coherence.

Where does the light come from in an AOSLO image of a cone?

We expect that *en-face* AO images of photoreceptors, including those taken with AOSLO, are best resolved when the optical focus is at the anterior tips of the inner segments, consistent with the location of the external limiting membrane (ELM). This is because this corresponds to the anatomic axial position where light emerges from the fiber-optic portion of the photoreceptor (Laties & Burnside, 1978). The light emerging from this aperture originates from two primary reflections that occur within the optical fiber component of the photoreceptor, the first from the inner-segment/outer-segment (IS/OS) junction and the second at the posterior end of the OS. These sources are readily seen in OCT B-scan images whose imaging mechanism is designed to reveal the relative optical path lengths of light returning from the retina. We know that these sources of reflections within cones contribute to AOSLO cone images because:

1) AOSLO and flood-illuminated AO images of the cone mosaic exhibit the same waveguiding properties as the IS/OS and OS layers in OCT (Gao, Cense, Zhang, Jonnal, & Miller, 2008; Roorda & Williams, 2002);
2) The magnitude of light measured from AOSLO and flood-illuminated AO images of cones is affected by visual pigments that reside in the outer segment of the cone (Roorda & Williams, 1999); and
3) There is apparent interference between the two primary sources of reflection in flood-illuminated AO retinal images (provided that the right type of light source is used) (Jonnal et al., 2007).

As such, our model considers each cone as a point source with an intensity weighted by the relative intensities from the two sources of reflections within the cones.

The relative contributions of the sources of reflection within the cones are not constant however. While the reflection at the OS tips are nearly uniform across the macula, there is a decreased reflection of the IS/OS junction near the base of the foveal pit. We suspect that this decreased reflectance in the central fovea is due to the unique anatomical structure of the cone photoreceptors at the foveal center, which exhibit a minimal taper at the IS/OS compared with more peripheral cones (Borwein, 1983; Dowling, 1987; Polyak, 1941; Schultze, 1873; Walls, 1942).

OCT measurements of foveal cone reflectance

To quantify the reflectance signal from different retinal layers, we examined OCT raster scans (256(L) x 256(W) x 1024(H), acquired in ~4 sec.) and horizontal OCT cross-sectional images through the fovea for 9 subjects aged 18-51 yrs old (median age = 25 yrs old). The OCT scans were acquired with an AO-SDOCT system described previously (Bigelow et al., 2007). We averaged 50 axial profiles at several retinal eccentricities up to 1 deg. For each profile, the ratio of the reflectance of the posterior tips of the outer segments to the layer corresponding to the IS/OS junction was measured. The fovea was located by the appearance on the images of the pit, the foveal reflex, and the increased separation between the signal from the IS/OS junction and that from the posterior tips of the OS (indicative of cone elongation associated with packing in the fovea). For comparison of reflectance signals, the customary logarithmic scaling – normally used to accentuate dim anterior layers – was eschewed in favor of linear scaling. Figure 4 (a) shows a retinal image linearly scaled with an inverse gray-scale color map. The arrow shows the location of the fovea where the IS/OS junction signal is attenuated. Figure 4 (b) shows an OCT image (composite of 5 co-added frames) with typical logarithmic reflectance scaling and gray-scale color map. The boxes in Figure 4 (b) show two regions where the profiles were averaged, one centered on the fovea and one centered at 1 deg. The corresponding profiles are shown in Figure 4 (c).

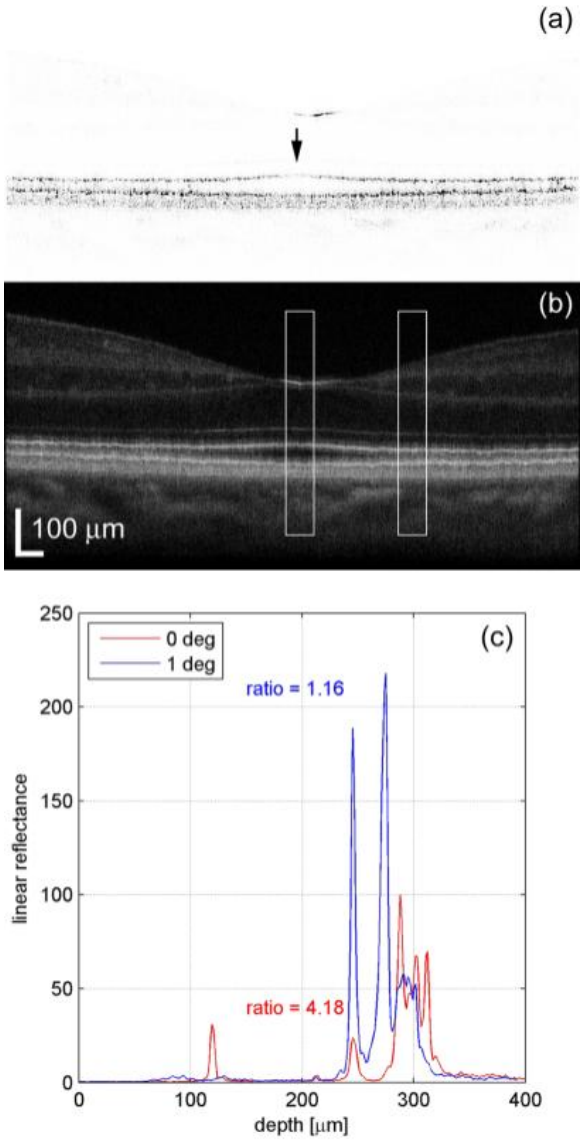

Figure 4: Reflectance measurements from OCT images. (a) Single linearly scaled OCT image illustrating attenuation of the IS/OS junction layer (arrow). (b) Composite OCT image showing regions over which the profiles were averaged (boxes). (c) Profiles from the regions in (b). In this case the ratio of reflectance at the posterior tips of the OS divided by reflectance at the IS/OS junction at the fovea was 4.18 and at 1 deg was 1.16.

Figure 5 shows an *en-face* OCT image through the fovea of one subject where individual retinal layers through the photoreceptors have been summed using a projection view of the layer containing the IS/OS junction (Figure 5 (a)) and the layer containing the posterior tips of the OS (Figure 5 (b)). The mottled appearance of the image in Figure 5 (a) is due to the cones, although the mosaic is not completely visible because of eye motion during the relatively slow OCT raster. The decreased reflectivity in the region within 0.5 deg of the fovea is clearly visible (arrow) in Figure 5 (a) while Figure 5 (b) does not show a comparable decrease in reflectivity.

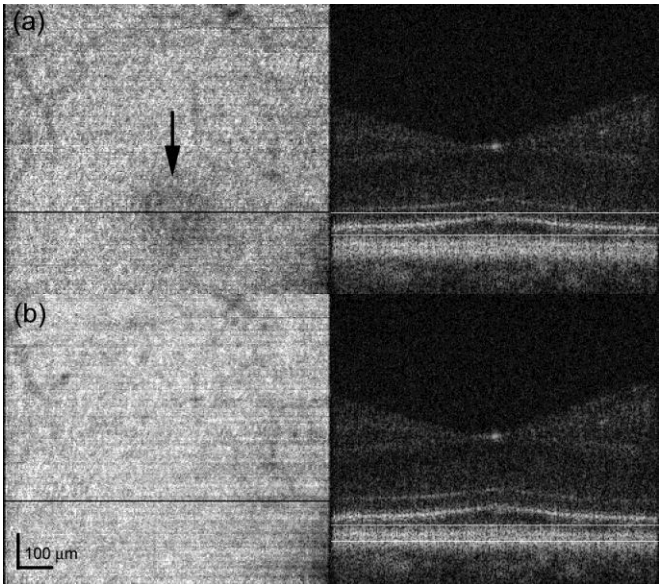

Figure 5: *En-face* OCT images at the photoreceptor layers (left) and corresponding summed layers shown in cross-sectional image through the fovea (right). (a) Composite image created from 27 depth slices through the IS/OS junction layer. Decreased reflectivity within 0.5 deg of the fovea is clearly visible (arrow). (b) Composite image created from 15 depth slices through the posterior tips of the OS.

To quantify the decrease in reflectivity for all subjects, we analyzed the horizontal cross-sectional scans. Figure 6 shows the average linear reflectance ratio between the photoreceptor layers (IS/OS junction and posterior tips of the OS). At eccentricities greater than 0.5 deg, the ratio between photoreceptor layers approaches 1. The attenuation of the IS/OS layer signal caused an increase in the reflectance ratio at eccentricities less than ±0.5 deg in all subjects. The average ratio was approximately 2.5 times higher at the fovea compared with eccentricities greater than 0.5deg (min = 1.94 and max = 3.55).

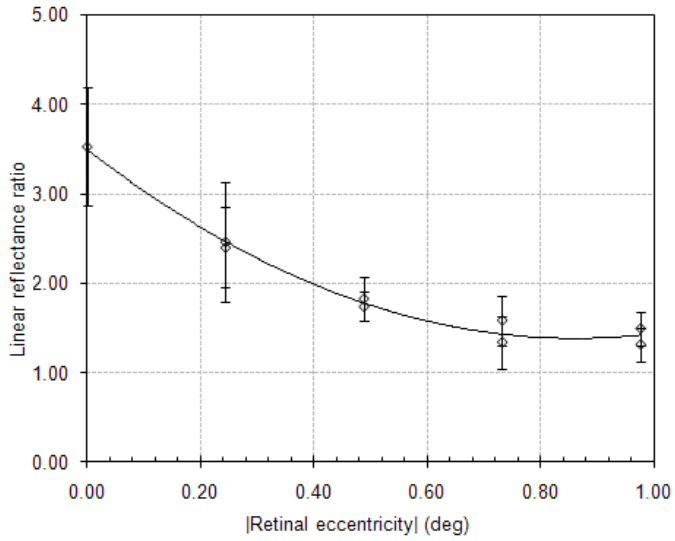

Figure 6: Increase in reflectance ratio associated with IS/OS layer attenuation in the central fovea. Average values for 9 subjects.

A polynomial fit to the data in Figure 6 was performed using Microsoft Excel and is expressed with Equation 3, where r is retinal eccentricity in degrees. This fit is shown in Figure 6.

$$weight = 2.8532r^2 - 4.9122r + 3.4963. \qquad \text{Equation 3}$$

This polynomial curve fit is only accurate for the range of data shown in Figure 6, a region extending approximately 1 degree away from the foveal center. In this way, the intensity of the reflection from the IS/OS junction in the region with the highest cone density contributed approximately 3.5 times less than the reflection from the posterior tips of the OS while in contrast cones out as little as 0.5 degrees only contribute approximately 1.5 times less. AOSLO images and flood-illuminated AO ophthalmoscopy images of the foveal cone mosaic are taken with the instrument focus at the anterior tips of the inner segments of the photoreceptors (at the level of the external limiting membrane), with the light collected being the sum of the two *en-face* OCT images shown in Figure 5. As a result, the weight of an individual cone would in general be proportional to a contribution defined by the inverse of the weight defined by Equation 3 from the IS/OS junction plus a constant intensity contribution from the posterior tips of the OS. In our model, the center of the fovea is defined by using automated software to determine the point with maximum cone density and *r* is then the distance to the cone with maximum density (Li & Roorda, 2007). In real images there are individual variations in the intensity of light emitted from cones, but this function describes only the overall variation seen in the foveal center (Pallikaris, Williams, & Hofer, 2003).

The impact of source coherence

Cone photoreceptors are known to act as waveguides. As stated earlier, the light scattered from the IS/OS junction and the posterior tips of the OS are summed and emerge at the anterior tips of the IS. Since their size (Curcio, Sloan, Kalina, & Hendrickson, 1990), and behavior (Gao et al., 2008; Roorda & Williams, 2002; Westheimer, 1967), is consistent with the cones being single mode fibers, we can consider each as an isolated point source for AOSLO and AO ophthalmoscopy imaging (Enoch, 1963; Roorda & Williams, 2002). Figure 7 is an illustration of two adjacent cones and the points of reflections that contribute to the AOSLO and AO ophthalmoscopy images.

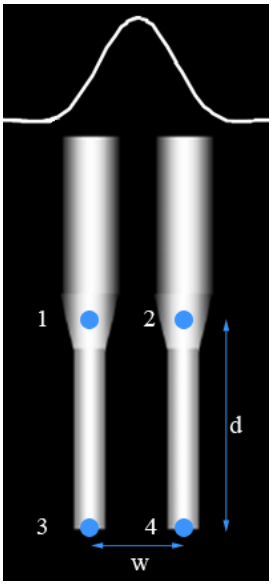

Figure 7: Illustration of the scattering points within neighboring cone photoreceptors. Two neighboring cone photoreceptors with a cross section of a point spread function illustrated at the tips of the inner segments, where the instrument would be focused during imaging. Each cone acts as a point source with the points of reflection that contribute to the output labeled in the figure. Points 1 and 2 scatter from the IS/OS junction and points 3 and 4 scatter from the posterior tips of the OS. The distances between adjacent photoreceptors, *w*, and between the two layers of reflection, *d*, combined with properties of the imaging source determine the extent to which inference artifacts are seen in the image.

The distance *d* in Figure 7 between the IS/OS junction and the tips of the OS is in the range of ~33-38 µm in the central fovea (Hermann et al., 2005; Polyak, 1941). It has been shown that when the coherence length spans the optical path difference between these two layers, *d*, interference can occur between points 1 and 3 and points 2 and 4 in Figure 7 (Jonnal et al., 2007). This interference is the result of temporal coherence artifacts and is not observed if the source bandwidth is large enough. In the AOSLO, we use a broadband superluminescent diode (SLD) centered at 840 nm with bandwidth of approximately 50 nm coupled to a single-mode fiber (Broadlighter S840, Superlum, Russia). The coherence length inside the cone photoreceptors is calculated to be approximately 4.35 µm, which is much shorter than the distance *d* (Jonnal et al., 2007; Zhang et al., 2006b). The distance *w* in Figure 7 between adjacent cones in the central fovea is approximately 2-3 microns or 0.5 minutes of arc, which is large enough to resolve the cones under typical imaging conditions, but the AO-corrected illumination spot does cover more than one cone, as does the secondary image of the cones formed at the confocal aperture.

Each cone photoreceptor is considered to be a point source. In the confocal pinhole plane of the AOSLO, the image of each point takes the following form, which when multiplied by its complex conjugate corresponds to a diffraction-limited Airy disk:

$$\vec{E}_j(r) = c\vec{E}_o \frac{2J_1(kr_j)}{kr_j} \exp(-i2\pi\phi(t)_j). \qquad \text{Equation 4}$$

In Equation 4, *c* is a constant, *k* is the wavenumber, *r* the cone location, and $\phi(t)$ represents a random phase term assigned to each simulated cone photoreceptor, to account for variable optical path lengths of the photoreceptor caused by variable outer segment lengths, or active metabolic processes resulting in phase differences between cones. The time dependence on the phase term could be fast changes caused by bleaching and recovery, or slow changes caused by shedding and regeneration of outer segments (Jonnal et al., 2007, 2010). In the case of a coherent system where all points can interfere with each other, the intensity function includes phase terms due to constructive and destructive interference:

$$I \propto c\left(\begin{array}{l} |E_1|^2 + |E_2|^2 + |E_3|^2 + |E_4|^2 + \\ \mathrm{Re}\left\{\begin{array}{l} \vec{E}_1\vec{E}_2^* \exp[i2\pi(\phi_1-\phi_2)] + \vec{E}_1\vec{E}_3^* \exp[i2\pi(\phi_1-\phi_3)] + \\ \vec{E}_1\vec{E}_4^* \exp[i2\pi(\phi_1-\phi_4)] + \vec{E}_2\vec{E}_1^* \exp[i2\pi(\phi_2-\phi_1)] + \\ \vec{E}_2\vec{E}_3^* \exp[i2\pi(\phi_2-\phi_3)] + \vec{E}_2\vec{E}_4^* \exp[i2\pi(\phi_2-\phi_4)] + \\ \vec{E}_3\vec{E}_1^* \exp[i2\pi(\phi_3-\phi_1)] + \vec{E}_3\vec{E}_2^* \exp[i2\pi(\phi_3-\phi_2)] + \\ \vec{E}_3\vec{E}_4^* \exp[i2\pi(\phi_3-\phi_4)] + \vec{E}_4\vec{E}_1^* \exp[i2\pi(\phi_4-\phi_1)] + \\ \vec{E}_4\vec{E}_2^* \exp[i2\pi(\phi_4-\phi_2)] + \vec{E}_4\vec{E}_3^* \exp[i2\pi(\phi_4-\phi_3)] \end{array}\right\} \end{array}\right)\left(\frac{2J_1(kr_j)}{kr_j}\right)^2 . \qquad \text{Equation 5}$$

For a purely incoherent system, no interference is observed, resulting in the intensity function:

$$I \propto c\left(\left|E_1\right|^2+\left|E_2\right|^2+\left|E_3\right|^2+\left|E_4\right|^2\right)\left(\frac{2J_1(kr_j)}{kr_j}\right)^2. \qquad \text{Equation 6}$$

Finally, in the case for our AOSLO system, for which the distance *d* between the layers of reflection is longer than the coherence length of the laser, Equation 5 reduces to include only the terms that can interfere:

$$\begin{aligned} I &\propto c\left(\begin{array}{l}\left|E_1\right|^2+\left|E_2\right|^2+\left|E_3\right|^2+\left|E_4\right|^2+ \\ \mathrm{Re}\left\{\begin{array}{l}\vec{E}_1\vec{E}_2^{*}\exp[i2\pi(\phi_1-\phi_2)]+\vec{E}_3\vec{E}_4^{*}\exp[i2\pi(\phi_3-\phi_4)]+ \\ \vec{E}_2\vec{E}_1^{*}\exp[i2\pi(\phi_2-\phi_1)]+\vec{E}_4\vec{E}_3^{*}\exp[i2\pi(\phi_4-\phi_3)]\end{array}\right\}\end{array}\right)\left(\frac{2J_1(kr_j)}{kr_j}\right)^2 \qquad \text{Equation 7} \\ &\propto c\left(\begin{array}{l}\left|E_1\right|^2+\left|E_2\right|^2+\left|E_3\right|^2+\left|E_4\right|^2+ \\ \left|E_1E_2\right|^2\cos[2\pi(\phi_1-\phi_2)]+\left|E_3E_4\right|^2\cos[2\pi(\phi_3-\phi_4)]\end{array}\right)\left(\frac{2J_1(kr_j)}{kr_j}\right)^2. \end{aligned}$$

Equation 6 and Equation 7 show that the use of a low-coherence SLD or other wide bandwidth source can effectively eliminate or reduce interference artifacts. This is indeed the case, as flood illuminated AO-ophthalmoscopes with temporally and spatially incoherent light show no apparent coherence artifacts and AOSLOs equipped with broadband sources have been shown to produce images with fewer interference artifacts (Grieve et al., 2006; Roorda & Zhang, 2005; Zhang et al., 2006b). But spatial coherence remains an issue for AOSLO imaging of densely packed foveal cones due to lateral optical interactions between them.

Defining the Foveal Cone Mosaic

A set of coordinates of individual foveolar cones obtained offline from human cone images was used as the input object for the model. The intensity at each cone was initially set to be inversely proportional to cone density such that it was uniform across the image (Li & Roorda, 2007).

Incoherent mosaics were generated by assigning an intensity value to each cone that was the sum of the two sources of reflections with relative intensities between the sources as specified by Equation 3. We intentionally ignored individual variations in cone intensity in an effort to isolate the impact of the diminished contribution of the IS/OS junction at the foveal center.

For coherent imaging, we assigned intensities to the two respective sources separately in same manner as above and additionally assigned random phase terms to the two sources within each cone.

For the AOSLO image we treated the two sources within each cone as mutually incoherent, owing to the short coherence length of the SLD source. As such, the image was effectively

formed by the sum of two independently generated coherent images, each with different initial phase terms, initiating from the two sources of reflection.

Image formation in the model

The point spread function (PSF) of the imaging system was considered to be diffraction-limited with appropriate settings for the pupil size and imaging wavelength used in our system. Because of the confocal pinhole, the PSF for incoherent imaging becomes the square of an actual Airy disk (Wilson & Sheppard, 1984). The illumination PSF was assumed to be the same as the imaging PSF as is typical for AOSLOs. For coherent imaging, the amplitude PSF was used for both the illumination and imaging paths. Incoherent images were generated in the classic way, by convolving the object with an intensity PSF.

Similar to the process by which they are formed in an actual AOSLO, the simulated coherent and AOSLO images were defined point by point using custom software developed in MatLab (The Mathworks, Natick, MA). First, initial intensity and phase values were assigned to each cone in accordance to the process outlined above. Then, an illumination PSF was centered at a specific location on the model retina and was used to weight its intensity. A secondary image of the illuminated model retina was generated at the confocal pinhole plane by convolving the object with the imaging PSF. The intensity of this secondary image was computed and then integrated over the open aperture of the confocal pinhole which, in a properly aligned system corresponds to the same location as the illuminated point. A single intensity value was determined in this manner and was repeated for a grid of illumination locations across the model retina. In this simulation, the confocal pinhole was considered to be an infinitely small aperture but the result will be similar for finite pinholes.

To offer some intuition about how interference arises in the scanning imaging process, consider the following situation where the AOSLO beam is scanning over two adjacent cones in the foveal center. The PSF is small enough to resolve the cones, but still large enough to illuminate two adjacent cones simultaneously (as illustrated in Fig. 4). Now consider the case where the scanning beam is midway between the two cones. With incoherent light, the PSF is just small enough to record a slight drop in reflected intensity at that location compared to when it was centered over one cone, and the cones are thus resolved. Now consider the coherent case: When the light from the two cones are in phase, light from the two adjacent cones will constructively interfere and will be observed as a maximum in reflectance at that scan location. Conversely, when the light from the two cones are 180° out of phase there is destructive interference and a minimum in intensity is recorded. In the actual situation, the phase difference of the light emerging from adjacent cones is random, and generates a type of speckle pattern whose maximum spatial frequency corresponds to the cone mosaic (provided that the incoherent resolution is better than the cone mosaic).

Adding Multiple Coherent or AOSLO Images

Since no noise was modeled, there is no benefit gained by adding multiple incoherent images. When adding multiple AOSLO or coherently imaged frames, we generated independent images

as specified above, each with a new set of randomly assigned phase terms for each cone and added them in intensity. This was done to account for changes in optical path lengths, either by varying OS lengths, slight changes in the sources of reflection within the cone, or changes in refractive index within the cones. As such, the benefits shown by adding multiple frames are only realized when such changes have occurred. When random phase changes do occur, then the sum of multiple coherent and/or AOSLO images is expected to yield an image that is identical to the incoherent image.

RESULTS

Typical imaging parameters were used to compute simulated images of the foveal cone mosaic with a wavelength of 840 nm and a 6 mm pupil, which corresponds to a full width at half maximum (FWHM) of approximately 0.6 arcmin. It is important to note that with a typical residual RMS wavefront error, we would expect this to increase according to previous studies (Zhang & Roorda, 2006). Figure 8 (a) shows an incoherent image, Figure 8 (b) shows a coherent AOSLO image with one layer of interference, and Figure 8 (c) shows a partially-coherent AOSLO image with two separate layers with independent interference artifacts and weighting summed to form the overall adjusted coherent AOSLO image.

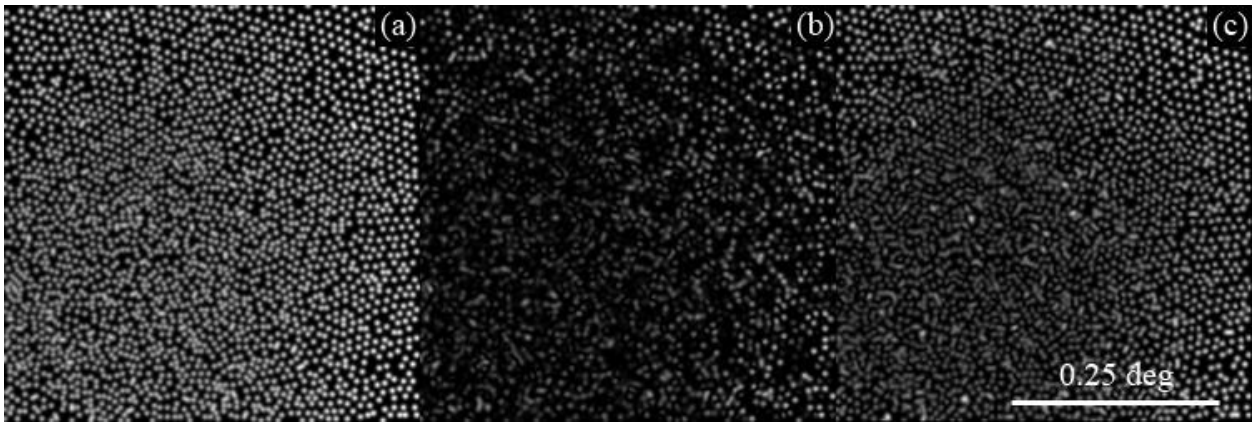

Figure 8: Model foveal cone mosaics using 840 nm light and a 6 mm pupil. Model foveal cone mosaics using 840 nm light and a 6 mm pupil. (a) Incoherent image (b) Coherent AOSLO image which allows for interference to occur between the two scattering sources within each cone, and (c) Low-coherence AOSLO image which does not allow for interference between the two scattering sources within each cone.

The highest density foveal cones are difficult to see in all the images, but particularly in Figure 8 (b) and (c) where interference artifacts completely contaminate their visibility. With coherent light, interference occurs between the two sources within the cone, causing random brightness variations across the entire mosaic. The immediate benefit of eliminating the interference between the two sources within a cone is apparent in Figure 8 (c), for which the intensity of the cone reflectivity remains much more uniform. But, at the foveal center, the lateral interference between neighboring cones dominates and the interference appears more similar between Figure 8 (b) and (c).

Figure 9 compares actual images of the same cone mosaic taken with coherent (660 nm laser diode) and low-coherence (680 nm superluminescent diode) light from a living eye. As expected, the mosaic has a much more uniform reflectance in the low-coherence case and a more contiguous cone mosaic is resolved.

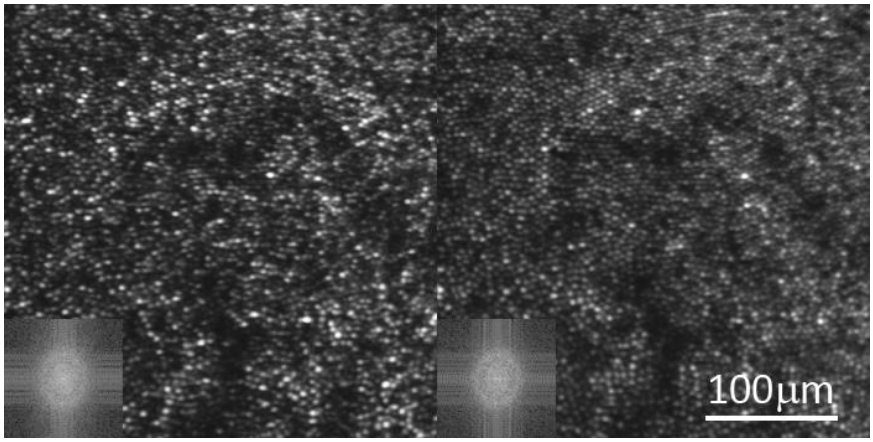

Figure 9: Comparison of imaging with coherent and low coherent light. Both images are of the same photoreceptor mosaic in a healthy normal eye. Both images are a registered sum of 100 frames from a single video. Variations in phase were not expected to have occurred over the course of one video and the addition of multiple frames is used here to increase the SNR of the image. The left image is taken with coherent 660 nm light and the right is taken with low coherent 680 nm light. The cone reflectance in the right image is much less variable, and the image reveals more of the contiguous close-packed cone photoreceptor array. The FFT of the image (lower left inset) reveals a better defined ring corresponding to the periodic cone array for the low-coherent image.

Figure 10 shows the benefit of adding multiple frames with independent phase relationships for coherent AOSLO images, where Figure 10 (a) is a single coherent image, Figure 10 (b) is the sum of 100 coherent images, and Figure 10 (c) is the incoherent image for comparison. As per the model, each image is generated with a unique set of random phase assignments to each cone. In both the coherent and the partially-coherent AOSLO cases, the addition of multiple frames reduces the interference artifacts, resulting in a higher fidelity image of the cone mosaic. The low coherence of the light source in the partially-coherent AOSLO image leads to faster convergence toward an incoherent image compared to the purely coherent case.

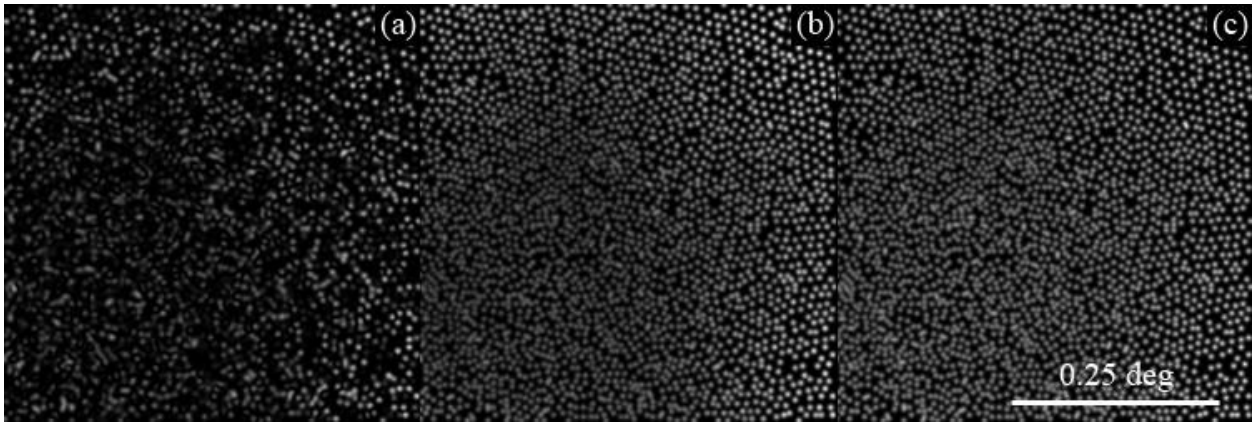

Figure 10: Summing multiple coherent (or AOSLO) images approaches the incoherent image. (a) Single coherent image (b) Sum of 100 coherent images (c) Incoherent image.

As expected, summing many coherent images results in an effectively incoherent image, provided that random phase changes occur between cones in the mosaic. In order to further illustrate the difference between the incoherent image and sums of coherent images for the model, a simplified retinal mosaic was used comprised of a small field with only 2, 3, or 4 cones. Figure 11 illustrates the convergence of the sums of these simplified coherent images onto the incoherent image with Figure 11 (a) plotting the log of the difference between the maximum intensity in the images for the sum images and a single incoherent image and Figure 11 (b) plotting the log of the difference between the mean intensities. All cases approach zero difference with the sum of multiple coherent images, more slowly with more cones in the image.

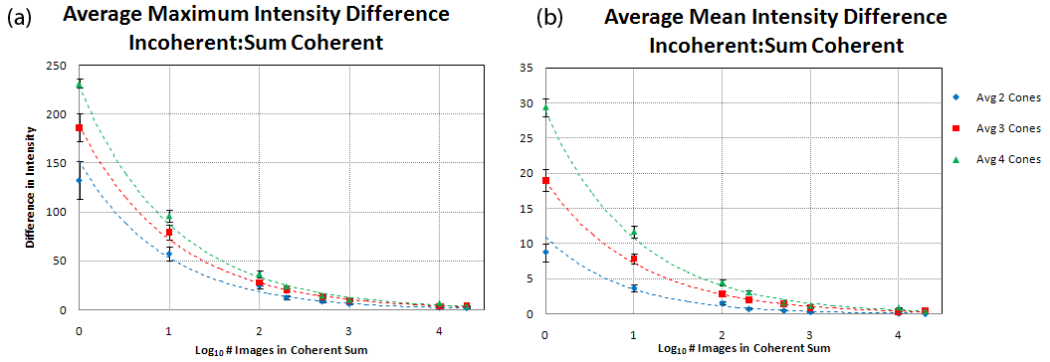

Figure 11: Plots illustrating the differences between the sum of coherent images and an incoherent image. Plots illustrate the maximum (a) and mean (b) intensities of difference images between sums of independent coherent images and the corresponding incoherent image, where all images have a normalized maximum intensity of 255. For images containing 2, 3, and 4 cones, the sum of independent coherent images approaches the incoherent image and images with more cones require the addition of more images.

DISCUSSION

Simulated images from the model are qualitatively similar to actual AOSLO images of the foveal cone mosaic. Figure 12 shows a typical image of the foveal cone mosaic taken from a healthy normal retina. The retinal topography is rarely flat and the layer of interest is not necessarily the layer that the wavefront sensor drives the correction toward. To account for that, we programmed the deformable mirror to apply precise focal adjustments during closed-loop. For all images like that shown in Figure 12, the focus is adjusted to obtain the sharpest and brightest cone images. Despite focal adjustments with steps as small as 0.05 D, we still do not routinely resolve cones in the foveal center. In both simulated and actual images, there is no clear and unambiguous mosaic of cones in the foveal center, but neither image is of low contrast either. Rather, the foveal center has a high contrast speckle-like pattern. These images support the idea that the presence of interference artifacts in AOSLO images is the primary reason it fails to reliably produce images of the foveal cone mosaic. While the use of a low coherent laser in the AOSLO offered major improvements, it was not sufficient to mitigate interference artifacts in images of the highest density cones.

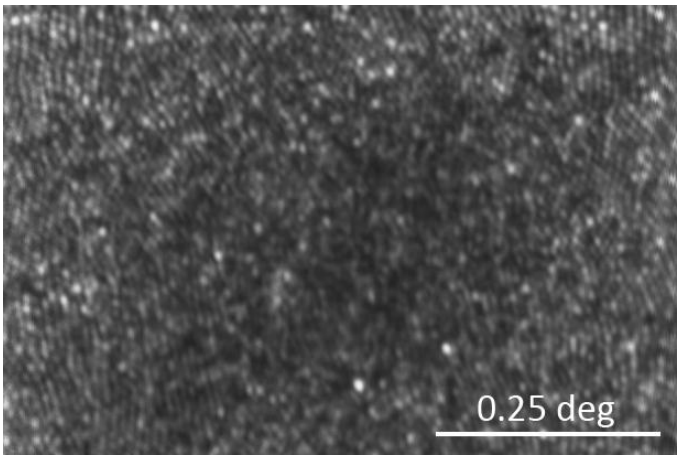

Figure 12: AOSLO image of the foveal center of a healthy normal eye taken with broadband 840 nm light. The image is a sum of 279 frames from an individual video where variations in phase are not expected to occur, similar to the images in Fig. 6. A contiguous, close-packed mosaic is visible at the margins of the image but at the foveal center, the mosaic of cones is less clear. Despite the fact that cones are not resolved, the image still has high contrast, exhibiting a speckle-like appearance.

A straightforward and obvious approach to reliably image the foveal cone mosaic is to minimize lateral interference between cones. This can be achieved by using larger pupil sizes and shorter-wavelength broadband light sources along with improved control of the AO system. But in a single frame, or even with a registered sum of multiple frames taken under the same optical conditions, lateral interference is still inevitable, given the practical limits on pupil size and wavelength available in a human eye. Further mitigation of the remaining interference artifacts can be achieved only by generating different phase relationships between the cones and

summing frames acquired under those conditions. By averaging images with different interference patterns the net image would approach an incoherent image, as demonstrated by Figure 10 and Figure 11.

To generate images of the same mosaic with different interference patterns we can image the same mosaic at different times, where the time delay between images is large compared to the underlying metabolic processes that cause phase differences within the cones. Over time, it is reasonable to expect that the relative optical path lengths between adjacent cones will vary randomly by ¼ wave or more, an amount that is sufficient to generate a unique interference pattern. We can also average images taken with different wavelengths. Interference artifacts will become less correlated as the wavelength separation increases. Finally, the average of a sequence of images taken over a time course where the optical path lengths of cones are intentionally changed is a promising approach and would be the most efficient. Miller's lab at Indiana University has shown that with visible light stimulation the optical path length of the cone photoreceptors does change quickly (Jonnal et al., 2007). If we image the foveal cones with IR light and stimulate the cones with red light, then the average of the sequence of frames during which the red light is activating the cones, should yield an image that is effectively incoherent. The dual wavelength imaging techniques along with precise stimulation in our AOSLO systems will facilitate these experiments (Grieve et al., 2006).

The model assumes that all cones reflect equally in space and over time. In fact, the reflectivity of cones is known to vary over time, even in the absence of interference artifacts. Pallikaris *et al.* used a flood-illuminated AO ophthalmoscope with a spatially and temporally incoherent Krypton flashlamp illumination source to measure the reflectivity of a human cone mosaic approximately every hour over a span of 24 hours (Pallikaris et al., 2003). The images revealed significant changes in cone reflectivity to the extent that, after six hours, cone intensity became uncorrelated with baseline. They also determined that the source of the variability originated primarily from the posterior termination of the cone outer segment. The implications of the latter results are that cones in the foveal center, which have a relatively weak reflection from their IS/OS junction, ought to experience larger relative changes in reflectance than more peripheral cones that have a stable and significant IS/OS component. In our (unreported) observations of incoherent cone images, it appears that the variability of cone-to-cone brightness is in fact greater at the foveal center than elsewhere in the mosaic. The presence of these variations is one more reason why adding images taken over time might help in resolving the entire foveal cone mosaic.

The model in this paper is specific for simulating images of the cone mosaic. How the coherence of light will affect other structures is not modeled, but is worth consideration here. Whenever an object being imaged consists of randomly arranged scatterers throughout its volume, then speckle in AOSLO images is inevitable. This applies to almost every other retinal structure including the retinal pigment epithelial cells, blood cells, ganglion cells and their axons which comprise the nerve fiber layer. To illustrate this point, Figure 13 shows an image of a model eye taken with coherent and low coherent light. In the model eye, the optic is a 100 mm focal

length achromat and the 'retina' is a simple sheet of clear white paper mounted at the lens focal point. Both images are nearly identical, and comprise very high contrast features which are evidence of interference artifacts. As expected, scattering structures in the paper fall within the coherence length of both light sources and the image taken with low coherent light only shows a slight reduction in speckle contrast.

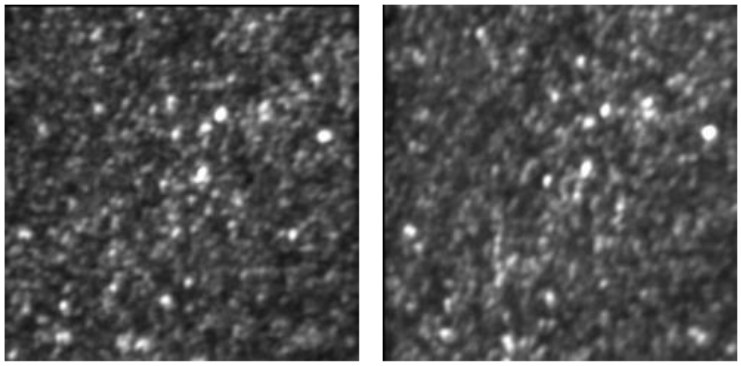

Figure 13: Registered sums of 150 frames from an AOSLO video of a model eye with a paper retina. The left image is taken with a coherent laser diode (660 nm) and the right image is with a low-coherent superluminescent diode (680 nm). In both cases, there are high contrast interference artifacts in the image, with only a slight reduction in its contrast from the SLD.

Finally, other practical considerations need to be taken into account in the effort to resolve foveal cones and are described briefly here:

Temporal Frequencies: Owing to the scanning nature of the image, the AOSLO image is generated by decoding a temporally modulated signal. Cones in the foveal center have the highest density and therefore generate the highest temporal frequencies - upwards of 5MHz - depending on the actual scan frequency and image field size. The temporal response of the entire electronics train needs to pass this signal.

Correcting for Eye Motion: Ever-present eye motions generate unique distortions in each AOSLO frame. Correction for these requires intra-frame removal of the distortions, and needs to be done with sufficient accuracy so that registered sums of frames from one or more videos will not reduce the contrast of the details in the image. This is especially important for features near the resolution limit. Our corrections are done with custom developed software (Stevenson & Roorda, 2005; Vogel et al., 2006).

Pixel Sampling and Scanner Nonlinearities: Most AOSLO systems use resonant scanners for the fast scanning axis in order to achieve high frame rates with sufficient sampling within each frame. A downside of the resonant scanners is that they scan in a sinusoidal fashion and therefore do not sample the scanned field with the same frequency throughout. With a fixed frequency pixel clock, the center of the field for which the scanner is moving fastest, is sampled

less frequently then the edges. The design of the AOSLO needs to be set so that the sampling frequency at the center of the field is sufficient for foveal cones.

Focus Adjustment: While the depth of focus is typically around 60 microns for AOSLO imaging, precise focus adjustments can be made in steps of 0.05D, which correspond to approximately 20 microns in depth at the retina. When imaging the foveola, the defocus is adjusted to optimize the visibility of the smallest cones. This focus will be slightly different than what is required to provide the best focus of neighboring cones since the ELM tends to be slightly elevated at the foveola. The elevation is approximately 25 microns, which corresponds to a defocus shift of ~ 0.06D (Hermann et al., 2005). As a result it is important to consider the defocus position carefully and make adjustments to optimize the visibility of the smallest cones, especially when imaging the foveal region.

Anisoplanatism: It is possible that topography of the inner retina at the foveal pit could introduce anisoplanatism across the AOSLO field. If this was the case, then the average wavefront across the field, which is what the AO system in a typical AOSLO uses to correct the wavefront, would be compromised everywhere and may limit the quality of the optical correction. The refraction of light along the slope of the pit is about 1 degree (Williams, 1980). Owing to the narrowness of the scanning beam at the retinal surface, we expect that any aberrations introduced due to anisoplanatism will have a negligible effect on the overall aberrations observed. Other studies have shown that the isoplanatic patch size at the fovea is 0.81 degrees on average (Bedggood, Daaboul, Ashman, Smith, & Metha, 2008), which is the field size we use for foveal imaging.

CONCLUSIONS

Developing a better understanding of the limits of AOSLO systems that use low-coherence light sources is an essential step on the path toward recording the highest fidelity images of the retina. This paper carefully models the process of AOSLO imaging of foveal cones, taking into account the nature of the light source as well as the unique structure of the cones and the way they pack into a mosaic, particularly cones in the foveal center. Our simulations compare well with actual images recorded in our system, lending support to the notion that interference artifacts impose limits on our ability to resolve cones in the foveal center. The model has also led to new ideas on potential ways to overcome these limits.

ACKNOWLEDGEMENTS

This section has been adapted from a previously published manuscript titled “Modeling the foveal cone mosaic imaged with adaptive optics scanning laser ophthalmoscopy” in Optics Express © 2010 Optical Society of America. Permission was obtained to include the adaptation in this dissertation from co-authors Daniel X. Hammer, Yuhua Zhang, David Merino, and Austin Roorda.

CHAPTER 3: COMPARISON OF ANATOMICAL AND FUNCTIONAL MEASURES OF THE NORMAL HUMAN FOVEA USING ADAPTIVE OPTICS SCANNING LASER OPHTHALMOSCOPY

ABSTRACT

In order to characterize the normal human fovea on a microscopic scale, it is important to obtain both structural and functional measures. We use Adaptive Optics Scanning Laser Ophthalmoscopy (AOSLO) to visualize most of the foveal cones in both eyes of three subjects. We identify cone locations and determine the location of peak cone density and compare it with the retinal locations targeted by steady fixation (the preferred retinal locus of fixation, PRL) and those that are responsible for the perception of direction of fixation (the preferred fixation direction, PFD). Repeated measures of the PRL show a large spread in the retinal locations targeted on individual fixation videos and that the mean location changed from day to day and was not co-located with the point of maximum cone density. The points recorded from an individual video had an average standard deviation of 2.6-4.9 arcmin (13.2-23.9 microns) and the average points had a standard deviation of 0.9-7.5 arcmin (4.3-36.9 microns). Individual measurements were displaced from each other by as much as 69.5 arcmin (343.73 microns) in the x (horizontal) direction and 28.1 arcmin (149.55 microns) in the y (vertical) direction. The mean locations had an average displacement of 2.4 arcmin (12 microns), ranging from 1.6-4 arcmin (8.1-21.4 microns). In addition, the PFD was also not co-located with the PRL or the point of maximum cone density and was approximately 3x larger than the spread of fixation points. In conclusion, on a microscopic scale, there are many slightly different definitions of the center of the fovea and these measures have different spreads and are only partially overlapping. It is valuable to combine different sources of information to form a more complete description of this important retinal region.

INTRODUCTION

The human foveola is the specialized region of the retina used for fixation and fine spatial vision tasks. The foveal center is characterized by anatomical features such as peak cone photoreceptor density, an absence of rod photoreceptors, the absence of retinal vasculature forming a foveal avascular zone (FAZ), and a displacement of inner retinal layers such that there is a distinctive pit, for which the fovea is named. The foveal center is identified in standard retinal fundus and optical coherence tomography (OCT) images as the area with maximum macular pigment, the center of the FAZ, the base of the foveal pit, or the location a prescribed distance from the optic disk (useful in particular when other measures of the fovea are obscured or confounded by disease progression). While these definitions result in similar locations that might suffice for larger views of the retina, when we zoom in on the very center of the fovea to obtain microscopic views of the foveal center, we would benefit from a more specific identification such as the region with peak cone density or minimum cone spacing (Chui, Zhong, Song, & Burns, 2012; Li et al., 2010; Putnam et al., 2005).

The addition of functional measures of the fovea to structural characterization can provide insight about the normal functioning fovea. AOSLO is one technology that can provide both microscopic structural information and functional testing by providing a high-resolution view of

most of the cone photoreceptors in the foveola as well as allowing a visible dynamic stimulus to be encoded directly in the imaging beam, resulting in a video of the underlying retina with stimulus locations unambiguously marked with respect to anatomical features. In order to fully understand functional markers of the fovea, it is important to consider the fact that the eye is always moving. Even when instructed to look directly at an object, the human eye is in constant motion under normal circumstances. These small fixational eye movements fall into separate categories depending on their duration and speed and result in a fundamental spread of the retinal locations used for fixation and result in the fact that measurements of the PRL and PFD cannot be made with a single snapshot. Historical studies of fixational eye movements were summarized by Ditchburn and Ginsborg and include slow drifts in fixation position (reported amplitudes between 1-6 arcmin with a duration less than 1 second in most studies), faster corrective movements called microsaccades (reported amplitudes vary, but range from 1-120 arcmin with a duration of ~25 ms), and a superimposed high frequency tremor component (reported amplitudes less than 1 arcmin at frequencies between 30-100 Hz in most studies) (Adler & Fliegelman, 1934; Ditchburn & Ginsborg, 1953; Martinez-Conde et al., 2004; Ratliff & Riggs, 1950). AOSLO imaging may be utilized to examine aspects of this dynamic fixation as images are acquired at video rates. These images may be stabilized using custom software (Arathorn et al., 2007; Stevenson & Roorda, 2005) resulting in an eye-trace and a video where retinal features are fixed in space. Due to image stabilization limitations governed in part by the small imaging field, displacement of stimuli due to drift movements is the main focus of our analysis. Drift movements occupy the bulk of the time we are able to analyze, changing the retinal location of stimuli during steady fixation. The larger and faster microsaccadic movements result in gaps in our stabilized videos that are discarded from analysis.

Previous investigations have localized the region of the foveola used for steady fixation tasks in relation to the underlying photoreceptor mosaic in a handful of subjects. Previous work using AO Ophthalmoscopy to study fixation stability in the foveal region reported that it averaged 3.4 arcmin (about 17 microns), in line with previous studies. They also determined that the region used for steady fixation is displaced from the location with the most densely packed cone photoreceptors by an average of 10 arcmin (about 50 microns) based on the mean from 3 subjects (Putnam et al., 2005). More recent studies using AOSLO found that the preferred retinal locus of fixation (PRL), the retinal locations targeted when the subject is instructed to fixate on a stimulus, had an average displacement of approximately 6 arc min (about 31 microns) for 14 subjects (Li et al., 2010).

AOSLO has also been used to measure the retinal locations targeted by other components of the fixational eye movement system (Kumar, 2008). In addition to confirming that the standard deviation of eye position during steady fixation varied from 4.6-7.8 arcmin for their subjects, Kumar investigated the retinal locations targeted by saccades and pursuit eye movements. The standard deviation of retinal locations targeted when the stimulus was jittered to one of 9 random locations, resulting in a saccadic eye movement, ranged from 8.0-17.1 arcmin. The standard deviation of retinal locations sampled when the stimulus moved in a 1.5 degree circle at 0.5 Hz, resulting in a pursuit eye movement, ranged from 5.9-13.4 arcmin. The distributions

of these three different eye movement systems were displaced from each other by a distance of 0.8-17.3 arcmin. Kumar reported that the mean fixation locus shifted between videos with a range of 5.6-10.6 arcmin for 4 different subjects with the explanation that it always remained within a larger region determining what was perceived as straight ahead (Kumar, 2008). Although they found displacements between the retinal locations targeted by the different systems, their relative placement with respect to the region with the highest cone density could not be determined due to resolution limitations.

In the current study, we further investigate these measures of the center of the fovea. In addition to high-resolution imaging, our characterization of the normal fovea includes two functional measures: the PRL and the perceived fixation direction (PFD), the retinal locations that give the perception of the fixation direction as identified with a psychophysical procedure. We examine the PRL in normal subjects on each of two days to identify the point or region around which the fixational system is centered and determine the stability of that point or region over time. We are specifically interested in the information that we can gain from an individual video, as that is what is traditionally acquired for all patients. We would like to understand how this measure of the PRL characterizes fixation over time for normal subjects, and how this characterization will extend to patients with abnormal fixation or retinal degenerations resulting in a non-foveal PRL.

METHODS

In order to study properties of the normal functioning fovea, AOSLO allows the direct correlation of stimuli with underlying retinal structure due to its ability to encode dynamic stimuli directly in the imaging beam. This provides simultaneous high-resolution views of the underlying photoreceptor mosaic with the stimulus locations encoded in the images during each frame of a video in real time. The result is that when the subject is instructed to look at an encoded stimulus, there is a direct measure of retinal locations corresponding to the subject's gaze direction.

The behavior of certain components of the small fixational eye movements have been shown to change with stimulus selection, the instructions given to the subject, or the subject's level of experience, but there was no significant difference observed in drift magnitudes, which are the component of particular interest in this study (Steinman, 1965). The stimuli used in this study were Gaussian dots with a FWHM of approximately 3.5 arcmin for determining the PRL and an approximately 6 arcmin solid square for determining the PFD. We chose the smallest Gaussian stimulus that was easily fixated to determine the PRL in order to make it as easy as possible for the subject to look at the center of the object. The larger, higher contrast stimulus was chosen for the PFD experiment in order to ease stimulus detection during the single frame presentation.

AOSLO Instrumentation: Two AOSLOs were used in this study and have been described previously (Merino, Duncan, Tiruveedhula, & Roorda, 2011; Zhang et al., 2006a). Both employed similar designs with a broadband superluminescent diode (SLD) centered at 840 nm

with bandwidth of approximately 50 nm coupled to a single-mode fiber (Broadlighter S840, Superlum, Russia), AO control with a Boston Micromachines MEMS mirror, and the use of AOMs for dynamic stimulus presentation. The system with the best resolution was used for anatomical imaging and the system with advanced stimulus control was used for psychophysics.

Subjects: Three healthy, normal subjects were recruited for this study and are summarized in Table 1. All subjects had best corrected acuities of 20/20 or better and were dilated for imaging. Informed consent was obtained from all subjects and the study protocol was approved by UC Berkeley and complied with the Declaration of Helsinki. Axial length measurements were made with the IOL-Master (Carl Zeiss Meditec, Dublin, CA) and a mean of 5 measurements for each subject was used. Retinal magnification differences induced by different axial lengths were factored in to linear reports of cone photoreceptor units as previously described (Li & Roorda, 2007).

Subject/Eye	DOB	Gender	Axial Length (mm)	Rx PRL	Rx PFD	Rx Anatomical
1 OD	1/12/1988	M	23.93	+0.5DS -0.75DCx135	+0.75DS -1.5DCx75	+0.75DS -0.75DCx130
1 OS			24.11	+0.75DCx45	-1.5DCx115	+0.5DS -0.75DCx45
2 OD	3/18/1981	F	24.58	-3DS	-3DS -0.75DCx110	-2.5DS
2 OS			24.54	-3.75DS	-3.75DS -0.5DCx90	-3.25DS
3 OD	5/17/1983	M	25.05	-1.5DCx20	-0.5DS -1DCx40	0.25DS -2DCx10
3 OS			25.85	-1.5DS -1.5DCx150	-2DS -1.5DCx130	-1.25DS -1.75DCx155

Table 1: Summary of Subject Information

Image Acquisition and Processing: The image acquisition process was slightly different depending on the system used and the imaging date, due to continual improvements that have been made to the AOSLO systems and processing over the course of this study (2010-2012). All AOSLO systems available were able to encode a dynamic stimulus directly into the imaging beam (Poonja et al., 2005; Rossi & Roorda, 2006; Rossi & Roorda, 2010a, 2010b; Rossi et al., 2007).

For the UCSF system: High-resolution images of the center of the fovea were obtained with this system, which had the best resolution of those available (Merino et al., 2011). Images were acquired over an approximately 0.7 degree field with a 6mm pupil. The field size was calibrated each day with a grating that was also used to de-warp images due to the sinusoidal scanner in post-processing. We used the Rochester desinusoid software that was developed by Alfredo Dubra with funding provided by the NIH grant BRP- EY014375 and NSF Science and Technology Center for Adaptive Optics, managed by UC Santa Cruz under cooperative agreement AST 98-

76783, and the Burroughs Welcome Fund. Images were then stabilized using custom MatLab software developed by Scott Stevenson. Frames that were not properly stabilized due to large eye movements or poor image quality were then removed from each video using custom MatLab software prior to forming a sum image, which increased the signal-to-noise ratio. These sum images were used to create a montage of the central fovea.

For the Berkeley system: Psychophysical experiments to determine functional measures of the center of the fovea were performed using this system due to its advanced stimulus delivery capabilities (Zhang et al., 2006a). The different experiments utilized different image dewarping and stabilization processes due to continual improvements that were made to the AOSLO over the course of the project. Images were again calibrated using a grid which was used to de-warp images due to the sinusoidal scanner in real-time using the image stabilization and targeted stimulus delivery interface described previously (Arathorn et al., 2007) for the videos used to determine the PRLs and in post-processing in the videos used to determine the PFD. For the PFD videos, the stabilization process was the same as the UCSF system, but the PRL videos were stabilized in real-time using the image stabilization and targeted stimulus delivery interface. In the event of poor stabilization due to large eye movements or poor image quality, the off-line stabilization process described could be completed on the raw videos. The same process was used to form sum images and these images were used to register the stimulus locations recorded in individual video frames to each other and to the high-resolution images acquired using the UCSF system. Custom MatLab software was used for this image registration and the image shifts were then double-checked manually by the authors.

Experiment 1: Determine the peak cone density in all eyes.

A high-resolution montage for each eye was assembled from the sum images acquired with the UCSF system and individual cones were labeled using a custom cone marking software (Li & Roorda, 2007). We were able to identify most of the cones throughout the central fovea with the number of cones identified per eye ranging from 18,311 to 29,142 and summarized in Table 2. Cone density was then determined at each cone using custom MatLab software as described previously in the literature (Li & Roorda, 2007). The peak densities measured in this way in each eye are also summarized in Table 2 and ranged from 98,185 cones/mm^2 to 141,300 cones/mm^2, in line with previous results (Curcio et al., 1990; Li et al., 2010; Østerburg, 1935). Iso-density curves were fit to this data with curves spaced by 5,000 cones/mm^2 after a Gaussian smoothing filter. This process is summarized in Figure 14. We successfully fit an estimate of the anatomical center of the fovea in all eyes from this data by taking the mean of the centroids of at least 3 iso-density curves, excluding contours that were not fit properly due to edge artifacts. Figure 26 in APPENDIX 1 illustrates the justification for this choice.

Subject/Eye	# Cones	Peak Density (cones/mm2)
1 OD	19134	139,550
1 OS	18330	141,300
2 OD	29142	126,260
2 OS	26601	140,370
3 OD	23629	125,740
3 OS	18311	98,185

Table 2: Summary of cones labeled and peak density for all eyes.

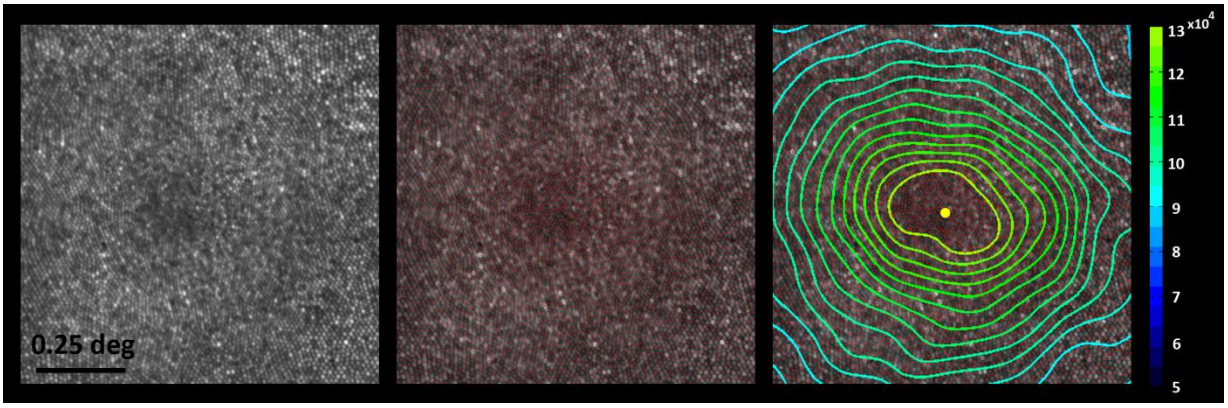

Figure 14: High resolution images were used to identify cone locations and fit iso-density curves to identify peak cone density. The center of the fovea was estimated from this data by taking the mean of the centroids of iso-density curves. Curves are spaced by 5000 cones/mm^2 after a Gaussian smoothing filter.

Experiment 2: Determine the retinal regions used for steady fixation, the PRL, and the mean of these locations in both eyes of three subjects on two different days.

One measure of the center of the fovea is the retinal locations used for steady fixation. Previous studies with non-image-based eye motion tracking have determined the standard deviation of fixation and other measures such as the Bivariate Contour Ellipse Area (BCEA) to represent the locus of fixation (Ditchburn, 1973; Steinman, 1965). These approaches are not able to make judgments about the precise targeted retinal locations used during steady fixation. With high-resolution imaging and the ability to determine stimulus position, previous studies showed similar measures of the standard deviation of fixation of 3.4 arcmin and determined a mean displacement of 10 arcmin or approximately 50 microns from the point of peak cone photoreceptor density for 3 subjects using a flood-illuminated AO ophthalmoscope (Putnam et al., 2005) and an average displacement of 6 arcmin for 14 subjects using an AOSLO (Li et al., 2010). By sampling dynamic fixation at video rates with stimuli encoded directly in the imaging beam, each AOSLO video can produce one measure of the PRL. The data from an individual video can be easily compared with previous studies on fixation stability using the non-image-based eye motion tracking that samples fixation over the course of a few seconds (Ditchburn, 1973; Steinman, 1965) while an individual sample or average PRL position is more

comparable with the individual measurements from the experiments with a flood-illuminated AO system (Putnam et al., 2005).

To determine the cones used for steady fixation, we recorded 10-15 second videos of a blinking stimulus, typically Gaussian dot with a FWHM of approximately 3.5 arcmin, in a 2.1 degree field with 840nm light. To better define the PRL and determine how its position varied across videos and time, we repeated measurements at two different time points in both eyes of three subjects. We analyzed at least 78 measurements each day with a minimum of 10 and average of 128 fixation points each to compare mean PRL across days. The average standard deviation of fixation from individual videos was 3.7 arcmin or 18.7 microns (range 2.6-4.9 arcmin/13.2-23.9 microns) in the x direction and 3.6 arcmin or 17.8 microns (range 2.8-4.6 arcmin/14.0-24.6 microns) in the y direction. More detailed summary information is shown below in Table 3. Stimulus locations were determined using custom MatLab software. Once these locations were recorded, the mean location and standard deviation were determined. This process is illustrated in Figure 15.

Subject /Eye	# Fixation Videos Day 1	# Fixation Videos Day 2	Average Points per video Day 1	Average Points per video Day 2	Average sd(x) Day 1	Average sd(x) Day 2	Average sd(y) Day 1	Average sd(y) Day 2
1 OS	93	92	131	180	3.0/ 14.7	3.3/ 16.1	4.1/ 20.0	3.3/ 15. 9
1 OD	98	97	191	191	3.8/ 18.3	3.6/ 17.4	3.4/ 16.5	3.8/ 18.2
2 OS	87	95	89	107	4.9/ 23.9	4.4/ 21.7	3.0/ 14.7	3.3/ 16.1
2 OD	81	91	120	120	4.4/ 21.8	4.3/ 21.0	3.4/ 17.0	2.8/ 14.0
3 OS	90	114	144	140	3.6/ 19.3	4.2/ 22.3	4.1/ 21.7	4.6/ 24.6
3 OD	78	82	69	50	2. 8/ 14.1	2.6/ 13.2	3.3/ 16.9	3.5/ 17.7

Table 3: Summary of individual PRL video analysis. The first two columns show the number of videos analyzed on each day. At least 10 points were registered in each video, with the average shown in columns 4 and 5. The average standard deviation values in columns 6-9 are the averages of the standard deviation values determined from the spread of fixation points in each individual video and are reported in arcmin/microns.

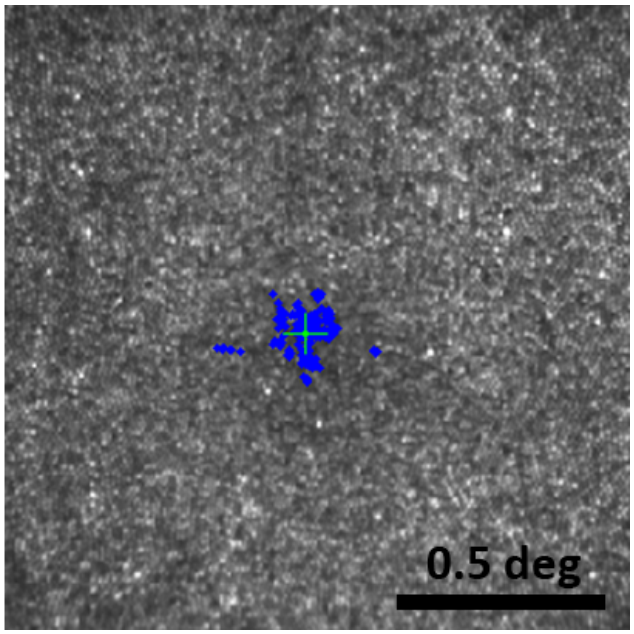

Figure 15: 208 fixation points recorded from an individual 15 second video plotted on the reference retinal image with the mean location +/- 1 standard deviation. The targeted retinal locations over the course of a 15 second video are plotted as blue dots. The standard deviations in the horizontal and vertical directions are represented by the cross and was 3.2 arcmin in the horizontal direction and 2.9 arcmin in the vertical direction. The maximum separation between points in the x direction was 23.1 arcmin and in the y direction was 12.9 arcmin.

Experiment 3: Determine the retinal regions responsible for the subjective perception of the direction of fixation, the PFD, in both eyes over time.

The perceived fixation is the zone on the retina onto which a stimulus must fall for a subject to respond that they are looking at it. The psychophysical procedure used to determine the PFD required the subject to look at the center of the 2.1 degree, 840nm imaging raster when they initiated a trial. During the trial, a 6 arcmin square was flashed for a single frame at a random location close to the fixation direction. Subjects made two 2 alternative forced choice (AFC) judgments of the direction of the stimulus with respect to their line of sight at the time of presentation (up/down, left/right). Subjects were instructed to ignore the edges of the imaging field and all other references and to make a judgment relative to their line of sight. 190-699 successful trials were obtained in each eye on two different days. Psychometric functions were constructed using this data and the point of subjective equality and standard deviation were determined as illustrated in Figure 15 for one subject on one day (Wichmann & Hill, 2001a, 2001b).

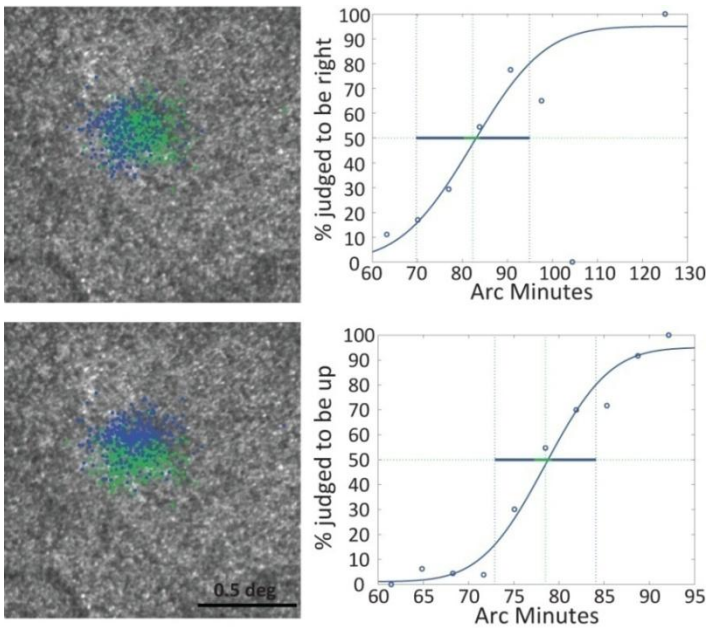

Figure 16: The data fitting procedure used to determine the PFD. For the left eye of subject 1 on the second day, the two retinal images show the locations where a stimulus fell color-coded for the subject's response left/right in the top figure and up/down in the bottom with the corresponding psychometric function fit showing +/- 1 standard deviation in blue and the confidence interval for fitting the threshold in green.

The data fitting procedure for all eyes on all days can be found in APPENDIX 2. In addition, Table 4 summarizes the data analyzed and resulting standard deviations for all eyes.

Subject/Eye	Points Day 1	Points Day 2	sd(x) Day 1	sd(y) Day 1	sd(x) Day 2	sd(y) Day 2
1 OD	553	579	27.9/135.7	9.3/45.2	11.3/55.0	5.9/28.4
1 OS	446	631	18.7/90.0	10. 7/51.3	20.1/96.5	8.4/40.3
2 OD	699	472	10.2/50.2	6.7/33.1	9.7/47.6	11.9/58.6
2 OS	190	493	28.1/139.1	8.4/41.4	11.5/56.7	6.1/30.2
3 OD	559	458	10.2/54.4	5.3/28.3	49.2/261.9	7.5/40.1
3 OS	541	378	9.4/47.6	9.6/48.7	8.7/44.2	4.9/24.7

Table 4: Summary of PFD fitting data. Sd values are in arcmin/microns.

RESULTS

Experiment 1: Determine the peak cone density in all eyes.

Peak density was determined in all eyes and is summarized in the methods section in Table 1. Contour plots labeling the anatomical center of the fovea for all eyes are shown below in Figure 17.

It is important to note that it was not possible to label all cones in the central 0.5 degrees for all eyes. This was the reason we needed to exclude the top 4 iso-density curves when determining the point reported as the peak as discussed in the methods section.

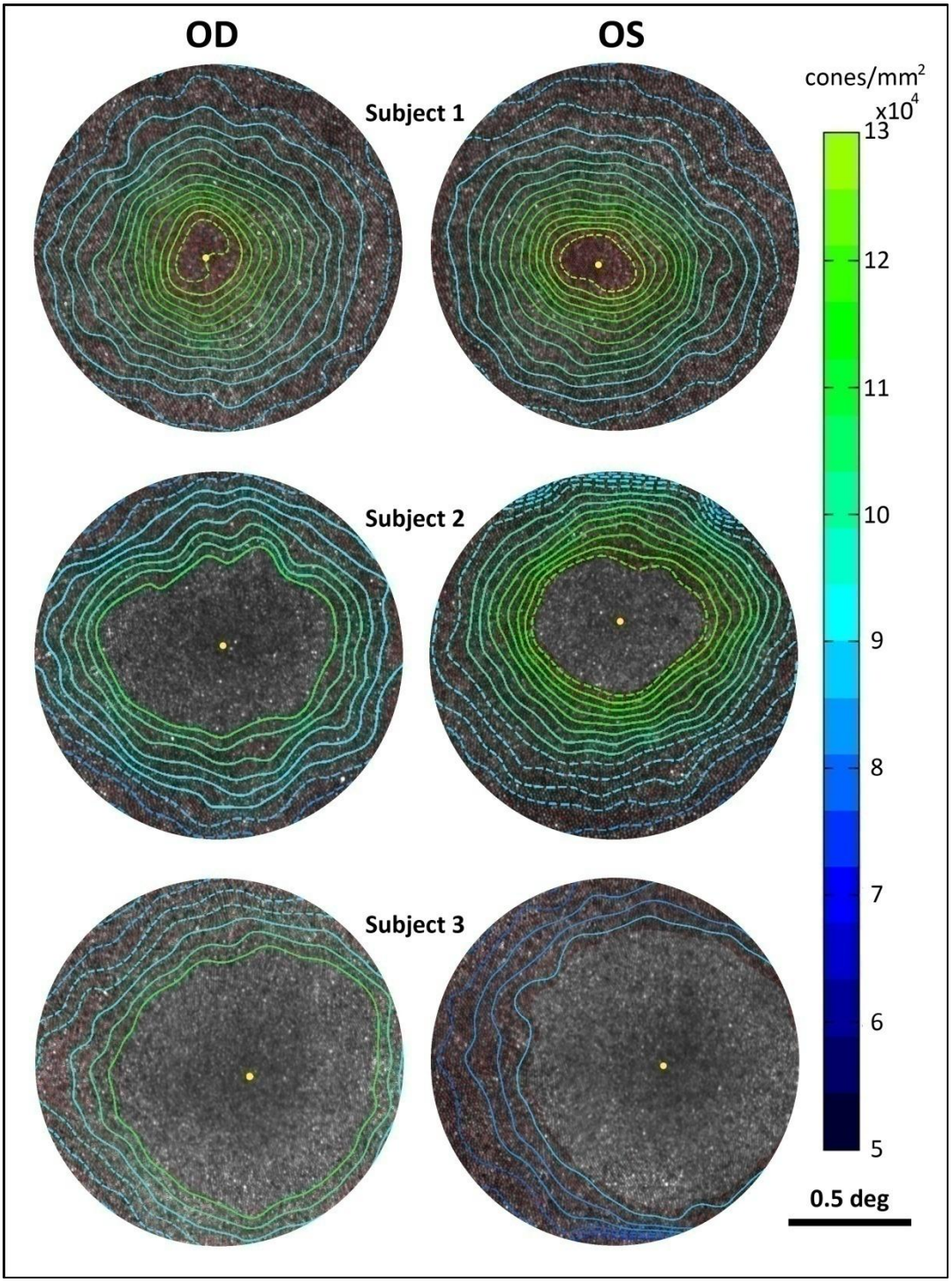

Figure 17: Contour plots for all eyes. The centroids of the solid contours were averaged to estimate the anatomical center of the fovea, labeled by the yellow dots.

Experiment 2: Determine the retinal regions used for steady fixation, the PRL, and the mean of these locations in both eyes of three subjects on two different days.

When many measurements of the PRL were taken across two days, the average standard deviation of the mean PRL locations was 2.5 arcmin (12.6 microns) in the x direction (range 0.9-7.5/4.3-36.9 microns) and 2.2 arcmin (11.1 microns) in the y direction (range 1.4-3.8/7.0-20.0 microns), which was expected from the literature (Ditchburn, 1973; Steinman, 1965). Individual measurements were displaced from each other by as much as 69.5 arcmin (343.7 microns) in the x direction and 28.1 arcmin (149.6 microns) in the y direction. The summary for all eyes is compiled below in Table 5.

Subject/Eye	sd mean(x) Day 1	sd mean(y) Day 1	sd mean(x) Day 2	sd mean(y) Day 2	Delta x max Day 1	Delta x max Day 2	Delta y max Day 1	Delta y max Day 2
1 OS	0.9/ 4.3	2.1/ 10.3	1.1/ 5.6	1.4/ 7.0	5.1/ 24.9	8.9/ 43.3	9.4/ 45.7	9.3/ 45.1
1 OD	1.6/ 7.5	1.9/ 9.0	1.1/ 5.3	2.3/ 10.9	11.9/5 7.4	6.4/ 31.0	11.7/ 56.3	12.6/ 60.4
2 OS	3.1/ 15.3	1.9/ 9.2	4.6/ 22.8	2.5/ 12.2	20.7/1 01.8	40.5/ 199.1	11.4/ 56.0	15.6/ 76.8
2 OD	3.0/ 15.1	2.9/ 14.1	7.5/ 36.9	2.1/ 10.6	17.7/8 7.3	69.5/ 343.7	21.4/ 106.0	18.5/ 91.4
3 OS	2.9/ 15.7	2.0/ 10.4	2.3/ 12.1	3.8/ 20.0	21.8/1 15.9	18.7/ 99.7	11.0/ 58.5	28.1/ 149.6
3 OD	1.1/ 5.4	1.9/ 9.7	1.1/ 5.6	2.0/ 10.0	4.8/ 24.3	5.9/ 29.9	11.2/ 56.9	9.4/ 48.0

Table 5: Summary of distribution of locations the individual PRLs. The standard deviations reported in the x and y directions were computed from the distributions of mean PRL locations on each day. Delta x max and Delta y max are the maximum separations between measurements of the mean PRL location from individual videos on each day. All values are in arcmin/microns.

To test for a shift in the mean of the two distributions of PRL measurements, we test along the X and Y directions independently with a Normal distribution test for the difference of two sample means. We assume that the distribution of the sample average is reasonably close to a Normal distribution because our sample size is large and the resulting distribution of the sample means is expected to be close to normal by the central limit theorem. We then test the two pairs of X-Y coordinates simultaneously using a parametric bootstrap simulation approach using Euclidean distance as a metric. Using this approach, we simulated a million bivariate normal random variables with a mean of zero and a covariance describing the expected spread of the data. For each simulated value, the distance from the origin was computed and the percentage of these simulated values that have a distance exceeding the distance of the observed mean difference is the p-value. As a result, the means were statistically different across days when considering the X-Y coordinates simultaneously for all eyes with an average

displacement of 2.4 arcmin (12 microns) with a range of 1.6-4.0 arcmin (8.1-21.4 microns). This data is summarized below in Table 6.

Subject/Eye	Separation between Daily Means (arcmin/microns)	p values when testing along the x direction	p values when testing along the y direction	p values when considering x-y coordinates simultaneously
1 OS	1.8/8.7	0	0.00000001	0
1 OD	2.1/10.1	0.17305295	0	0
2 OS	2.3/11.2	0.00741303	0.00000025	0.00015
2 OD	2.6/12.6	0.01079835	0.00052917	0.00313
3 OS	4.0/21.4	0.04924145	0	0
3 OD	1.6/8.1	0.00006731	0.000006	0

Table 6: Comparison of the mean locations determined from the distribution of multiple measurements of the PRL on two separate days. The separation is the radial separation between the mean locations without regard to whether it is horizontal or vertical. The p values when testing along the X and Y directions independently are reported as well as the p values when considering the X-Y coordinates simultaneously, indicating the level of statistical significance of the separation between distributions.

Experiment 3: Determine the retinal regions responsible for the subjective perception of the direction of fixation, the PFD, in both eyes over time.

The PFD formed a broad distribution with an overall mean of 12.9 arcmin (64.6 microns), a vertical mean of 7.9 arcmin (39.2 microns) with a range from 4.9-11.9 arcmin (24.7-58.6 microns), and a horizontal mean of 17.9 arcmin (89.9 microns) with a range from 8.7-49.2 arcmin (44.2-261.9 microns). The summary of this data was shown above in Table 4.

Combining all Measures: After determining the peak density, the PRLs, and the PFDs in all eyes, the next step is to combine all the data. The separations between the anatomical center of the fovea and the PRL and PFD were calculated. The average separation between the mean PRL location and the anatomical center was 8.9 arcmin (44.8 microns) with a range from 1.2-18.0 arcmin (6.2-95.5 microns) and the average separation between the point of subjective equality as measured by the PFD was separated from the anatomical center by an average of 8.9 arcmin (44.2 microns) with a range from 1.8-13.2 arcmin (9.4-67.1 microns). The separations between the various measurements are summarized below in Table 7. All measures are plotted together on the high-resolution images of the fovea in Figure 18.

Subject /Eye	Peak to PRL Day 1	Peak to PRL Day 2	Peak to PFD Day 1	Peak to PFD Day 2	Separation between PRLs	Separation between PFDs
1 OD	8.7/42.0	10.0/48.1	12.2/58.5	14.6/70.0	1.7/8.4	18.0/86.5
1 OS	8.0/39.2	10.1/49.2	10.7/52.1	13.6/65.9	2.3/11.3	2.9/13.9
2 OD	1.3/6.2	3.3/16.5	5.9/29.2	2.8/14.0	2.2/10.9	4.6/22.7
2 OS	3.0/14.5	4.4/21.5	9.1/44.9	6.7/33.0	2.5/12.3	2.4/11.9
3 OD	9.5/48.1	13.4/68.2	12.2/61.9	13.2/67.1	4.1/21.0	2.0/10.1
3 OS	16.6/88.4	18.0/95. 6	1.8/9.4	4.5/23.9	1.5/8.0	3.1/16.4

Table 7: Separation between measures of the center of the fovea. Here we report the distances between the point determined to be the anatomical center of the fovea (Peak) and the average of the PRL locations (columns 2 and 3) as well as the center of the distribution of points responsible for the perception of the direction of fixation (PFD) (columns 4 and 5). The distances between PRLs and PFDs are also reported (columns 6 and 7). All values are in arcmin/microns.

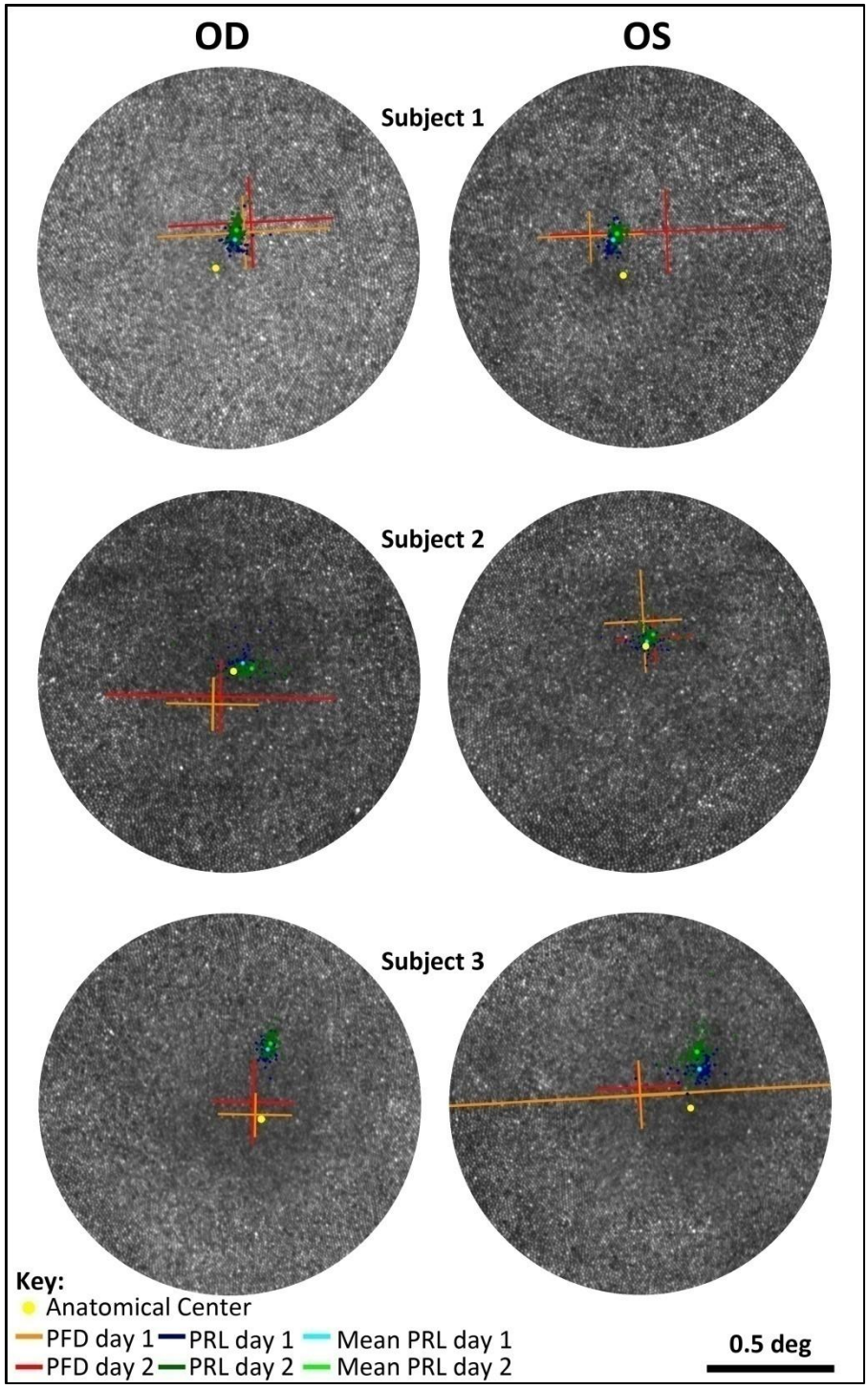

Figure 18: High resolution montages in fundus view for the three subjects. The bars represent +/- 1 standard deviation for the PFD, which can be interpreted the boundaries where the correct decision was made 84% of the time.

DISCUSSION

The retinal locations corresponding to the PRL are highly variable in both individual video frames and the mean locations derived from individual videos. In individual videos, the average standard deviation of fixation was 3.7 arcmin or 18.7 microns (range 2.6-4.9 arcmin/13.2-23.9 microns) in the x direction and 3.6 arcmin or 17.8 microns (range 2.8-4.6 arcmin/14.0-24.6 microns) in the y direction. Comparing the mean locations determined from individual videos showed an average standard deviation of 2.5 arcmin or 12.6 microns in the x direction (range 0.9-7.5 arcmin/4.3-36.9 microns) and 2.2 arcmin or 11.1 microns (range 1.4-3.8 arcmin/7-20 microns) in the y direction. As the mean locations are determined from individual videos, it is not too surprising that the standard deviation of the mean locations is smaller than that from an individual video on average.

Previous measurements of the standard deviation of fixation are more comparable with one of these measures or the other. For example, Putnam et al. measured the standard deviation from points corresponding to individual snapshots obtained using an AO Ophthalmoscope (Putnam et al., 2005). Even though these are individual measurements, the points are not at all correlated temporally with each other as they are in the case of an individual AOSLO video. As a result, these measurements should be more fairly compared with the measurements of the mean PRL locations. Historical studies of fixation stability used measurements from an eye trace, where points were correlated with each other and are more fairly compared with the data from an individual AOSLO video (Ditchburn, 1973; Steinman, 1965). An analysis of a subset of the data showed that the mean PRL locations could be fit by a Gaussian distribution with an R^2 of 0.94 while the data from individual videos had an R^2 value of 0.87. In either case with a fairly large sample size, it is possible to approximate the distributions as normal, but this is an additional justification for our use of the mean PRL locations in our analysis.

The mean PRL was displaced from the point of peak cone density by an average of 7.94 arcmin, which is also consistent with previous studies reporting a separation of 10 arcmin (Putnam et al., 2005) and 6 arcmin (Li et al., 2010). Previous studies hypothesized that the displacement of the PRL for steady fixation and loci of other fixational sub-systems places them at the edges of the blue cone-free zone or the region with highest cone density, compromising the maximum resolution so all systems maintain relatively high resolution. If one system was at the center, it would compromise the resolution of the others by up to a factor of 2. An alternative explanation might be that one system does not need the resolution of the other systems (for example, there was an exhibited lag in the pursuit eye movements or larger saccadic eye movements might not need the resolution of the steady fixation system). Rucci has also made arguments for why do we bother fixating at all when we have this whole fovea with the potential for exceptional acuity (Rucci, Iovin, Poletti, & Santini, 2007)? Although Rossi showed that acuity drops immediately away from the PRL, Boyce measured monocular fixational eye movements and found reasonable agreement between days in the same subjects. He also proposed the use of a series of overlapping short-period fixation areas summing to the overall elliptical fixation area (Boyce, 1967; Rossi & Roorda, 2010a). These studies are somewhat consistent with our measurements of the mean PRL locations shifting in one day and between

days. Boyce's analysis did not include high-resolution imaging however, so even though the stability and characteristic behavior of the eye movements did not change from day-to-day, measurements of the mean locations targeted were not available and it is not possible to know if there was a shift in the mean fixation locus. Glezer also proposed the possibility of an insensitive zone of approximately 5 arcmin in diameter in the center of the retina where all points would have the same high level of visual acuity (Glezer, 1965).

CONCLUSIONS

Peak cone density, PRL, and PFD do not converge on a single retinal location, suggesting that the developmental and functional systems that serve foveal vision operate somewhat independently. Since fixation stability is finer than our PFD it suggests that fixation is driven by a sub-perceptual mechanism. That is, we do not wait until we perceive our stimulus is falling off of our fovea to make a corrective eye motion. The fixated image just needs to fall within the PFD, not necessarily at the same location every time, for the fixation system to kick in.

Current clinical measures of the fovea are not sensitive enough to detect the changes that we see between these different definitions of the fovea. However, as high-resolution imaging is used more widely, it will become important to know how well the center of the fovea can be determined and how the functional and anatomical markers compare. Scientifically, it is interesting that there is no one location that defines the center. It is important that the mean location from the distribution of measured PRLs is not the same from day to day in all 3 subjects as this has implications for how well we can know where the functional center of the fovea is in diseased subjects where we cannot identify the anatomical center in any other way.

CHAPTER 4: THE ROLE OF NATURAL AND MANIPULATED FIXATIONAL EYE MOVEMENTS IN FOVEAL VISION

ABSTRACT

Despite retinal image motion caused by fixational jitter, the world appears stable. The use of Adaptive Optics Scanning Laser Ophthalmoscopy (AOSLO) with real-time image stabilization and targeted stimulus delivery capabilities enables us to investigate the role of small fixational eye movements, or the lack thereof, on visual tasks. The image stabilization and targeted stimulus delivery interface facilitates the presentation of any stimulus motion including natural, stabilized, amplified, rotated, or independent trajectories. Here we look specifically at the role of stimulus motion in the detection of motion, contrast sensitivity, and the role that motion plays in image fading. We find that the smallest motion detection thresholds occurred under natural eye motion conditions for both a slow (0.5 cps) and a fast (1.5 cps) circular motion trajectory with a radius of approximately 2.5 arcmin for the slow condition and approximately 0.8 arcmin for the fast condition. When the movement of the center of rotation of the stimulus was manipulated to be equal and opposite to the natural motion, thresholds were measured to be 2.1 and 2.5 times larger for the slow and fast conditions, respectively. When the stimulus traveled a perfect circular path in retinal coordinates by stabilizing the center of rotation of the stimulus, the thresholds were 1.4 and 1.6 times larger. In the final condition where the center of rotation of the retinal stimulus was doubled, thresholds were 1.3 and 1.5 times larger. We find that the time required for an image to fade was smallest under stabilized conditions and that there were no instances where the stimulus did not fade in the 9-second trials for three subjects. Under manipulated conditions where there was more motion added, the closer the condition became to the natural condition, the longer it took for the image to fade and the more instances where the stimulus would not fade during an entire 9-second trial. When measuring the contrast required to detect a stimulus that was ramping up in contrast from invisible to visible over the course of a 6 second trial, the highest contrast required for all subjects occurred under stabilized conditions. The lowest thresholds were measured under negative gain conditions, where the stimulus motion was amplified. These results support previous reports that the visual system perceives true motion of objects despite confounding motion of their retinal images.

INTRODUCTION

In general, normal human subjects experience a stable percept of stationary objects in the world despite the fact that images are in constant motion on the retina even during steady fixation. This constant fixational jitter is larger than detectable motion thresholds and greater than the size of foveal receptive fields (McKee, Welch, Taylor, & Bowne, 1990; Smith, 2001). There is still a great deal to be understood about the consequences of these movements in spatial vision tasks and there are two main categories of explanations for the role that fixational eye movements play in visual processing: one that they maintain retinal image contrast by preventing images from disappearing (Ditchburn & Ginsborg, 1952; Kotulak & Schor, 1985; Weymouth, Hines, Acres, Raaf, & Wheeler, 1928) and a second that the spread of fixational eye

movements is caused by instability in the system such that errors caused by drifts are corrected by microsaccades (Cornsweet, 1956).

IMAGE STABILIZATION AND STIMULUS CONTROL WITH AOSLO

In order to understand the role of natural and manipulated retinal image motion, we describe two experiments in this chapter. Many of the methods are common to both, so we provide these first.

AOSLO Instrumentation: The Berkeley AOSLO was used in this study and has been described previously (Zhang et al., 2006a). Imaging was performed with a broadband superluminescent diode (SLD) centered at 840 nm with bandwidth of approximately 50 nm coupled to a single-mode fiber (Broadlighter S840, Superlum, Russia), with stimulus presentation performed with a low-coherence 680nm SLD. AO correction was accomplished with a Boston Micromachines MEMS mirror and AOMs were employed for dynamic visible stimulus presentation directly encoded within the imaging beam (Poonja et al., 2005; Rossi & Roorda, 2006; Rossi & Roorda, 2010a, 2010b; Rossi et al., 2007). It was possible to use either or both a dark stimulus in the dim 840nm imaging field or a bright 680nm stimulus.

Image Acquisition and Dynamic Stimulus Presentation: Recent developments with collaborators at Montana State University allow real-time stabilization of stimuli with simultaneous high-resolution imaging using AOSLO (Arathorn et al., 2007; Yang et al., 2010). In addition to stimulus stabilization, it is also possible to speed up or slow down the motion of a stimulus with respect to the actual eye movements or to encode an independent and unrelated movement in order to characterize its effect on visual performance. As a result, the use of AOSLO with the image stabilization and targeted stimulus delivery interface allows us to present a stimulus within the imaging raster with any motion profile. The motion of the stimulus was controlled with a direction and magnitude that was a computed function of the eye's own motion. There are a number of conditions with respect to the natural eye motion that will be used in these experiments. Gain 0 refers to the natural condition. In this case, the stimulus does not move in space. As a result, the stimulus slips naturally across the photoreceptor mosaic when the eye moves. Gain 1 refers to the stabilized condition. In this case, the stimulus motion is equal to the retinal motion. As a result, there is no motion of the stimulus across the photoreceptor mosaic. Gain -1 refers to the condition where the retinal slip is doubled. In this case, the additional stimulus motion is equal and opposite of the retinal motion. As a result, there is double the motion across the photoreceptor mosaic. Finally, Gain 2 refers to the condition where the retinal motion is equal and opposite of the natural stimulus motion. In this case, the stimulus motion is double retinal motion. As a result, there is equal motion across the photoreceptor in the opposite direction compared with normal stimulus motion. These conditions are illustrated in Figure 19.

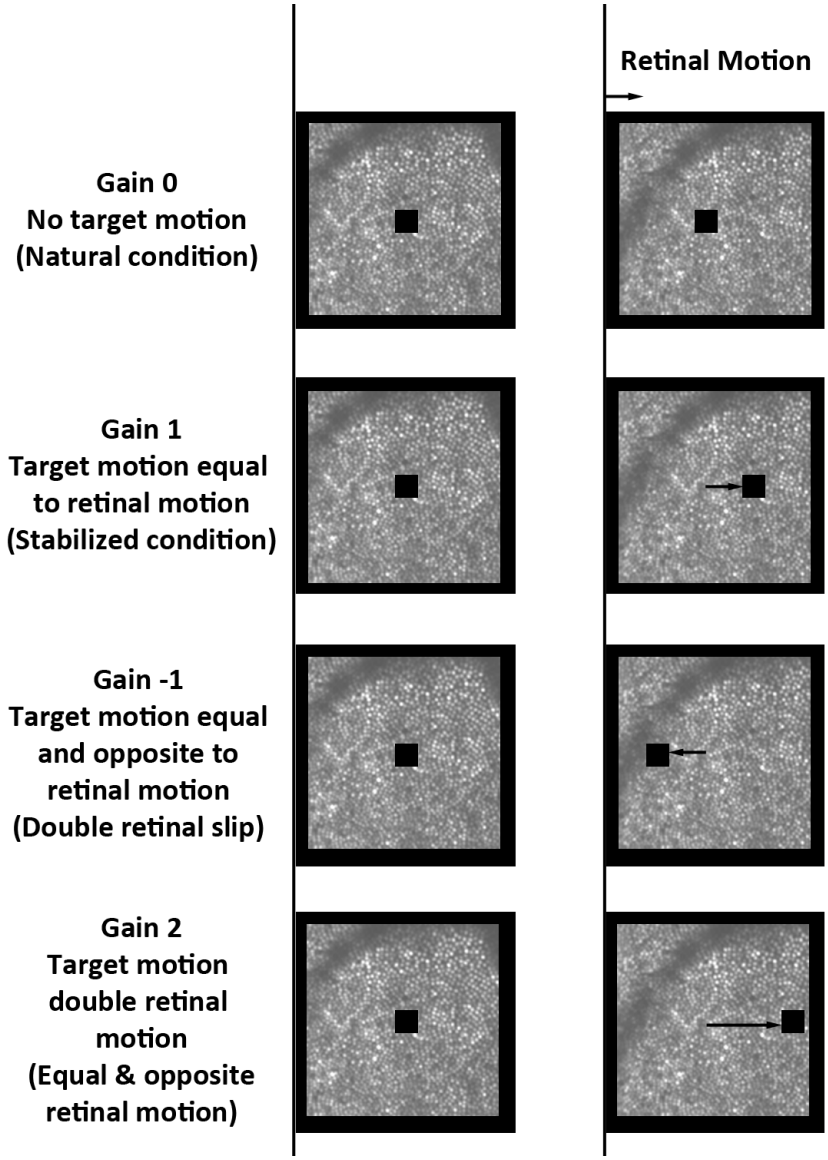

Figure 19: Illustration of stimulus motion conditions with respect to retinal image motion used in these experiments. Gain 0 is the natural stimulus motion condition. Gain 1 is the stabilized condition. Gain -1 is the condition where retinal slip is doubled. Gain 2 is the condition where stimulus motion is equal and opposite of natural stimulus motion.

A few things to note about these retinal image motion conditions. Gain 0 and gain 2 have equivalent retinal motion, but in opposite directions. Gain 1 and Gain -1 have equivalent relative motion with respect to the imaging raster.

In addition to these base motions that are related to the natural eye motion, additional stimulus offsets and/or motion paths may be superimposed on the stimulus motion. For

example, if we want to randomize the targeted location in order to minimize fatigue on a particular set of photoreceptors, we can set up a random variable to displace the stimulus presentation location from a selected location or if we want to present a stimulus moving in a predefined path such as the natural eye motion from a different trial, we could change the location on each subsequent frame of a video.

A. MEASUREMENT OF MOTION DETECTION THRESHOLDS

Fixational eye movements cause visual stimuli to move on the retina at all times. The magnitude of motion is large in many respects: it is greater than the size of foveal receptive fields and is easily large enough to see. Despite the retinal image motion caused by fixational jitter, objects in the world appear to be stable and without this motion, images fade from view. We set out to investigate the role of natural and manipulated fixational eye movements in foveal vision. Is our perception of motion best when the images of the world slip naturally across our retina due to eye motion?

When discussing motion judgments, it is important point out that thresholds for detecting relative motion and absolute motion are smaller than fixation motion and subjects' are extremely good at making relative judgments in comparison to absolute judgments of object motion. Relative motion thresholds on the order of seconds of arc have been measured (McKee et al., 1990), allowing subjects to discriminate stimulus motions smaller than the diameter of a foveal cone (Legge & Campbell, 1981; Nakayama & Tyler, 1981; Raghunandan et al., 2008). Previous work using AOSLO to study referenced and unreferenced motion made absolute motion threshold measurements of ~1 arcmin and demonstrated that there is only partial compensation for eye movements when making motion judgments in an unreferenced field as opposed to complete compensation for referenced motion (Raghunandan et al., 2008). As a result, Raghunandan suggests that a spatial reference is important for complete compensation of retinal jitter, arguing against an exclusive compensation based on an efference copy or muscle proprioception alone. They also note that it is possible that only certain types of eye movements, such as saccades, are compensated by the efference copy or muscle proprioception and a spatial reference is only necessary to compensate for other types of eye movements, but could not do more than speculate with their data set. The studies here all have a constant frame of reference from the AOSLO imaging raster, so it is not possible to address the source of eye motion information.

Previous experiments utilized real-time stabilization and targeted stimulus delivery with AOSLO to study the relationship of stimulus motion to perceived stimulus motion using a psychophysical matching task (Stevenson et al., 2010). The results indicated that that increasing the magnitude of retinal image motion in a direction consistent with natural eye motion, even if it is amplified, has little effect on the perceived image stability. In contrast, cancelling out the retinal image motion leads to a percept of image motion before the object fades away from view due to the lack of motion. Finally, presenting a magnitude of retinal image that is equal to that of the natural motion but in the opposite direction leads to the percept of a highly unstable object. It is clear from this that the direction of retinal image motion plays an

important role in producing a stable percept of the world. We are interested in quantifying the role that image stability has on image fading as well as the role of natural and manipulated movements on the detection of motion and contrast sensitivity.

There are a few potential sources of information that could be used to compensate for fixational eye movements. They include the use of an efference copy of the signal used to drive eye motion (Helmholtz, 1925; Poletti, Listorti, & Rucci, 2010), the use of the signals sent from the moving eye muscles to the brain (proprioception) (Bridgeman, 1995), and the use of a signal derived directly from the information in the retinal images (Gibson, 1954; Murakami & Cavanagh, 1998; Tulunay-Keesey & Verhoeve, 1987).

In either case, subjects have access to some information about the eye motion and compensate for it to give the stable percept of the world. This raises questions about how this information is used to suppress the motion signal from these fixational eye movements. It is possible that subjects are compensating for the actual retinal motion, that they are compensating for the magnitude of the eye motion, or that they are compensating for the direction of the eye motion. The consequence of employing these different mechanisms is that if subjects are only compensating for the actual retinal motion, all other directions of motion will lead to unstable percepts. If subjects compensate for the magnitude of retinal motion, any small motion of the same scale as fixational eye motion will be suppressed regardless of direction. Finally, if subjects compensate for the direction or retinal motion, all motion in a direction consistent with the direction of the retinal motion will be suppressed regardless of magnitude. Figure 20 illustrates these possible compensation schemes with respect to an illustration of eye motion.

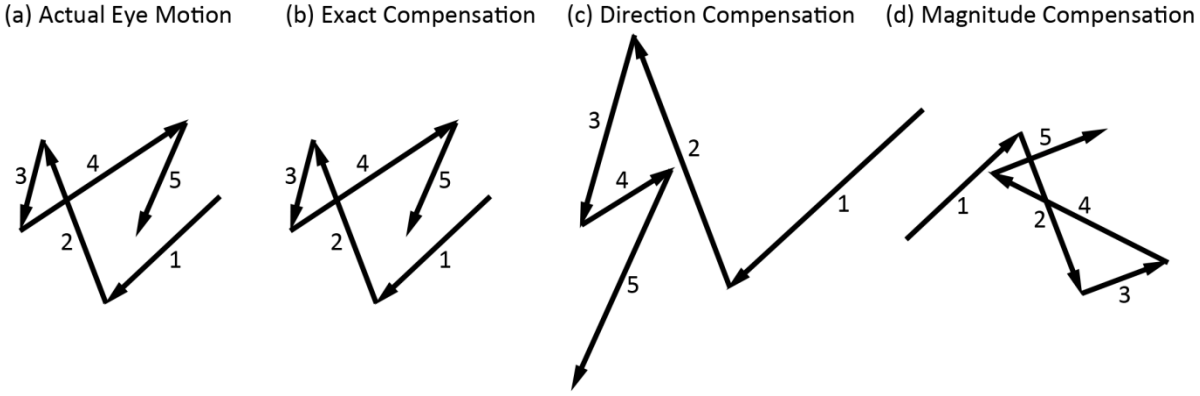

Figure 20: Possible eye motion compensation schemes. Simplified illustration of a possible eye motion path and possible compensation schemes. If (a) represents the actual eye motion, possible paths that could be compensated to produce stabilized percepts include (b) the exact eye motion path (c) paths that are consistent with the direction of motion, regardless of magnitude, and (c) paths that are consistent with the magnitude of motion, regardless of direction.

Once subjects possess this information, it may be used in a number of different ways in our motion detection tasks with a few possible results. The first hypothesis is an exact-compensation situation, where subjects compensate for the actual retinal motion. In this case, the information is used to exactly offset the image instability induced by eye-motion and the smallest thresholds would be measured only under natural conditions. The second hypothesis is a direction-driven compensation situation, where subjects compensate for motions consistent with the direction of retinal motion. In this case, stimuli that slip on the retina in a direction consistent with eye motion - even if they are amplified – would result in the smallest thresholds for motion-detection or lower than for other directions of motion. The third hypothesis is a magnitude-driven compensation situation, where subjects compensate for the magnitude of retinal motion regardless of direction. In this case, motion-detection thresholds would be lowest when the retinal motion is smallest.

In order to understand how our ability to detect very small amounts of stimulus motion relates to the spatial manipulation of the motion trajectory on the retina, we make quantitative measurements of motion detection thresholds. Five normal subjects performed a 2AFC task judging of clockwise or counterclockwise motion of a 26 pixel red (680nm) circular stimulus in a 512 pixel, 840nm imaging field that was approximately 1.2 degrees on a side. The circular stimulus trajectory was presented with the center of rotation of the retinal motion moving naturally with fixational eye movements as well as manipulated such that it was stabilized or amplified in directions consistent with and opposite natural eye motion. Stimuli were presented extrafoveally to avoid fixation tracking and two conditions were tested with a slower circular motion path (0.5 cycles in the 1 second trial) and a faster circular motion path (1.5 cycles in the 1 second trial).

The relationship between stimulus motion on the retina and acuity or other motion detection tasks are of interest in understanding the elements of retinal image motion that contribute to stimulus visibility and stability and understanding the implications of this stabilization. The goal of this study is to determine quantitatively the role that retinal image motion plays in the visual task of 2 AFC clockwise or counter-clockwise motion detection.

METHODS

Subjects: Five subjects with normal vision were recruited for this experiment. All subjects had best corrected acuities of 20/20 or better and were dilated for imaging. Informed consent was obtained from all subjects and the study protocol was approved by UC Berkeley and complied with the Declaration of Helsinki.

Stimulus Parameters and Psychophysical Experiment: In order to test the ability to detect motion under natural and manipulated eye motion conditions, a circular motion path was superimposed on the stimulus motion. All trials and stimulus presentations were 1 second and the starting point varied randomly between trials. Two different conditions were tested in which the stimulus moved one-half of a cycle (slow condition) or one and a half cycles (fast condition). For each motion condition, the radius of the superimposed circular path was varied

using a 2-down 1-up staircase procedure. All responses from multiple staircase procedures were combined to determine the threshold radii. The one-half cycle condition is illustrated in Figure 21.

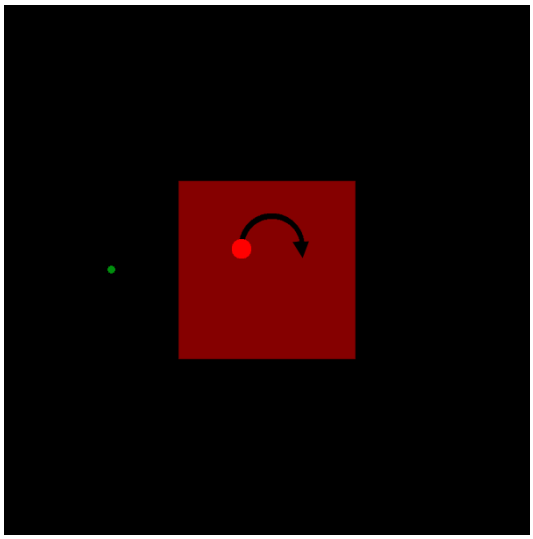

Figure 21: Stimulus motion for the motion experiments. Subjects fixated on a bright green dot and a bright red circular stimulus was presented within the dim red imaging raster with a circular motion added to the retinal image motion condition.

When this circular motion is superimposed on different retinal motion trajectories, the paths remain circular only in the stabilized condition. Under normal and other motion manipulations, there is considerable deviation from a circular path. Two examples for each of the tested conditions are illustrated in Figure 22.

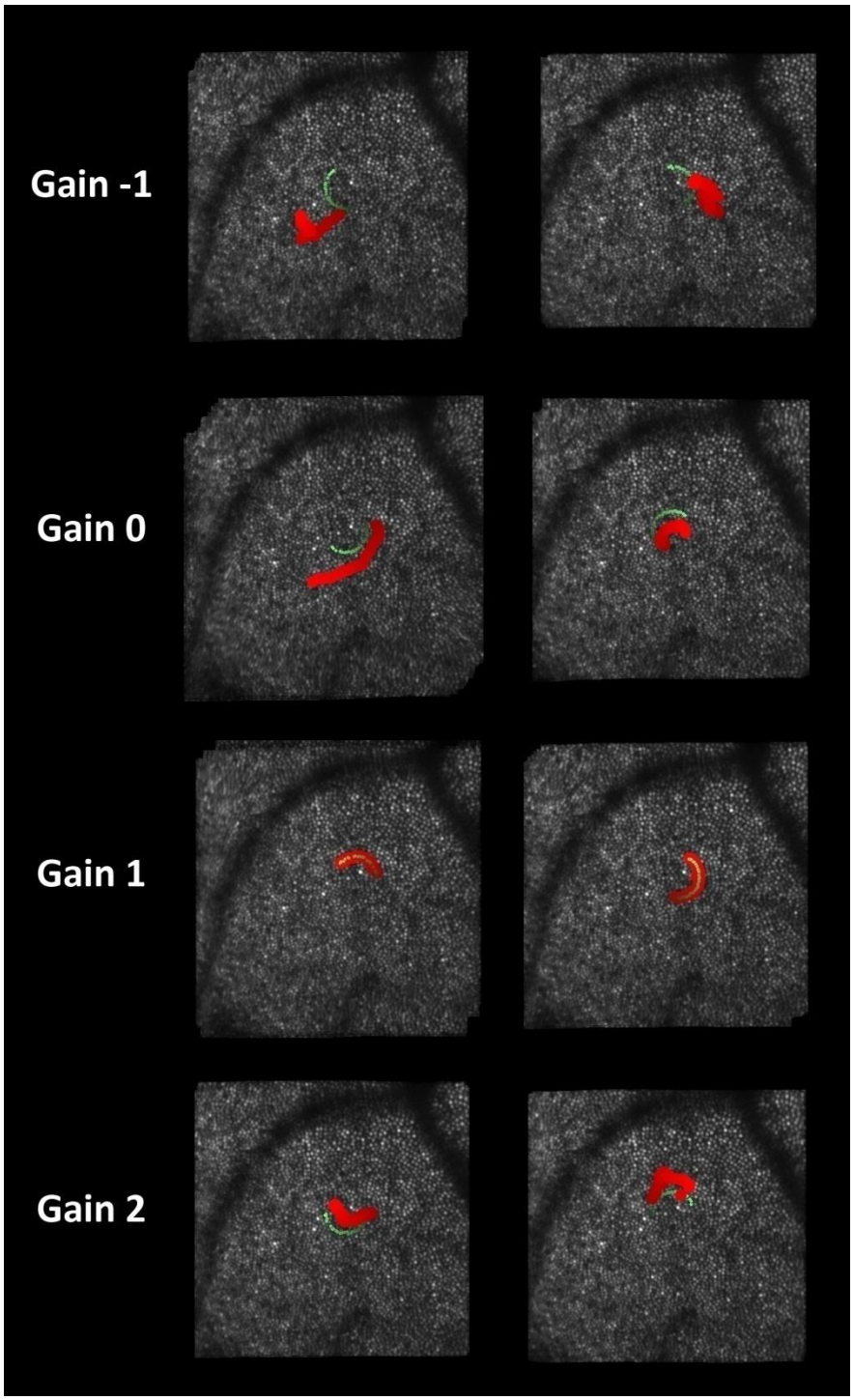

Figure 22: Examples of stimulus motion paths for the different conditions plotted on the retinal mosaic. For each of the gain conditions used in this experiment, the green paths represent the circular motion path that was added to the eye motion manipulation resulting in the final stimulus path shown in red.

RESULTS

There was considerable variability in the thresholds measured for different subjects. Figure 23 shows the results for the slow (0.5 Hz) and fast (1.5 Hz) stimulus conditions as well as the average thresholds for both conditions.

On average, the smallest thresholds occurred under natural eye motion conditions (gain 0) with a 2.5 arcmin radius for the slow condition and 0.8 arcmin radius for the fast condition. When the movement of the center of rotation of the stimulus was manipulated to be equal but opposite natural motion (gain 2), thresholds were 2.1 times larger for the slow condition and 2.5 times larger for the fast condition. When the stimulus traveled a perfect circular path on the retina and the center of rotation was stabilized (gain 1), thresholds were 1.4 times larger for the slow condition and 1.6 times larger for the fast condition. Finally, when the center of rotation of the retinal stimulus was doubled (gain -1), thresholds were 1.3 times larger for the slow condition and 1.5 times larger for the fast condition. When the retinal slip of the base movement was doubled (gain -1) or stabilized (gain 1), thresholds were elevated 1.34 and 1.37 times for the slow condition and 1.53 and 1.61 times for the fast condition. The error bars in Figure 23 represent the standard deviation. The only condition that was statistically significant was the difference between gain 0 and gain 2. There were small differences between gain -1 and gain 1, but they did not reach significance.

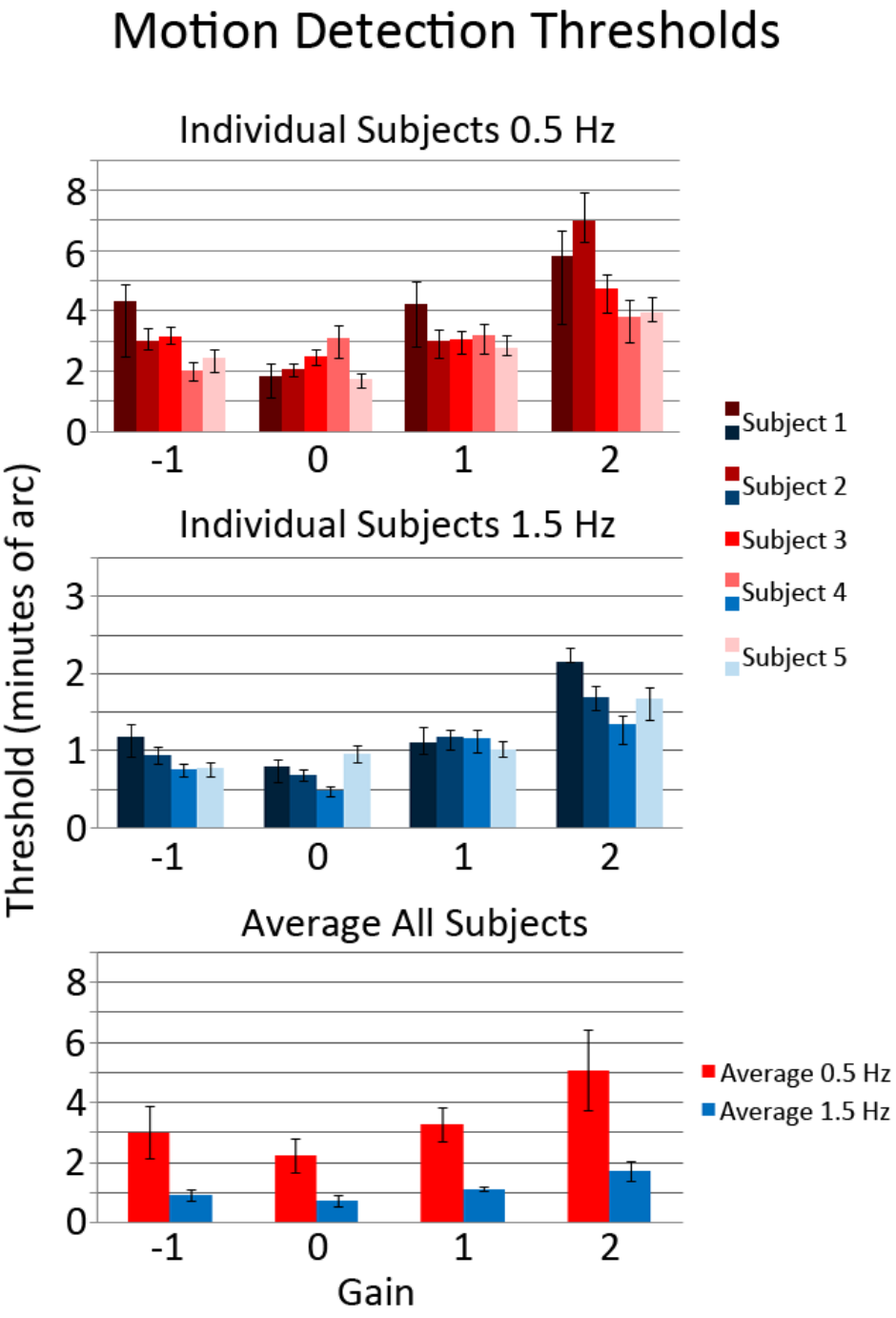

Figure 23: Results for the motion detection experiment. The top graphs show the thresholds for the 0.5 Hz (slow) condition in red for 5 subjects and the thresholds for the 1.5 Hz (fast) condition in blue for 4 subjects with the error bars representing the confidence intervals for the threshold fit. Average thresholds for all subjects for both the slow (red) and fast (blue) stimulus conditions are shown in the bottom graph with error bars representing the standard deviation.

DISCUSSION

Our results show that, on average, subject performance during a motion detection task is best under natural retinal image motion conditions. It is interesting that performance is diminished under the condition where retinal image motion is minimized (gain 1) as Figure 22 demonstrates that the natural, gain 0, condition can result in trajectories that are far from circular. It is also interesting to note that the threshold results do not seem to be dependent on the direction of imposed manipulated motion (both gain -1 and +1 result in comparably elevated thresholds) even though their retinal image motion trajectories differ considerably. As a result, it is clear that there is some compensation mechanism at work that is closest to an exact compensation scheme illustrated in Figure 20.

Although we proposed that this stimulus would be a way to better quantify the perceived motion phenomena that we found in our earlier experiments (Stevenson et al., 2010), the task is quite different. In the earlier experiment, the stimulus movement was directly yoked to eye motion. Here the only thing yoked to eye motion is the center of rotation. So the motions are only weakly correlated. But, given that there is a frame of reference (fixation point & raster) the eye can always use that to determine its motion.

B. MEASUREMENT OF CONTRAST THRESHOLDS AND THE ROLE OF FADING

In addition to the fact that objects that are constantly moving across the retina appear stable, when objects are fixed on a single retinal location, they actually fade from view. This fading of retinal images is a visual phenomenon that occurs when neurons in the visual system become adapted to a stimulus. Troxler's fading refers to the phenomenon where stimuli that are in the periphery disappear when someone fixates on a point for a few seconds (Martinez-Conde et al., 2006). In this case, small fixational eye movements drive stimulus motion and are small enough that the retinal image changes in the periphery are not large enough to produce visual signals. Fading has also been shown for images that are stabilized on the retina with specialized laboratory equipment (Ditchburn et al., 1959; Riggs et al., 1953; Steinman & Levinson, 1990). Riggs et al. tested stimuli as thin as 5.8 seconds of arc up to 93.3 seconds or arc and demonstrated fading of thin lines within seconds and reported that they would stay faded for the remainder of the 60 second trial with larger stimuli taking both longer to disappear and often reappearing. Ditchburn et al. discussed the fading of a larger stimulus a few arcmin in width stabilized in the center of the fovea, noting that the bar would disappear and reappear with a median time around 5 seconds. They noted that stimulus was seen for only approximately 2 seconds of that 5 second interval. They also concluded that the normal median drift itself is not large enough to prevent fading. Overall in these reports, there is much discussion of the disappearance and reappearance of stabilized images, with a time course that depends on retinal location, stimulus size, and contrast. For larger stimuli presented foveally fading was slower and not sustained compared with smaller stimuli presented eccentrically.

In order to understand the role of natural and manipulated fixational eye movements on contrast sensitivity and the role that motion plays in image fading, we performed two separate experiments. In the first experiment, we investigated the threshold for detection of a small

grating that increased in contrast over the course of a 6 second trial from invisible to visible. The location to be tested was presented with a cue for 0.33 seconds at the start of the trial with a button press. Subjects were then instructed to attend to the cued location and judge grating orientation as soon as they were able to make a judgment (2AFC right or left). This 2 AFC orientation judgment was intended to help subjects maintain better attention on the task, but was not used in the analysis. We recorded the contrast level at the time the decision was made under natural, stabilized and manipulated eye motion conditions. This experiment was performed at two different retinal locations, close to fixation at the center of the fovea and approximately 1 degree from the fovea. We then performed a second experiment to look at the time-course of image fading for small stimuli near the fovea under the natural motion condition, the stabilized condition, and conditions in-between. In this experiment, subjects were instructed to fixate on the corner of the red imaging raster and initiated a trial with the press of a button. A small 100% contrast grating was presented at a random location within the imaging field and subjects were instructed to press one button when the stimulus was no longer visible or to press another if the 9 second trial concluded with no image fading. We measured the time the stimulus was visible and the percentage of trials where the stimulus was visible for the entire 9 second trial.

METHODS

Subjects: Five subjects with normal vision were recruited for this set of experiments with a subset participating in each individual experiment. All subjects had best corrected acuities of 20/20 or better and were dilated for imaging. Informed consent was obtained from all subjects and the study protocol was approved by UC Berkeley and complied with the Declaration of Helsinki.

Stimulus Parameters and Psychophysical Experiment: We perform two experiments to look at different aspects of the problem. The first experiment was to determine the contrast level that can be detected as a stimulus ramps up in contrast over the course of a trial following a cue in the targeted location. The subjects were instructed to make a 2AFC judgment of grating orientation (L/R) to find the threshold contrast for grating orientation discrimination. Each trial started with a steady (gain 0) square stimulus for fixation to cue the tested location for 0.5 seconds. We then tested with a grating that slowly increases for a set delta contrast over 1.5 seconds. These tests were executed in a 1.9 degree field with a stimulus that displayed 3 cycles of a 15 cpd diagonal gabor for the test location close to the fovea near fixation and a 10 cpd diagonal gabor for the test location around 1 degree eccentricity. The second experiment was designed to simply determine the time for a 100% contrast 20 cpd stimulus to fade during a 9 second trial. The subjects initiated the trials and were instructed to press the L arrow when the stimulus could no longer be seen. The subjects were instructed to press the R arrow if the stimulus was seen for the entire 9 second trial. A mark was encoded in the video upon pressing the button in order for us to record the time to fade in post-processing.

RESULTS

When measuring the contrast required to detect a stimulus that was ramping up in contrast from invisible to visible over the course of a 6 second trial, the highest contrast required for all subjects occurred under stabilized conditions. The lowest thresholds were measured under negative gain conditions, where the stimulus was actually slipping across the retina and there were larger than normal amounts of stimulus motion. These experiments were performed both in the fovea and around 1 degree from the fovea and the results are illustrated in Figure 24 and summarized in Table 8.

Gain	-1	-0.5	0.01	0.5	1	1.5
Fovea	0.93	0.91	0.91	0.96	1	0.98
1 deg	0.91	0.92	0.94	0.95	1	0.95

Table 8: Summary of normalized contrast detection for a ramping stimulus at the fovea and 1 deg. The corresponding ratio of contrast condition for 6 gain conditions.

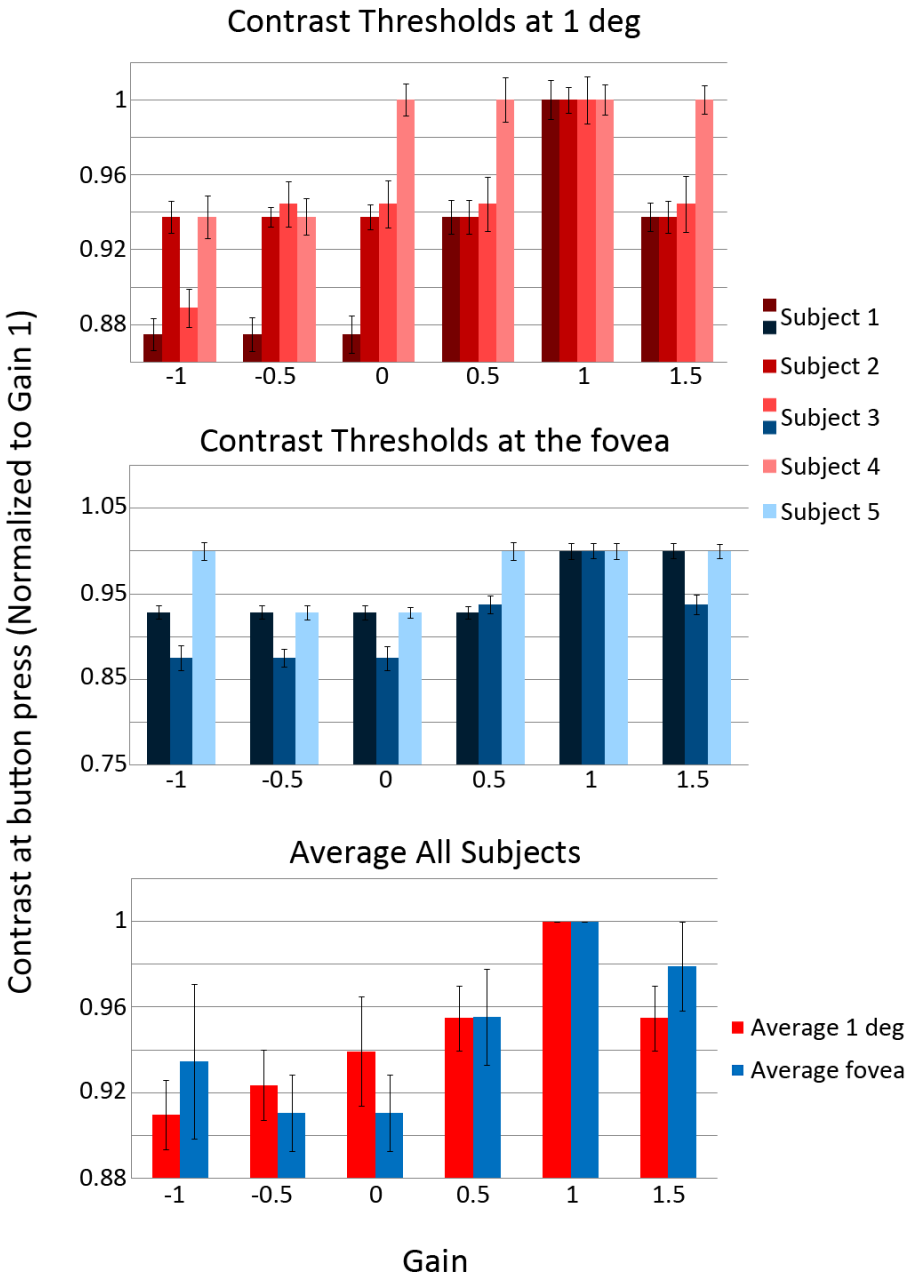

Figure 24: Contrast thresholds for a ramping stimulus. The stimulus was 3 diagonally oriented cycles of a 10 cpd grating at 1 degree and a 15 cpd grating in the fovea. Subjects performed a 2 AFC judgment of grating orientation and the time to button press was used to determine the contrast thresholds under different gain conditions. The top graph illustrates the results when the task was performed in the periphery around 1 degree and the middle when the experiment was performed close to the center of the fovea. For the top two graphs, data are normalized to the Gain 1 condition for the individual subject. The bottom graph displays the averages for all subjects for both conditions. The error bars represent the standard error of the mean.

We find that the time required for an image to fade was smallest under the stabilized (gain 1) condition and that there were no instances where the stimulus did not fade in the 9 second trials for three subjects. Under manipulated conditions where there was more motion added, the closer the condition became to the natural condition (gain 0), the longer it took for the image to fade and the more instances where the stimulus would not fade during an entire 9 second trial. These results are summarized in **Error! Reference source not found.** and **Error! Reference source not found.** and illustrated in **Error! Reference source not found.**.

Gain	0	0.2	0.5	0.8	1
Time to Fade (sec)	6.45	6.42	5.91	4.93	3.93

Table 9: Average time to fade in seconds for all subjects at different gain conditions.

Gain	0	0.2	0.5	0.8	1
% Did Not Fade	73.3	54.5	21.5	0.0	0.0

Table 10: Average percentage of trials that did not fade for all subjects at different gain conditions.

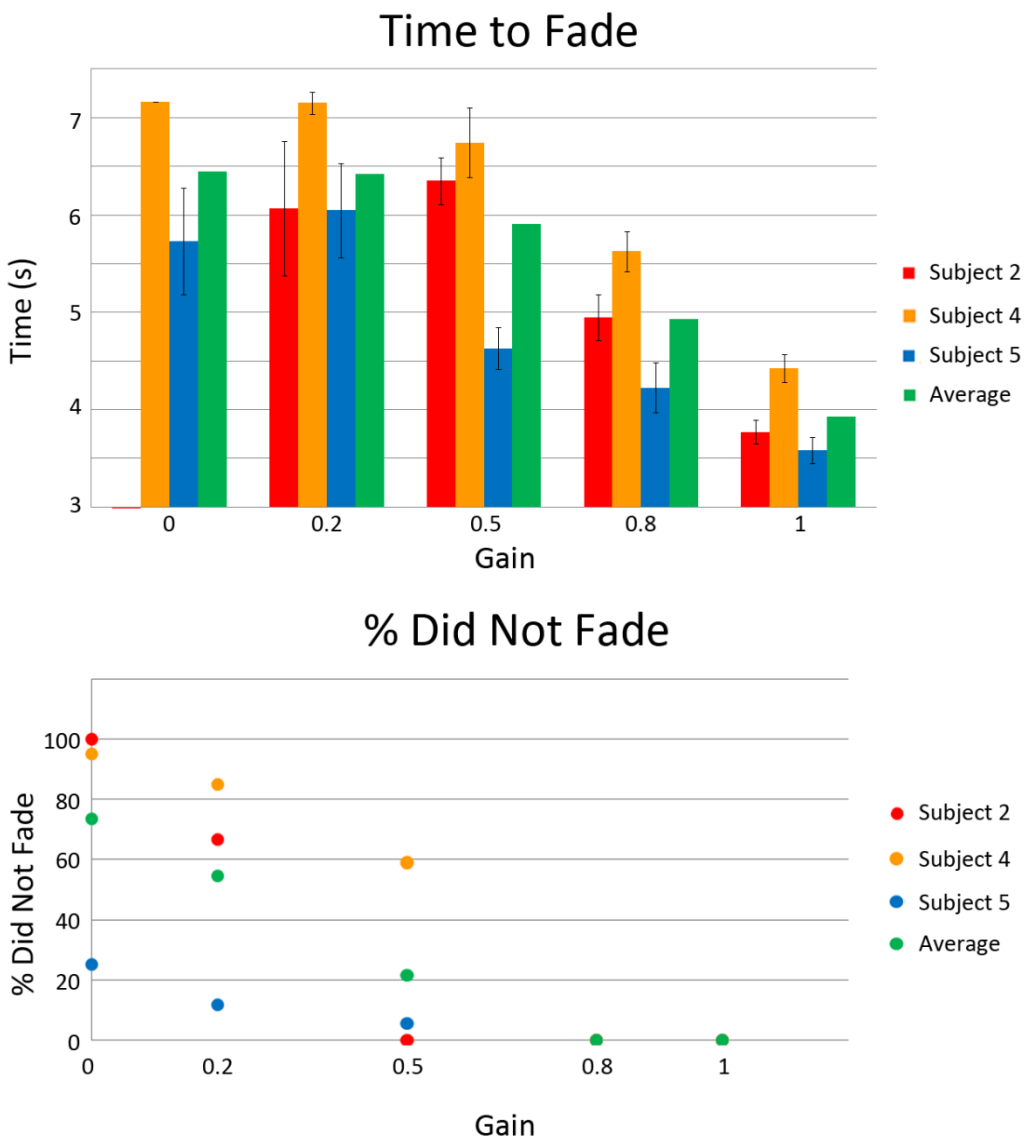

Figure 25: Time for a stimulus to fade and the percentage of stimuli faded for different motion conditions. The top graph shows the average time required for a stimulus placed close to the fovea to fade from view. The bottom graph illustrates the percentage of trials where the stimulus did not fade for the entire 9 second trial. The stimulus was 3 diagonally oriented cycles of a 20 cpd grating.

DISCUSSION

When we measured the time for an unchanging stimulus to fade, the shortest times were measured under stabilized conditions (gain 1) and there were no instances where the stimulus did not fade in the 9 second trials for all three subjects. When retinal image motion was added, the closer the condition became to the natural condition (gain 0), the longer it took for the image to fade and the more instances where the stimulus would not fade during an entire 9 second trial, as expected. Although the trends are similar for all three subjects, it is interesting to note that under normal conditions (gain 0), there were many instances where the image did fade for one subject while for another there were no instances of fading. These differences will be discussed in more detail later in the discussion as sources of fading. We did not test negative gain conditions in this experiment, but it is likely that the negative gain would have led to fewer instances of fading.

When we measured the contrast threshold for a stimulus ramping in contrast, the lowest contrast thresholds were measured under negative gain conditions. For all subjects, the highest contrast was required under stabilized conditions. These results show that the additional retinal motion associated with the stimulus slipping across the retina more than normal leads to increased sensitivity to contrast. This result is somewhat consistent with Macedo's result that increased retinal slip improves visual acuity (without crowding) in the periphery (Macedo et al., 2008).

In the contrast ramping experiment, there is a noted difference between the results in the fovea and at 1 degree. There are a number of important considerations that may lead to this difference. The first consideration is if the eye motion is optimal for foveal vision. This result suggests that it might be the case. At the fovea, retinal images that move slowly are less visible and retinal images that move too quickly are less visible. So, the actual eye movement generates the optimal temporal changes in the foveal photoreceptors that will provide optimal responsivity. In the periphery, the images have to move faster to reach the same temporal frequency. Another consideration is stabilization errors, which will be discussed below in more detail, which will have more effect in the center of the fovea than at 1 degree. There is also an important consideration that the stimulus presentation location varied from trial to trial. When the stimulus is presented in the periphery, the changing locations are still always in the same general direction with respect to fixation. When the stimulus is presented close to fixation, it is possible for the subject to be attending to a slightly different retinal location. In general, the subject has to work to fixate on the same spot (either in the imaging raster for presentation in the fovea or the corner of the raster for imaging around 1 degree) while attending to the stimulus, which is a more difficult task with a stimulus close to fixation. We expect that at least part of the noted differences are real as it is known from the literature that there are rapid changes in acuity directly outside of the fovea (Rossi & Roorda, 2010a) and fading occurs more often and more quickly outside the fovea (Martinez-Conde et al., 2004).

Contrast ramping allows us to test the role of image stabilization in a dynamic situation during a spatial acuity task. When a visual stimulus is presented quickly, the mechanisms behind retinal

stabilization do not have enough time to come into play. When a visual stimulus is presented for a long period of time, it will initially appear and may disappear and even reappear. We hypothesized that allowing the contrast to ramp up will mean that if it is below threshold and stabilized, even if the contrast does get high enough to detect, it may not be seen because the ramp was slow enough to prevent detection. Our data confirm that at and near stabilized conditions (gain 1), higher contrasts thresholds and lower percent of seeing were detected. Another important thing to note with this experiment is that the change in contrast might be enough to elicit some visual response. In this case, the thresholds might change with different retinal image motion conditions, but the stimulus will still appear at all times and the contrast levels measured may not be as predictable.

Mechanisms of fading: There are likely multiple mechanisms contributing to image fading, even close to or in the fovea. Generally speaking, they could be described as attention-based or stimulus-based fading. When a stimulus is not being attended, it may lead to less signal-to-noise in the neural activity associated with that stimulus, which could then cause it to fade away from view and blend with its surroundings. When a stimulus is stabilized on the retina, there is a decrease in retinal neural activity, which is demonstrated by an almost immediate decrease in the spike rate of parvocellular LGN cells with the presentation of a stabilized stimulus (Sincich et al., 2009). The question remains how do these two factors interact, as it is extremely difficult for a subject to attend to an object constantly, even close to the fovea, for an extended period of time? There is evidence in the literature for both these factors leading to stimulus fading. Troxler's fading is described in the literature in that stimuli in the periphery will fade from view after ~20 seconds. This effect is enhanced for small, low contrast, equiluminant and/or blurred stimuli. It is attributed to the adaptation of neurons and part of the general principle in sensory systems that an unvarying stimulus disappears from our awareness (Komatsu, 2006). Fading due to stabilized retinal images is also widely discussed in the literature, even for blinking stimuli. A classic example is afterimages that are bleached onto the retina by strong adaptation of rods and cones will disappear with time. To study this stabilization under controlled circumstances, a variety of laboratory setups have been created to eliminate or manipulate the motion of retinal stimuli (Ditchburn & Ginsborg, 1952; Riggs et al., 1953; Schieting & Spillman, 1987; Yarbus, Haigh, & Riggs, 1967).

Troxler's fading in particular could be a concern in long experiments, as many subjects' report that the entire AOSLO imaging raster can actually fade from view. This is of particular concern when a subject is tired or focusing hard on a task such as looking at a fixation target that is not co-located with the experiment. The focus of these experiments was to understand the role of retinal stabilization in fading, so we hoped to minimize the effect of Troxler's fading by presenting stimuli close to the fovea and ensuring that the subjects were well rested. The subjects were able to mark trials as bad in the event that the entire imaging field faded.

Previous experiments have shown that entoptic images of the blood vessels that cast shadows on the retina and are invisible under typical conditions fade extremely rapidly in comparison to laboratory-generated stimuli, which often fade more slowly. In general, smaller, lower contrast,

and lower spatial frequency stimuli presented at more eccentric retinal locations with very small stabilization errors have been shown to fade more rapidly. These variables all contribute to how quickly the visual system will adapt to, and as a result start to ignore, the visual signal created by the stimulus. When we repeated measurements in the same location for an experiment where the subject was instructed to report whether the image faded or not and the trial length was modified, it appeared that the images would fade much more rapidly as time went on. This might be tapping into some of this retinal adaptation where returning to the exact location many times in a short period of time is allowing the situation to more closely mimic that of an entoptic image where the retina would be continually adapted to the fixed blood vessels within the retina. Other studies in our lab measuring sensitivity of individual cones have shown thresholds to increase over the course of a set of trials, which may also be part of this retinal adaptation. There are two types of fatigue: retinal fatigue and the resulting adaptation and subject fatigue during a long experiment. The later is a confounding factor that can also lead to image fading and has been known to lead to the entire imaging raster to fade for some subjects.

Stabilization errors: A potential problem with all experiments in this chapter is that the retinal stabilization (or targeting with a different gain condition) is not perfect due to large amounts of motion associated with normal fixational eye movements. When we are performing experiments in the center of the fovea, or close to it, using a small field (due to system limitations), the resulting images are void of large retinal landmarks such as blood vessels or large cone photoreceptor structure like there would be at more eccentric retinal locations. These small changes in retinal position related to inaccuracy in stabilization/targeting may be large enough to elicit a visual response and elevate thresholds. It is critical to determine good vs. bad trials in this task and exclude trials with potential confounding artifacts from the analysis. Fading will not occur under poor stabilization conditions, so the additional analysis considering the reliability of the tracking after the fact allows us to discard bad trials.

This is also important in considering the differences between experiments performed in the fovea and just outside the fovea. The retinal imaging is much easier and higher fidelity away from the fovea, due to the considerations discussed in the earlier chapters of this dissertation. As a result, the image stabilization and targeted stimulus delivery works both more reliably and with shorter delay times when imaging at this location. In addition, there is evidence from the literature that retinal slip may enhance visual acuity in the periphery where more motion is required for an image to cross the same number of photoreceptors (Macedo et al., 2008).

Subjects' observations: There were some interesting observations made by all subjects' in regard to stimulus appearance. The first was that the descriptions of a 100% contrast stimulus fixated foveally under a stabilized (gain 1) condition were that the stimulus does disappear after some time (average around 2 seconds), but they would get an inverse or embossed image appearing again from time to time for brief periods that will quickly fade again. There are reasonable explanations for why this happens that include stimulus stabilization errors or occasions where the subject makes a larger eye movement away from the stimulus and then

back. As a result, training was extremely important in this task such that the subjects are clearly aware and able to discriminate trials where a stimulus fades in comparison to trials where the stimulus disappears because the trial is over. There is an audible cue at the end of each trial to help with this. The second observation was that all subjects observed large differences in stimulus appearance from trial to trial, even when no stimulus properties were changed. These differences are not correlated with the amount of time the subject had been in the imaging system or presentation location as they occurred at many locations and did not show any clear trends.

Magnitude of eye motion: We investigated alternative approaches to the analysis of the data. One approach was to bin thresholds based on the magnitude of the eye motion during the trial, but results were not significantly different. It is possible that the judgment might be made earlier in the trial or it might be a threshold of how the eye is moving that is important. We could also approach the analysis differently and look at the percent of trials correctly identified for different gain conditions or something comparable.

Power fluctuations: It is also important to note that the absolute values of our measured contrast thresholds may change from day to day due to fluctuations in the imaging laser power. Even over the course of an individual experiment, the laser power has been found to fluctuate on occasion. The trends for all experiments are consistent between subjects imaged on different days, however, and this was part of the motivation behind normalizing the data for presentation in Figure 24.

CONCLUSIONS AND FUTURE DIRECTIONS

We demonstrate the ability to make quantitative psychophysical measurements of motion detection, contrast, and fading under natural and manipulated stimulus motion trajectories using customized image acquisition and dynamic stimulus presentation with AOSLO.

True motion is perceived despite confounding retinal image motion and subjects' perform best under natural conditions. Despite the fact that stimuli appear more stable under manipulated eye motion conditions consistent with natural eye motion, this does not seem to aid in the detection of circular motion. It is likely that there are different mechanisms interacting, resulting in the variety of visual percepts observed under different stimulus motion conditions. The illusion of stability under negative gain conditions also allows for the detection of stimuli of lower contrast, but it inhibits motion detection. The natural condition (gain 0) also leads to a stable percept of objects in the world and allows for the smallest motion detection thresholds while inhibiting contrast detection in comparison to negative gain conditions. Finally, we have the condition of retinal stability (gain 1), under which images are most likely to fade and fade quickly and performance in contrast and motion detection tasks is diminished even though there is the smallest amount of stimulus motion on the retina. One suggested explanation for these observations was that if there is a fixed frequency ideal for a given cone spacing measurement or if there is an advantage to using the maximum density of cones. Is it possible

that fixation along the steepest gradient of cone density could provide an advantage for high-acuity tasks?

Future directions for eye motion experiments could include investigating a completely independent eye motion (for example, delay the motion by 1 trial), decreasing the stimulus intensity, removing the imaging field reference with a moving or tapered field edge or adding a background that masks the imaging field, looking at the direction and velocity of eye movements resulting when a stabilized stimulus is placed close to the fovea and the similar condition of testing the change from stabilized to unstabilized and vice versa. Longer stimuli (it is possible that the time-course over which we can appreciate the stability is longer or the stabilization wasn't "locked on" in the same way throughout our experiments). The ultimate goal would be to explore other conditions or tasks where the illusion of stability under negative gain condition leads to increased visual performance similar to the results we found in the contrast ramping experiment.

It will be interesting to extend these quantitative measurements to broader measurements of contrast sensitivity. In addition, it would be interesting to remove the frame of reference in order to test unreferenced motion manipulations. Finally, it would also be interesting to extend these findings to situations with multiple stimuli moving with independent motion manipulations.

ACKNOWLEDGEMENTS

Co-Authors on a paper presentation of this material at the OSA Fall Vision Meeting in September, 2011: Pavan Tiruveedhula (Vision Science Graduate Group, University of California, Berkeley), Qiang Yang (Center for Computational Biology, Montana State University), David W. Arathorn (Center for Computational Biology, Montana State University), Scott B. Stevenson (College of Optometry, University of Houston), and Austin Roorda (Vision Science Graduate Group, University of California, Berkeley)

REFERENCE LIST

Adler, F. H., & Fliegelman, M. (1934). Influence of Fixation on the Visual Acuity. *Archives of Ophthalmology*, *12*(4), 475–483.

Arathorn, D. W., Yang, Q., Vogel, C. R., Zhang, Y., Tiruveedhula, P., & Roorda, A. (2007). Retinally stabilized cone-targeted stimulus delivery. *Optics express*, *15*(21), 13731–44.

Babcock, H. W. (1953). The Possibility of Compensating Astronomical Seeing. *JSTOR: Publications of the Astronomical Society of the Pacific, Vol. 65, No. 386*.

Barlow, H. (1997). Neuroscience: Adaptation by Hyperpolarization. *Science*, *276*(5314), 913–914.

Barlow, H. B. (1952). Eye Movements During Fixation. *J. Physiol*. Retrieved December 19, 2011, from http://jp.physoc.org/content/116/3/290.full.pdf

Baron, W. S., & Westheimer, G. (1973). Visual acuity as a function of exposure duration. *Journal of the Optical Society of America*, *63*(2), 212.

Bedggood, P., Daaboul, M., Ashman, R., Smith, G., & Metha, A. (2008). Characteristics of the human isoplanatic patch and implications for adaptive optics retinal imaging. *Journal of biomedical optics*, *13*(2), 024008.

Bigelow, C. E., Iftimia, N. V., Ferguson, R. D., Ustun, T. E., Bloom, B., & Hammer, D. X. (2007). Compact multimodal adaptive-optics spectral-domain optical coherence tomography instrument for retinal imaging. *Journal of the Optical Society of America. A, Optics, image science, and vision*, *24*(5), 1327–36.

Born, M., & Wolf, E. (2000). *Principles of Optics: Electromagnetic Theory of Propagation, Interference and Diffraction of Light*. Cambridge University Press, London, UK.

Borwein, B. (1983). Scanning electron microscopy of monkey foveal photoreceptors. *The Anatomical record*, *205*(3), 363–73.

Boyce, P. R. (1967). Monocular Fixation in Human Eye Movement. *Proceedings of the Royal Society B: Biological Sciences*, *167*(1008), 293–315.

Bridgeman, B. (1995). A review of the role of efference copy in sensory and oculomotor control systems. *Annals of Biomedical Engineering*, *23*(4), 409–422.

Burns, S. A., Tumbar, R., Elsner, A. E., Ferguson, D., & Hammer, D. X. (2007). Large-field-of-view, modular, stabilized, adaptive-optics-based scanning laser ophthalmoscope. *Journal of the Optical Society of America A*, *24*(5), 1313.

Chui, T. Y. P., Zhong, Z., Song, H., & Burns, S. A. (2012). Foveal avascular zone and its relationship to foveal pit shape. *Optometry and vision science : official publication of the American Academy of Optometry*, *89*(5), 602–10.

Cornsweet, T. N. (1956). Determination of the Stimuli for Involuntary Drifts and Saccadic Eye Movements. *Journal of the Optical Society of America*, *46*(11), 987.

Curcio, C. A., Sloan, K. R., Kalina, R. E., & Hendrickson, A. E. (1990). Human photoreceptor topography. *The Journal of comparative neurology*, *292*(4), 497–523.

De Valois, R. L., & De Valois, K. K. (1980). Spatial vision. *Annual review of psychology*, *31*, 309–41.

Ditchburn, R W, & Ginsborg, B. L. (1953). Involuntary eye movements during fixation. *The Journal of physiology*, *119*(1), 1–17.

Ditchburn, R. W. (1973). *Eye-movements and visual perception.* Oxford: Clarendon Press.

Ditchburn, R.W., Fender, D. H., & Mayne, S. (1959). Vision with controlled movements of the retinal image. *The Journal of physiology*, *145*(1), 98–107.

Ditchburn, R.W., & Ginsborg, B. L. (1952). Vision with a Stabilized Retinal Image. *Nature*.

Dowling, J. E. (1987). *The Retina: An Approachable Part of the Brain, Part 747* (p. 282). Harvard University Press.

Dreher, A. W., Bille, J. F., & Weinreb, R. N. (1989). Active optical depth resolution improvement of the laser tomographic scanner. *Applied Optics*, *28*(4), 804.

Enoch, J. M. (1963). Optical Properties of the Retinal Receptors. *Journal of the Optical Society of America*, *53*(1), 71.

Gao, W., Cense, B., Zhang, Y., Jonnal, R. S., & Miller, D. T. (2008). Measuring retinal contributions to the optical Stiles-Crawford effect with optical coherence tomography. *Optics express*, *16*(9), 6486–501.

Gibson, J. J. (1954). The visual perception of objective motion and subjective movement. *Psychological Review*, *61*(5), 304–314.

Glezer, V. D. (1965). The receptive fields of the retina. *Vision Research*, *5*(10-11), 497–525.

Greivenkamp, J. E. (2003). *Field Guide to Geometrical Optics (SPIE Vol. FG01)*. SPIE Publications.

Grieve, K., Tiruveedhula, P., Zhang, Y., & Roorda, A. (2006). Multi-wavelength imaging with the adaptive optics scanning laser Ophthalmoscope. *Optics express*, *14*(25), 12230–42.

Helmholtz, H. (1925). *Treatise on physiological optics. III. The perceptions of vision.* (J. P. C. Southall, Ed.). New York: Optical Society of America.

Hermann, B., Michels, S., Leitgeb, R., Ahlers, C., Povazay, B., Sacu, S., Sattmann, H., et al. (2005). Thickness Mapping of Photoreceptors of the Foveal Region in Normals Using Three-Dimensional Optical Coherence Tomography. *ARVO Meeting Abstracts*, *46*(5), 3971.

Hubel, D. H., & Wiesel, T. N. (1959). Receptive Fields of Single Neurones in the Cat's Striate Cortex. *The Journal of Physiology 148*.

Jonnal, R. S., Besecker, J. R., Derby, J. C., Kocaoglu, O. P., Cense, B., Gao, W., Wang, Q., et al. (2010). Imaging outer segment renewal in living human cone photoreceptors. *Optics express*, *18*(5), 5257–70.

Jonnal, R. S., Rha, J., Zhang, Y., Cense, B., Gao, W., & Miller, D. T. (2007). In vivo functional imaging of human cone photoreceptors. *Optics express*, *15*(24), 16141–60.

Kotulak, J. C., & Schor, C. M. (1985). The accommodative response to subthreshold blur and to perceptual fading during the Troxler phenomenon. *Perception*.

Kumar, G. (2008). The Retinal Origin : On the independence of retinal loci targeted by saccades, pursuits and fixation and their relationship to the retinal point of perceived fixation (Doctoral dissertation). University of Houston, Houston.

Legge, G. E., & Campbell, F. W. (1981). Displacement detection in human vision. *Vision Research*, *21*(2), 205–213.

Li, K. Y., & Roorda, A. (2007). Automated identification of cone photoreceptors in adaptive optics retinal images. *Journal of the Optical Society of America. A, Optics, image science, and vision*, *24*(5), 1358–63.

Li, K. Y., Tiruveedhula, P., & Roorda, A. (2010). Intersubject variability of foveal cone photoreceptor density in relation to eye length. *Investigative ophthalmology & visual science*, *51*(12), 6858–67.

Liang, J., Williams, D. R., & Miller, D. T. (1997). Supernormal vision and high-resolution retinal imaging through adaptive optics. *Journal of the Optical Society of America. A, Optics, image science, and vision*, *14*(11), 2884–92.

Macedo, A. F., Crossland, M. D., & Rubin, G. S. (2008). The effect of retinal image slip on peripheral visual acuity. *Journal of vision*, *8*(14), 16.1–11.

Martinez-Conde, S., Macknik, S. L., & Hubel, D. H. (2004). The role of fixational eye movements in visual perception. *Nature reviews. Neuroscience*, *5*(3), 229–40.

Martinez-Conde, S., Macknik, S. L., Troncoso, X. G., & Dyar, T. A. (2006). Microsaccades counteract visual fading during fixation. *Neuron*, *49*(2), 297–305.

McKee, S., Welch, L., Taylor, D., & Bowne, S. (1990). Finding the common bond: Stereoacuity and the other hyperacuities. *Vision Research*, *30*(6), 879–891.

Merino, D., Duncan, J. L., Tiruveedhula, P., & Roorda, A. (2011). Observation of cone and rod photoreceptors in normal subjects and patients using a new generation adaptive optics scanning laser ophthalmoscope. *Biomedical optics express*, *2*(8), 2189–201.

Morgan, J. I. W., Dubra, A., Wolfe, R., Merigan, W. H., & Williams, D. R. (2009). In vivo autofluorescence imaging of the human and macaque retinal pigment epithelial cell mosaic. *Investigative ophthalmology & visual science*, *50*(3), 1350–9.

Murakami, I., & Cavanagh, P. (1998). A jitter after-effect reveals motion-based stabilization of vision. *Nature*, *395*(6704), 798–801.

Nakayama, K., & Tyler, C. W. (1981). Psychophysical isolation of movement sensitivity by removal of familiar position cues. *Vision Research*, *21*(4), 427–433.

Østerburg, G. A. (1935). Topography of the layer of rods and cones in the human retina. *Acta Ophthalmologica (Suppl.)*, *13*(6), 1–97.

Pallikaris, A., Williams, D. R., & Hofer, H. (2003). The Reflectance of Single Cones in the Living Human Eye. *Investigative Ophthalmology & Visual Science*, *44*(10), 4580–4592.

Poletti, M., Listorti, C., & Rucci, M. (2010). Stability of the visual world during eye drift. *The Journal of neuroscience : the official journal of the Society for Neuroscience*, *30*(33), 11143–50.

Polyak, S. L. (1941). *The retina: the anatomy and the histology of the retina in man, ape, and monkey, including the consideration of visual functions, the history of physiological optics, and the histological laboratory technique.* Chicago: University of Chicago Press.

Poonja, S., Patel, S., Henry, L., & Roorda, A. (2005). Dynamic visual stimulus presentation in an adaptive optics scanning laser ophthalmoscope. *Journal of refractive surgery, 21*(5), 575–80.

Putnam, N. M., Hofer, H. J., Doble, N., Chen, L., Carroll, J., & Williams, D. R. (2005). The locus of fixation and the foveal cone mosaic. *Journal of vision*, *5*(7), 632–9.

Raghunandan, A., Frasier, J., Poonja, S., Roorda, A., & Stevenson, S. B. (2008). Psychophysical measurements of referenced and unreferenced motion processing using high-resolution retinal imaging. *Journal of vision*, *8*(14), 14.1–11.

Ratliff, F., & Riggs, L. a. (1950). Involuntary motions of the eye during monocular fixation. *Journal of experimental psychology*, *40*(6), 687–701.

Riggs, L. A., Ratliff, F., Cornsweet, J. C., & Cornsweet, T. N. (1953). The Disappearance of Steadily Fixated Visual Test Objects. *Journal of the Optical Society of America*, *43*(6), 495.

Roorda, A. (2010). Applications of adaptive optics scanning laser ophthalmoscopy. *Optometry and vision science : official publication of the American Academy of Optometry*, *87*(4), 260–8.

Roorda, A. J., & Zhang, Y. (2005). Mechanism for Cone Reflectivity Revealed With Low Coherence AOSLO Imaging. *ARVO Meeting Abstracts*, *46*(5), 2433.

Roorda, A., Romero-Borja, F., Donnelly, I., Queener, H., Hebert, T., & Campbell, M. (2002). Adaptive optics scanning laser ophthalmoscopy. *Optics Express*, *10*(9), 405–412.

Roorda, A., & Williams, D. R. (1999). The arrangement of the three cone classes in the living human eye. *Nature*, *397*(6719), 520–2.

Roorda, A., & Williams, D. R. (2002). Optical fiber properties of individual human cones. *Journal of vision*, *2*(5), 404–12.

Rossi, E.A., & Roorda, A. (2006). The limits of high contrast photopic visual acuity with adaptive optics. *Investigative ophthalmology & visual science, 47,* 5402.

Rossi, Ethan A, & Roorda, A. (2010a). The relationship between visual resolution and cone spacing in the human fovea. *Nature neuroscience*, *13*(2), 156–7.

Rossi, Ethan A, & Roorda, A. (2010b). Is visual resolution after adaptive optics correction susceptible to perceptual learning? *Journal of vision*, *10*(12), 11.

Rossi, Ethan A, Weiser, P., Tarrant, J., & Roorda, A. (2007). Visual performance in emmetropia and low myopia after correction of high-order aberrations. *Journal of vision*, *7*(8), 14.

Rucci, M., Iovin, R., Poletti, M., & Santini, F. (2007). Miniature eye movements enhance fine spatial detail. *Nature*, *447*(7146), 851–4.

Schieting, S., & Spillman, L. (1987). Flicker Adaptation in the Peripheral Retina. *Vision research*, *27*(2), 277–284.

Schultze, M. (1873). The retina. In S. Stricker (Ed.), *Manual of human and comparative histology*. London: New Sydenham Society.

Sincich, L. C., Zhang, Y., Tiruveedhula, P., Horton, J. C., & Roorda, A. (2009). Resolving single cone inputs to visual receptive fields. *Nature neuroscience*, *12*(8), 967–9.

Smith, A. T. (2001). Estimating Receptive Field Size from fMRI Data in Human Striate and Extrastriate Visual Cortex. *Cerebral Cortex*, *11*(12), 1182–1190.

Steinman, R. M., & Levinson, J. Z. (1990). The role of eye movement in the detection of contrast and spatial detail. In E. Kowler (Ed.), *Eye movements and their role in visual and cognitive processes* (Vol. 4, pp. 115–212). Elsevier Science Publishers BV (Biomedical Division).

Steinman, Robert M. (1965). Effect of Target Size, Luminance, and Color on Monocular Fixation. *Journal of the Optical Society of America*, *55*(9), 1158.

Steinman, Robert M., Haddad, G. M., Skavenski, A. A., & Wyman, D. (1973). Miniature Eye Movement. *Science*.

Stevenson, S. B., & Roorda, A. (2005). Correcting for miniature eye movements in high resolution scanning laser ophthalmoscopy. *Proceedings of SPIE,* 5688, 145–151.

Stevenson, S. B., Roorda, A., & Kumar, G. (2010). Eye tracking with the adaptive optics scanning laser ophthalmoscope. *Proceedings of the 2010 Symposium on Eye-Tracking Research & Applications – ETRA,* 195. New York, New York, USA: ACM Press.

Stevenson, S., Kumar, G., & Roorda, A. (2007). Psychophysical and oculomotor reference points for visual direction measured with the adaptive optics scanning laser ophthalmoscope. *Journal of Vision*, *7*(9), 137–137.

Stevenson, Scott, Arathorn, D., Yang, Q., Tiruveedhula, P., Putnam, N., & Roorda, A. (2010). Suppression of retinal image motion due to fixation jitter is directionally biased. *Journal of vision*.

Tulunay-Keesey, U., & Verhoeve, J. (1987). The role of eye movements in motion detection. *Vision Research*, *27*(5), 747–754.

Vogel, C. R., Arathorn, D. W., Roorda, A., & Parker, A. (2006). Retinal motion estimation in adaptive optics scanning laser ophthalmoscopy. *Optics express*, *14*(2), 487–97.

Walls, G. L. (1942). *The Vertebrate Eye and Its Adaptive Radiation* (p. 785). Hafner.

Westheimer, G. (1967). Dependence of the Magnitude of the Stiles-Crawford Effect on Retinal Location. *J. Physiol.*, *192*, 309–315.

Weymouth, F. W., Hines, D. C., Acres, L. H., Raaf, J. E., & Wheeler, M. C. (1928). Visual acuity within the area centralis and its relation to eye movements and fixation. *American Journal of Ophthalmology*, *11*, 947–960.

Wichmann, F. A., & Hill, N. J. (2001a). The psychometric function: I. Fitting, sampling, and goodness of fit. *Perception & Psychophysics*, *63*(8), 1293–1313.

Wichmann, F. A., & Hill, N. J. (2001b). The psychometric function: II. Bootstrap-based confidence intervals and sampling. *Perception & Psychophysics*, *63*(8), 1314–1329.

Williams, D. R. (1980). Visual consequences of the foveal pit. *Investigative ophthalmology & visual science*, *19*(6), 653–67.

Wilson, T., & Sheppard, C. (1984). Theory and practice of scanning optical microscopy. *London: Academic Press*.

Yang, Q., Arathorn, D. W., Tiruveedhula, P., Vogel, C. R., & Roorda, A. (2010). Design of an integrated hardware interface for AOSLO image capture and cone-targeted stimulus delivery. *Optics Express*, *18*(17), 17841.

Yarbus, A. L., Haigh, B., & Riggs, L. A. (1967). Eye movements and vision.

Zhang, Y., Poonja, S., & Roorda, A. (2006a). MEMS-based adaptive optics scanning laser ophthalmoscopy. *Optics letters*, *31*(9), 1268–70.

Zhang, Y., Poonja, S., & Roorda, A. (2006b). AOSLO: from benchtop to clinic. *Proceedings of SPIE*, *6306*, 63060V–63060V–11.

Zhang, Y., & Roorda, A. (2006). Evaluating the lateral resolution of the adaptive optics scanning laser ophthalmoscope. *Journal of biomedical optics*, *11*(1), 014002.

Zhang, Y., & Roorda, A. (2007). Photon signal detection and evaluation in the adaptive optics scanning laser ophthalmoscope. *Journal of the Optical Society of America. A, Optics, image science, and vision*, *24*(5), 1276–83.

Zou, W., Qi, X., & Burns, S. A. (2008). Wavefront-aberration sorting and correction for a dual-deformable-mirror adaptive-optics system. *Optics Letters*, *33*(22), 2602.

APPENDIX 1

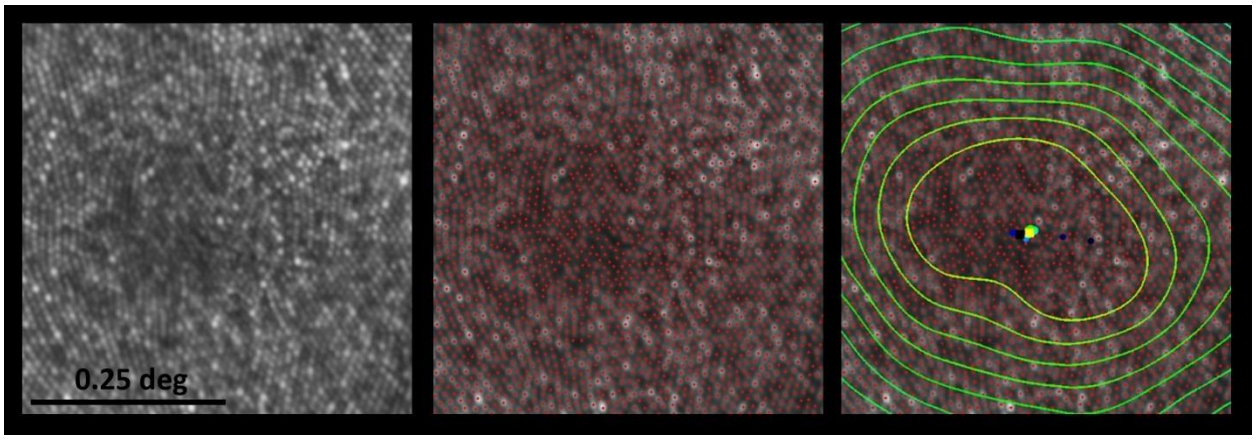

Figure 26: Label centroids of iso-density curves. The yellow square identifies the location estimated from outside contours and the black square identifies the location used for this subject identified from 11 central iso-density curves.

APPENDIX 2

The six figures that follow (Figure 27-Figure 32) show the fitting procedure for all eyes on both days.

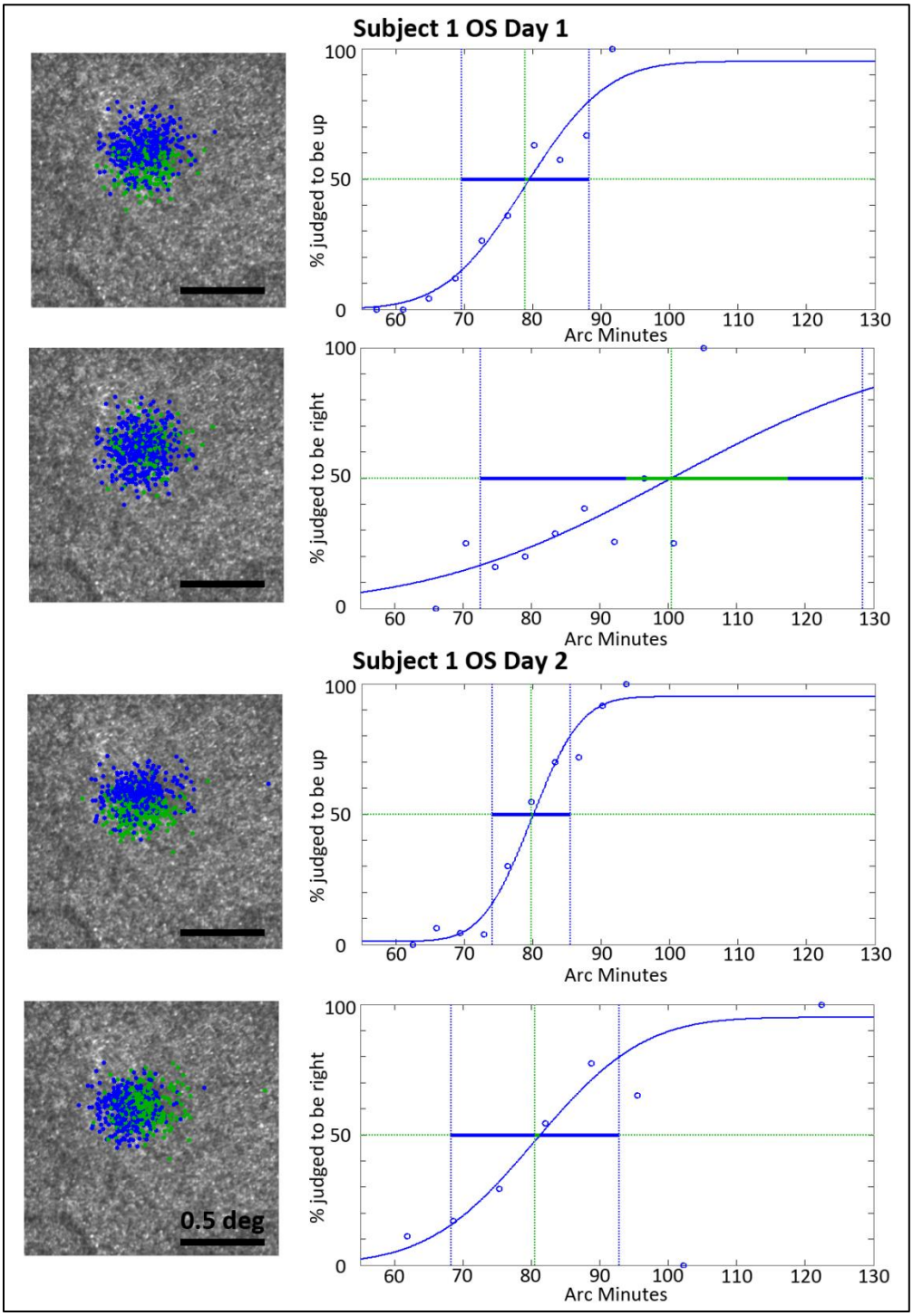

Figure 27: Subject 1 OS Cumulative Gaussian Fits for the PFD.

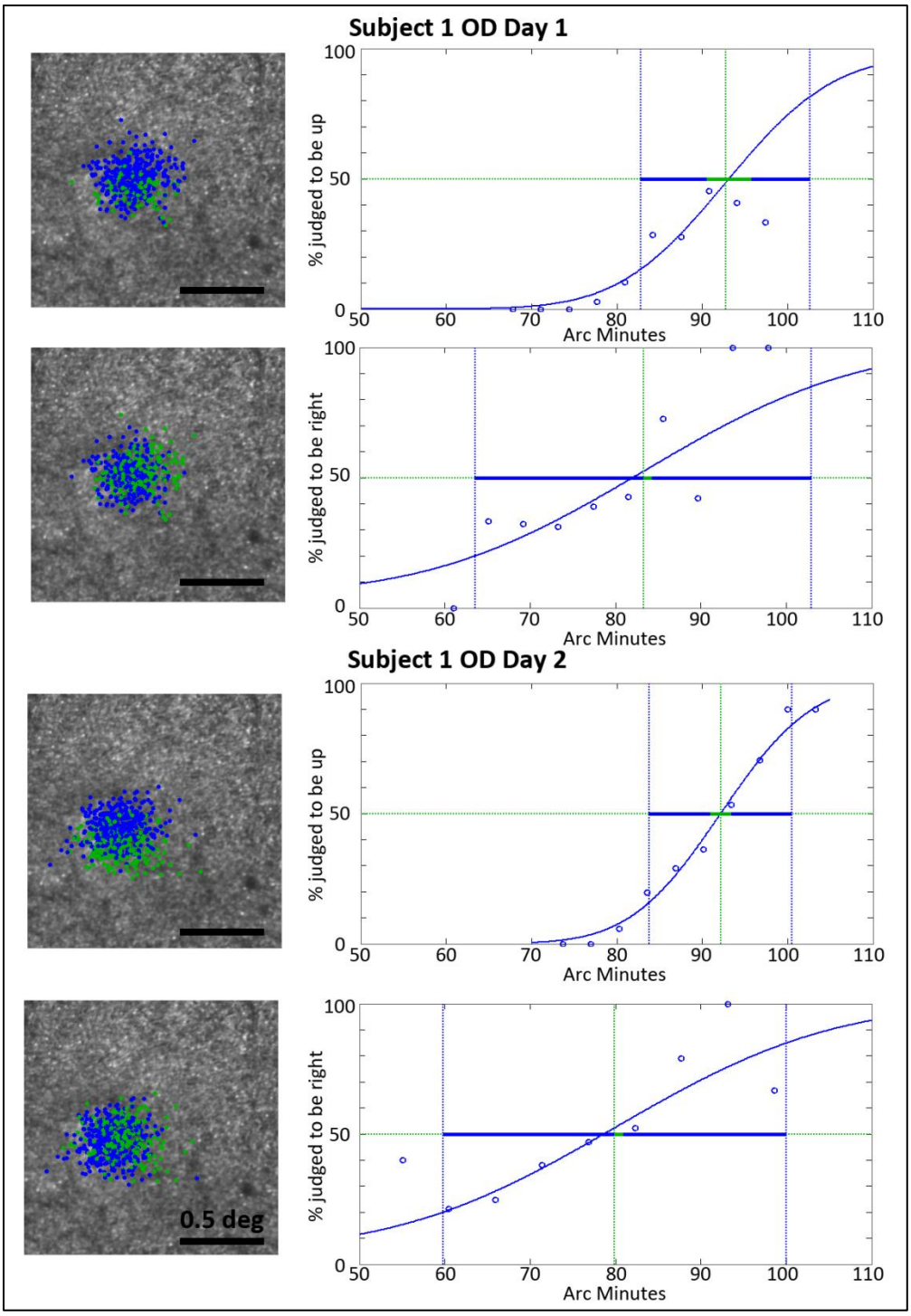

Figure 28: Subject 1 OD Cumulative Gaussian Fits for the PFD.

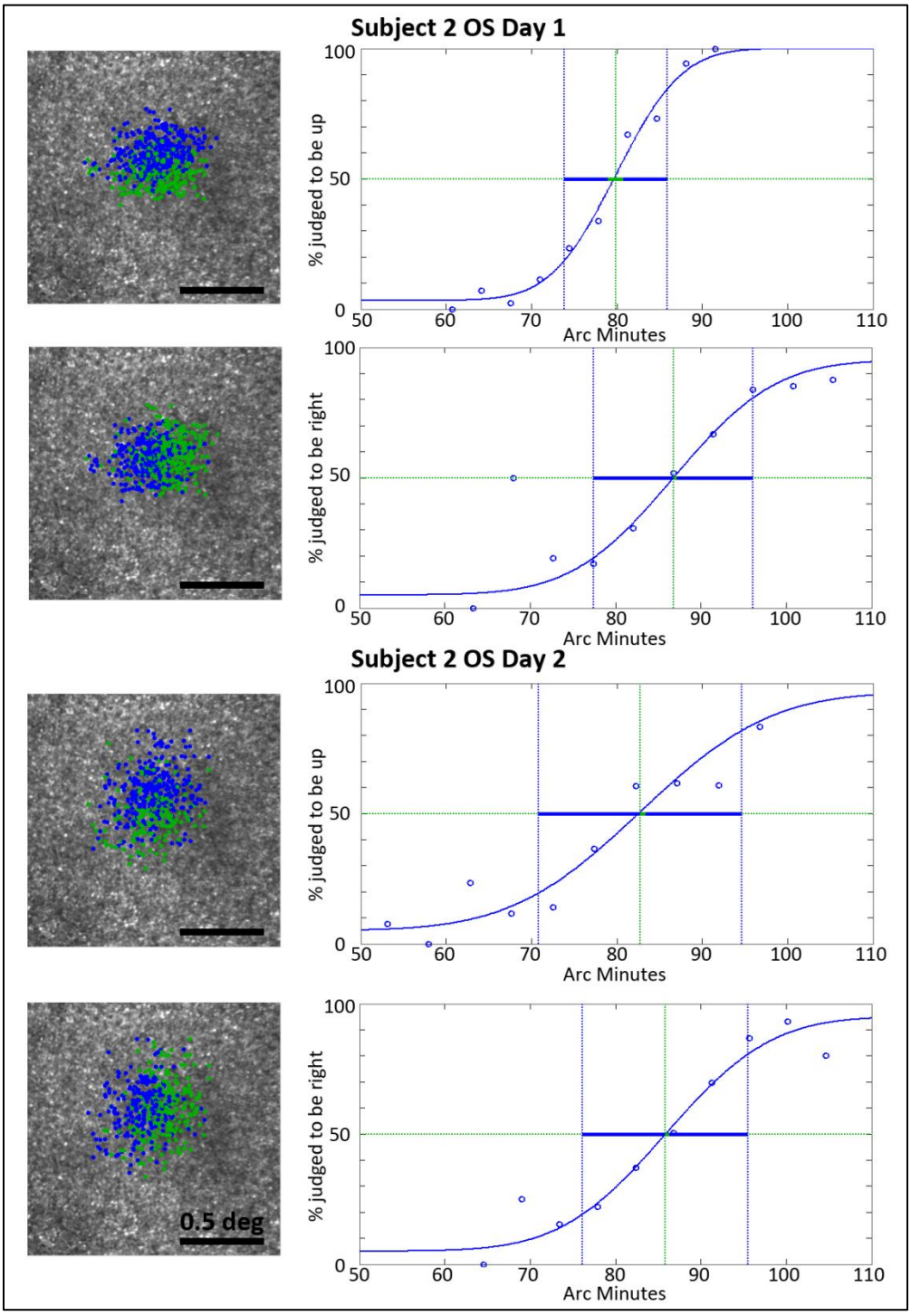

Figure 29: Subject 2 OS Cumulative Gaussian Fits for the PFD.

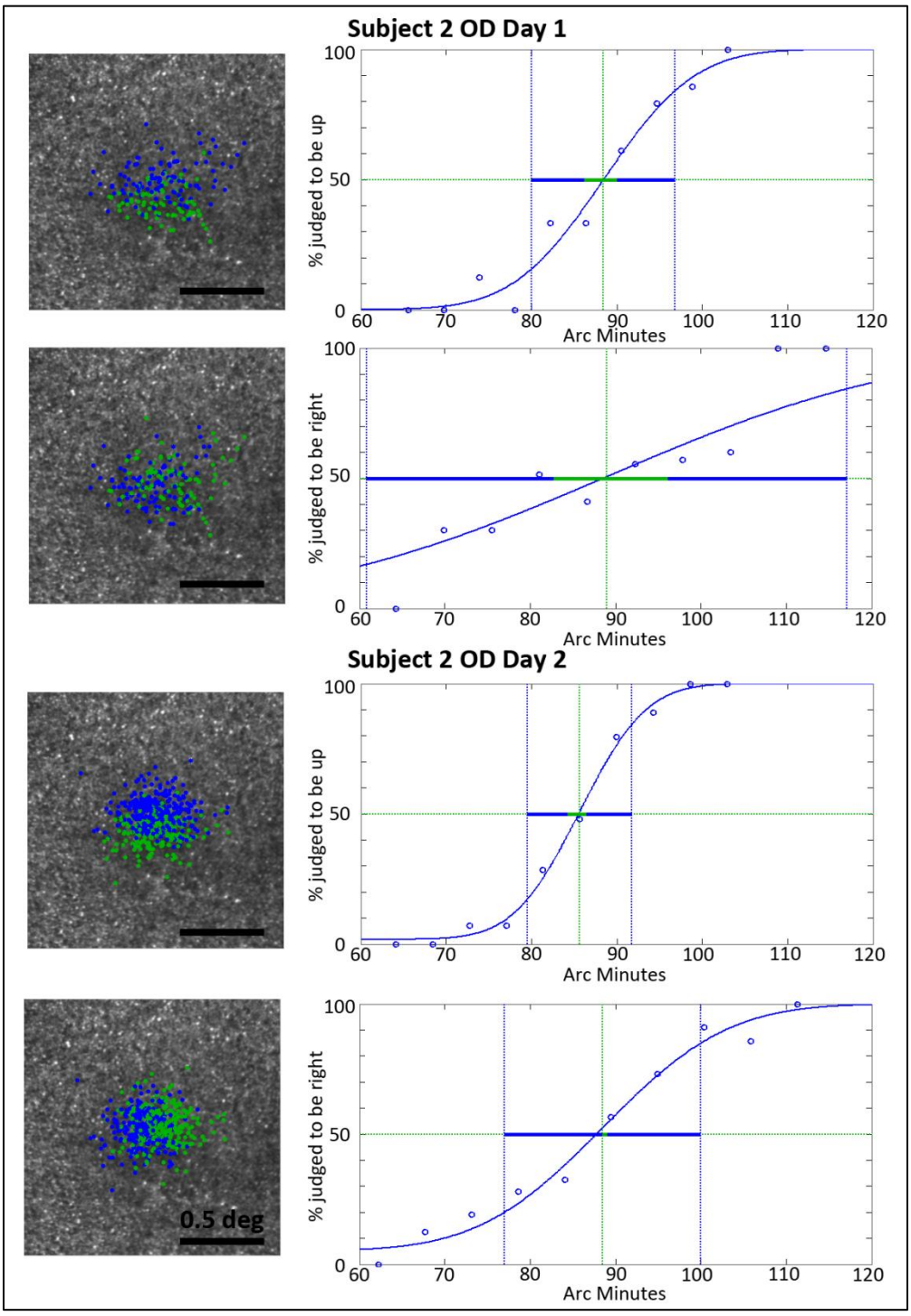

Figure 30: Subject 2 OD Cumulative Gaussian Fits for the PFD.

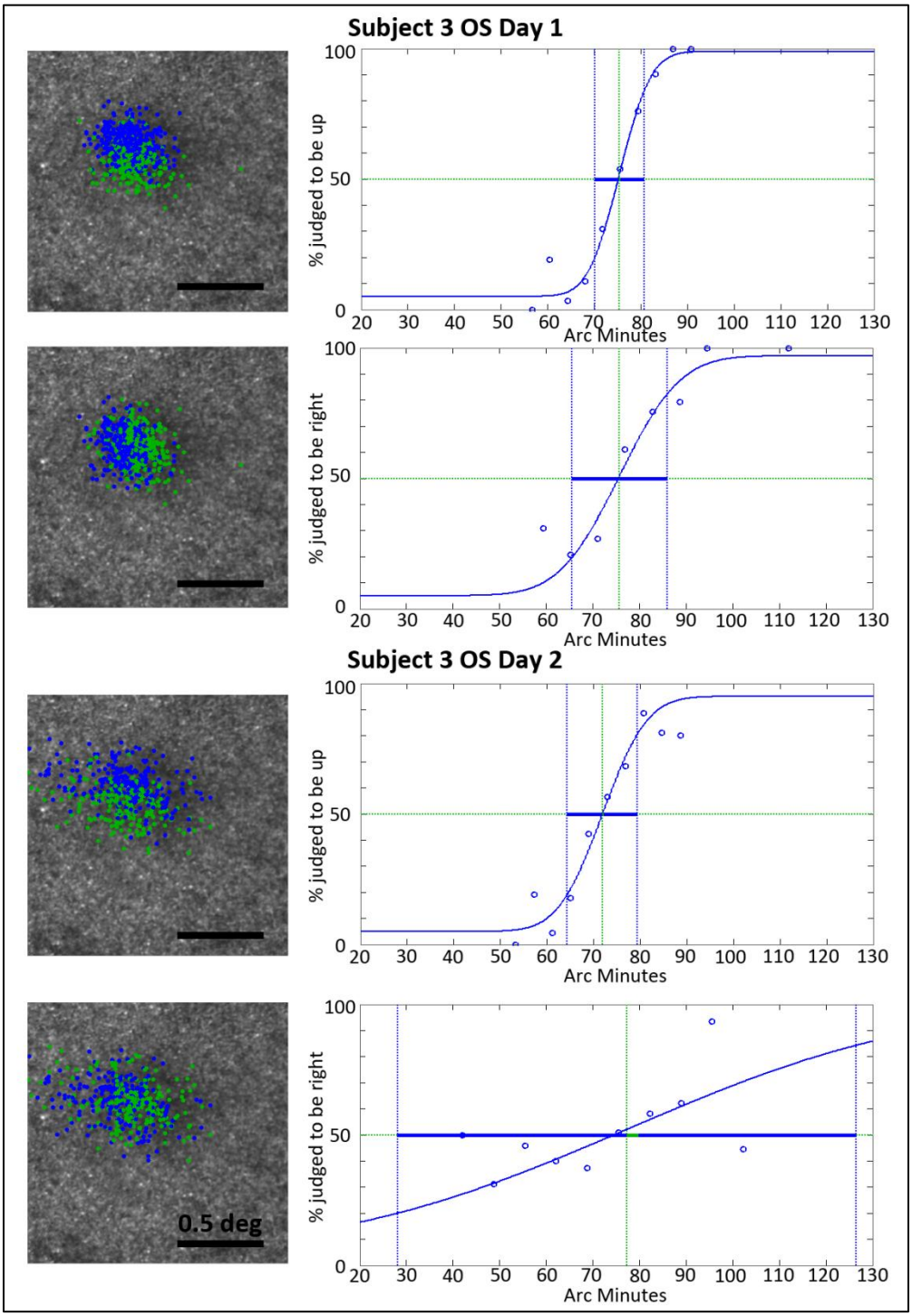

Figure 31: Subject 3 OS Cumulative Gaussian Fits for the PFD.

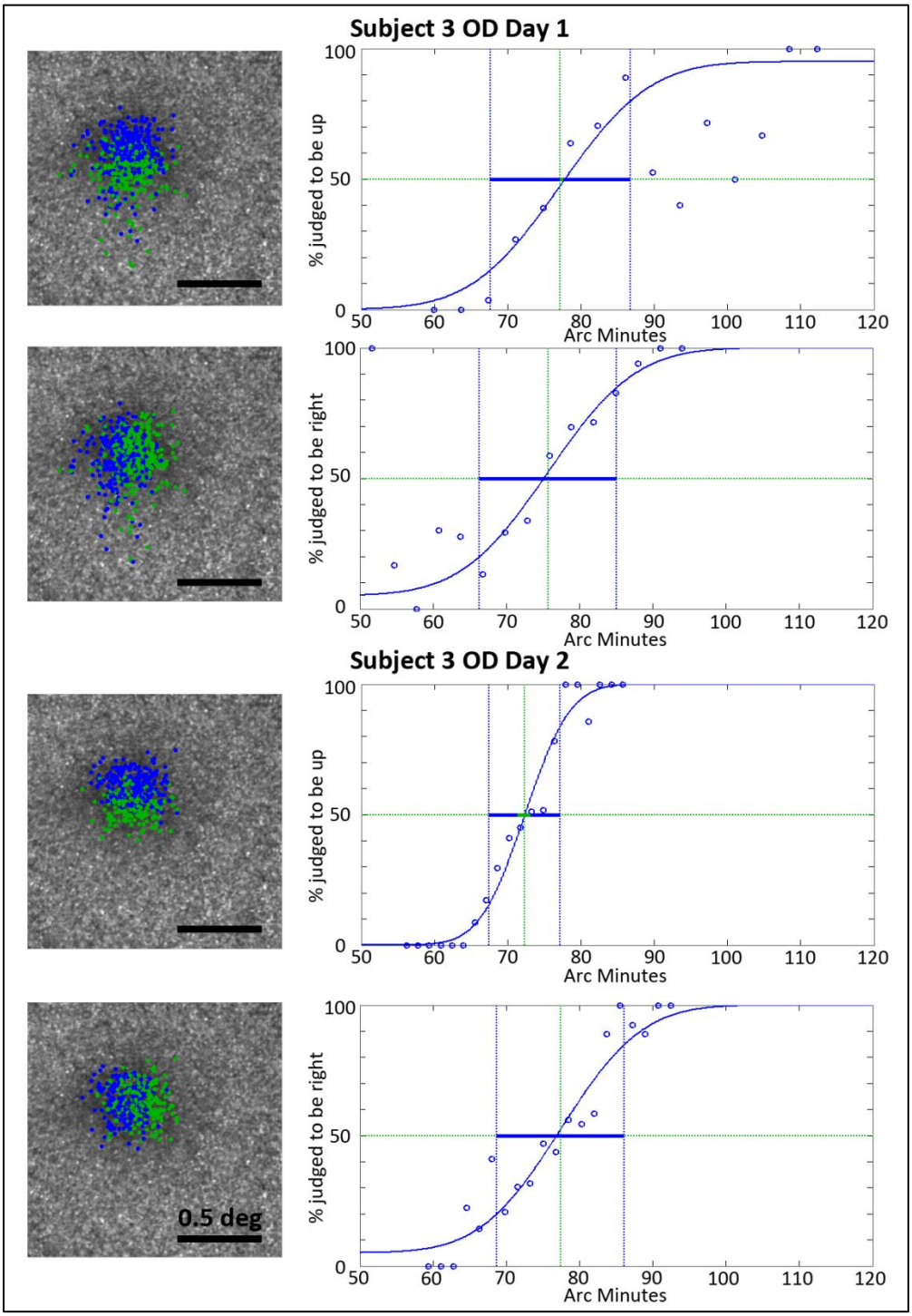

Figure 32: Subject 3 OD Cumulative Gaussian fit for the PFD